Order Number 9326527

Anisotropic traveltime tomography

Michelena, Reinaldo Jose, Ph.D.

Stanford University, 1993

U·M·I
300 N. Zeeb Rd.
Ann Arbor, MI 48106

ANISOTROPIC TRAVELTIME TOMOGRAPHY

A DISSERTATION
SUBMITTED TO THE DEPARTMENT OF GEOPHYSICS
AND THE COMMITTEE ON GRADUATE STUDIES
OF STANFORD UNIVERSITY
IN PARTIAL FULFILLMENT OF THE REQUIREMENTS
FOR THE DEGREE OF
DOCTOR OF PHILOSOPHY

By
Reinaldo J. Michelena
April, 1993

I certify that I have read this thesis and that in my opinion it is fully adequate, in scope and in quality, as a dissertation for the degree of Doctor of Philosophy.

Jerry M. Harris (Principal Advisor)

I certify that I have read this thesis and that in my opinion it is fully adequate, in scope and in quality, as a dissertation for the degree of Doctor of Philosophy.

Francis Muir

I certify that I have read this thesis and that in my opinion it is fully adequate, in scope and in quality, as a dissertation for the degree of Doctor of Philosophy.

Jon F. Claerbout

I certify that I have read this thesis and that in my opinion it is fully adequate, in scope and in quality, as a dissertation for the degree of Doctor of Philosophy.

Amos Nur

Approved for the University Committee on Graduate Studies:

Anisotropic traveltime tomography

Reinaldo J. Michelena
Stanford University, 1993

ABSTRACT

The estimation of velocity anisotropy in heterogeneous media can aid the solution of imaging and interpretation problems. It can aid imaging because when anisotropy is properly considered, events can be focused in the correct place with the correct velocity without the well known distortions obtained when using isotropic velocities in anisotropic environments. It can also help in interpretation because the anisotropy says something about how a rock is put together, which can be used, for example, to identify rock types or to characterize fracture orientation.

The effects of velocity anisotropy and heterogeneity are coupled in the data. In this thesis I show that ray theoretic traveltime tomography can be used to separate these two effects by creating a model that is both anisotropic and heterogeneous. Two different models are used at the same time: one for the velocities and one for the heterogeneities. Although there are many possible ways to describe each of these models, I show that the ones that incorporate prior information about the medium are the ones that produce more accurate results.

The model I use to describe the velocity is transversely isotropic. In accord with the observation that around the axes of symmetry a TI medium looks like an elliptically anisotropic medium, I use elliptically anisotropic models to fit the traveltimes that are assumed to correspond to rays that travel near either axis of symmetry. Then I show how the results obtained by fitting the data with ellipses can be transformed into the elastic constants that describe a general TI medium, assuming that all wave types are available. Heterogeneous media are described as a superposition of homogeneous regions, each of them transversely isotropic. No assumptions are made about the weakness of either anisotropy or heterogeneity because the ray tracing is performed in anisotropic models.

The results of synthetic and field data examples can be summarized as follows:

1. The parameters (direct and normal moveout velocities) obtained by fitting compressional and shear wave traveltimes around one axis of symmetry with elliptically anisotropic models can be transformed into the elastic constants that describe a general TI medium. The simpler the heterogeneities, the more accurate the transformation.

2. When fitting the data with iterative techniques such as conjugate gradients, different components of the velocity converge at different speed, and, therefore, early termination of the iterations may alter the anisotropy of the solution. This may also happen when regularizing the problem by damping or truncating the singular value decomposition.

3. When only one wave type is available, fitting the data with elliptically anisotropic models still produces useful partial results.

4. No assumptions are made about the weakness of the anisotropy or heterogeneity. The accuracy of the results depend on the amount of prior information that the model of heterogeneities contains about the actual medium. For 1–D variations, the solutions are stable and accurate in the presence of strong anisotropy and heterogeneity, whereas for arbitrary 2–D variations, the solutions may be unstable and less accurate.

Acknowledgments

The first advice Jerry Harris gave me when I met him almost five years ago was perhaps the most important I received: "You are at Stanford, you can do whatever you want." This advice came at a time when the only thing I knew was that I didn't know what to do. With great patience, Jerry always had time to hear my doubts and then managed not to give me answers but, instead, to put me on the track toward finding them myself. He constantly challenged my ideas, and taught me that in scientific research there is always room for improvement. Thanks, Jerry. I owe you much more than you think.

My contact with Francis Muir made me look at my research through anisotropic spectacles. Three years later, I ended up writing a dissertation on anisotropic inversion, which contains many ideas that one way or another originated in Francis's own work, his suggestions, or conversations with him. Francis's constant insight and fine sense of humor made my work much simpler and more enjoyable.

Jerry Harris and Jon Claerbout allowed me the privilege of moving freely between their research groups, the Seismic Tomography Project (STP) and the Stanford Exploration Project (SEP). In both groups, I found exceptionally rich and stimulating environments that greatly influenced the way I approach my own work. From Jon, I learned that one way to manage a group doing scientific research is by doing it himself, setting the standards. Jon's were always the highest. Amos Nur introduced me to Jerry Harris with the idea of doing some work that combined rock physics and cross-well seismology. Well, Amos, I think I ended up doing something along those lines.

My office mate and friend, Spyros Lazaratos, has helped me since I came to Stanford. I benefited greatly, during those difficult first months, from hearing about his experiences as a graduate student at Stanford and, later, from many enlightening conversations with him about our research. Spyros also picked one of the data sets I used in chapter 4. Carlos Cunha Filho arrived at Stanford the same quarter I did (and he graduated one year before

me!). Even with the enormous amount of work he had to finish in that short time, he was always willing to help, and to take some time to enjoy a beer and good food. The field experience of Mark Van Schaack helped me to understand the dirty tricks behind data acquisition, and how important it is to consider them in talking about high-resolution images. In addition, Mark carefully edited and picked the data set I used in the last chapter. David Lumley's suggestions and comments were always on target, and I found our conversations about inverse problems enlightening and thought provoking. I thank Oona Scotti, Dominique Marion and Diane Jizba for their friendship.

Martin Karrenback showed me how to use his finite-difference, elastic modeling, "the ultimate modeling machine." I used his code in chapter 3 to check the correctness of the traveltimes I was computing by ray tracing. I had also interesting conversations with Gary Mavko and and Lev Vernik. Richard Nolen-Hoeksema helped me interpret the field data results I show in chapters 4 and 5. I substantially increased my productivity thanks to the impressively done "background job" of Caroline Lambert at STP and Steve Cole, Dave Nichols, Mihai Popovici, and Martin at SEP of maintaining and updating the hardware and software within each group. The crucial background work of Sonya Williams at STP and Diane Lau at SEP, and Margaret Muir before I knew them, helped me smoothly solve many administrative puzzles. Finally, you the reader, should be grateful to Lauren Rusk, "advocate for the overwhelmed reader," who thought about you all the time while doing such a fine editorial job on this thesis.

Sven Treitel, Jerry Harris and Larry Lines made the arrangements for my visit to the Amoco Research Lab in Tulsa during the summer of 1991. There I had various enlightening conversations with Ilya Tsvankin while I was learning how to trace rays in anisotropic media. At Amoco, I also had interesting talks with Leon Thomsen and John Scales. John Queen, from Conoco, always showed interest in my work. William Harlan, also from Conoco, made important comments and suggestions about appendix A while it was being considered for publication in *Geophysics*. And Michael Schoenberg spent some time with me during a short visit to Stanford in the summer of 1992 to check whether some of the results I obtained in chapter 2 were reasonable.

Amoco Production Company and STP recorded and provided one of the data sets used in chapter 4. The other data set used in that chapter was provided by British Petroleum (BP). Jerry Harris recorded this last data set while at BP. The data used in chapter 5 were also recorded by STP at a Chevron Petroleum Technology field site.

Intevep, S.A. financed my studies, and my living, at Stanford. In particular, I want to thank Marcos Rampazzo and Orlando Chacín of Intevep for their continuous support and interest in my work. I also received financial support from Conicit (the National Council for Scientific and Technological Investigations in Venezuela).

The years at Stanford wouldn't have been nearly as intense as they were, and wouldn't have enriched my life as much as they did without the love, encouragement, and insight of my wife, Mainlin Suárez. During these years we grew together, discovering a new country, a new culture, and a new society, while rediscovering ourselves. And here we are, still growing but now with a child, Miguel Antonio, who keeps reminding us that we still have a long way to go, with him.

Contents

List of Tables

List of Figures

Chapter 1

Introduction

The effect of velocity anisotropy on wave propagation in homogeneous and heterogeneous media has been the subject of numerous publications. Careful forward modeling has helped interpreters understand how velocity anisotropy manifests itself in field data. Fewer attempts have been made, however, to solve the inverse problem, namely, the estimation of the parameters that describe the complexity of velocity anisotropy. These parameters are the elastic constants. The estimation of elastic constants is important because it can aid lithologic discrimination and fracture orientation, reveal anisotropic properties of the medium not obvious in the data, and provide further imaging or full waveform inversion algorithms with background models that can be refined iteratively. This dissertation will focus on one solution to the inverse problem, namely, the estimation of elastic constants from seismic measurements.

1.1 Anisotropy or heterogeneity?

Rocks can be anisotropic for a variety of reasons. Some rocks, minerals for example, can be inherently anisotropic depending on how their molecules arrange themselves in an orderly way to form a crystalline structure. Other rocks can become anisotropic after a sufficiently large stress has altered the crystalline structure of their constituents. Sufficiently large stresses can also cause preferentially oriented cracks in isotropic rocks or in rocks with otherwise randomly oriented cracks to make them look anisotropic at seismic frequencies. Other types of rocks can be formed by arrangements of elongated grains or fine isotropic layers that make the rocks look anisotropic at seismic frequencies. A more

detailed explanation of possible causes of rock anisotropy can be found in Crampin et al. (1984).

Backus (1962) showed that a region composed of thin isotropic layers is equivalent in the long wavelength limit to a homogeneous transversely isotropic medium. More recently, Schoenberg and Muir (1989) extended Backus's conclusion to arbitrary, anisotropic, thin layers. These results have two important implications. The first is that, for scales much smaller than the seismic wavelength, there is no way to distinguish intrinsically anisotropic materials from materials with preferentially oriented heterogeneities (e.g., fine layering), which means that, from seismic measurements alone, it is not possible to identify the causes of anisotropy. The second implication is that, for scales smaller than a fraction of the minimum wavelength in the data, there is no way to distinguish whether the medium is heterogeneous or homogeneous anisotropic. This fundamental equivalence between anisotropy and heterogeneity in the wave propagation problem has its counterpart in the inverse problem.

Both heterogeneity and anisotropy affect wave propagation. The goal of the inverse problem in heterogeneous anisotropic media is to transform this coupled effect in the data into a model that is simultaneously heterogeneous and anisotropic. At first glance, this problem may seem insoluble because of the fundamental equivalence between anisotropy and heterogeneity that I mentioned before. We should remember, however, that the equivalence in the forward problem occurs at scales that are small compared to the wavelength. At larger scales, the effects of heterogeneity and anisotropy are distinguishable, and therefore, as long as the scale of interest in the inverse problem is not too small, it should be possible to set up an inverse problem that separates such effects.

The problem of the equivalence between anisotropy and heterogeneity worsens when only a fraction of the information contained in the wavefield (e.g., first arrival traveltimes) is used for the inversion. In this case, anisotropy and heterogeneity may be equivalent every time they are described with the same number of parameters, or, even worse, with different combinations of parameters in anisotropy and heterogeneity that fit the data equally well. Figure 1.1 (taken from Babuska and Cara, 1991) illustrates this difficulty. In this example, two different models are used to fit the same pair of traveltimes: model (a) is heterogeneous isotropic and model (b) is homogeneous elliptically anisotropic. Since both sets of parameters can be used to explain the observations, there is a complete equivalence between anisotropy and heterogeneity in this case. Increasing the number

(finite) of measurements and the angles of observation is one way to resolve the ambiguity by selecting the model that fits the particular data better. However, if the model is subdivided into smaller cells, it is always possible to find a scale where the equivalence occurs because only two rays cross the small-size cells. If the ambiguity remains after increasing the number of measurements, additional information is necessary to resolve it.

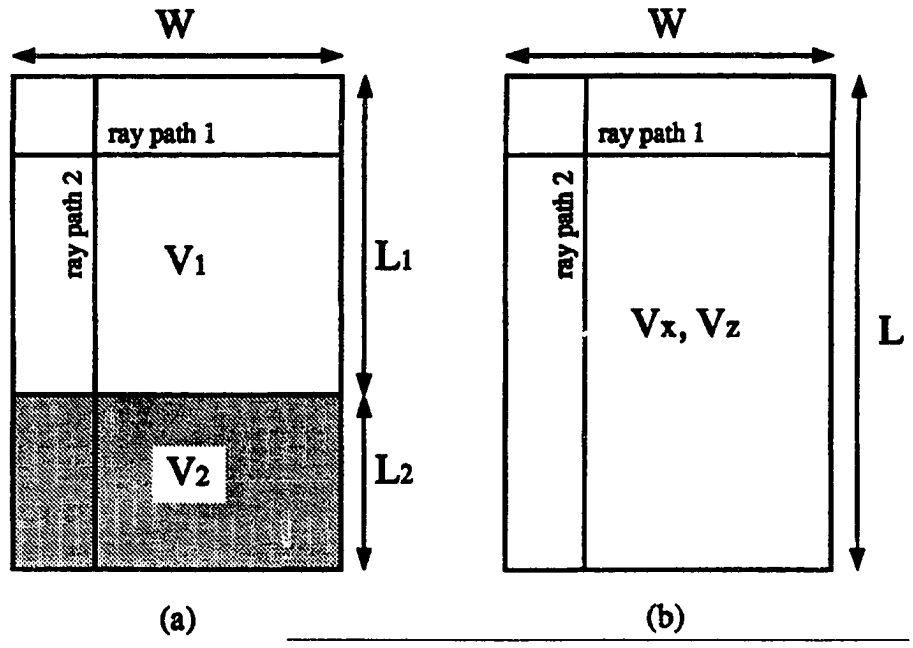

Figure 1.1: Simple velocity models that show the heterogeneity/anisotropy equivalence that needs to be considered when solving inverse problems in heterogeneous anisotropic media (after Babuska and Cara, 1991). (a) Heterogeneous isotropic model. (b) Homogeneous anisotropic model. These two models fit the data equally well.

The additional information necessary to resolve the ambiguity comes from the prior information about the medium, which tells us what model to use. That information can be used in the example of Figure 1.1 to choose between models (a) or (b) and estimate only the corresponding pair of parameters. However, if the prior information is not correct, anisotropy in the real medium is transformed into heterogeneities that do not exist, or, conversely, heterogeneities in the real medium are explained by unreal anisotropic solutions. Therefore, the selection of the proper model is crucial.

1.2 Estimation of elastic constants in heterogeneous media: previous work

Elastic constants have been estimated primarily in the lab where the small rock samples can be assumed to be homogeneous. When the assumption of homogeneity is not valid, the problem of estimation is more difficult because the effects of anisotropy and heterogeneity are coupled in the data. This coupling problem has been addressed by making prior assumptions about both effects. For example, by assuming that the rock samples are homogeneous, Arts et al. (1991) estimate, from lab measurements, the 21 elastic constants that characterize a general triclinic system. By assuming isotropic velocities, McMechan (1983) estimates tomographically arbitrary spatial variations using 2-D and 3-D models. These two papers are examples of different trade-offs between the complexity of the models in regard to velocity and heterogeneity. On the one hand, the first paper uses the simplest model for heterogeneities (homogeneous) without making any assumption about the type of velocity anisotropy. On the other hand, McMechan's paper uses the simplest model for the velocity (isotropic) without making any assumption about the heterogeneity. It is interesting to notice that even though the only model that does not assume anything about the medium is 3-D triclinic, the models used in the previous papers are usually presented as examples of models that make no assumptions about the medium.

Previous studies that have estimated variations of anisotropy with position have used "intermediate" models that simplify anisotropy and heterogeneity. The selection of the model is based on two factors: the prior information available about the medium and the geometry used to record the data. When selecting the model for anisotropy, these two factors make transverse isotropy (TI) a good candidate because, on the one hand, TI is a common form of anisotropy in the subsurface, and, on the other hand, 3-D multicomponent information that is necessary to study more complex symmetries is not usually recorded. For analogous reasons, layered models (1-D) have routinely been used to describe the heterogeneities. Therefore, not surprisingly, several authors have chosen the combination of 1-D and TI to describe their models. White et al. (1983) estimate the five TI elastic constants of a homogeneous formation using a VSP geometry. Hake et al. (1984) approximate the traveltimes curves of layered models with a three-term Taylor series expansion in which the coefficients are a function of the elastic constants. Winterstein and Paulsson (1990) estimate the elastic constants from VSP and cross-well measurements in a

medium with velocity increasing linearly with depth. Byun and Corrigan (1990) propose an iterative, model-based, optimization scheme to invert traveltimes for the five elastic constants of a layered TI medium. More recently, Sena (1991) has proposed a variant of this method in which all the calculations are done analytically, without having to go through the semblance analysis needed with Byun and Corrigan's method.

When using ray theoretic tomographic methods, the 1-D assumption about the heterogeneity can easily be relaxed. Moreover, the formulation of the problem is almost identical for any type of heterogeneity, regardless of its complexity. The simplicity of the formulation of the problem for general heterogeneity may explain why most papers on ray theoretic traveltime tomography describe the heterogeneities of the medium using the most complex and general model: a fine 2-D grid (Dines and Lytle, 1979; McMechan, 1983; White, 1989). The basis function required to describe a 2-D grid is orthogonal. Although other basis functions that don't have the property of orthogonality have been recently proposed (Van Trier, 1988; Harlan, 1989; Michelena and Harris, 1991), those that have such a property are still the most widely used to represent the heterogeneities in tomographic traveltime inversions. At the same time, however, the model assumed for velocities has been, until recently, the most simple: isotropic.

Recent papers have addressed the problem of estimating velocity anisotropy from cross-well measurements using ray theoretic traveltime tomography. These papers have focused on the problem of eliminating the artifacts obtained when isotropic tomography is used to invert data recorded in anisotropic environments (Carrion et al., 1992). McCann et al. (1989) show how an isotropic inversion improved after assuming a fixed amount of anisotropy. Stewart (1988) and Williamson et al. (1993) describe the heterogeneities with nonoverlapping square cells and the velocity anisotropy using Thomsen's (1986) expression for P-wave phase velocity in weakly anisotropic media. Saito (1991) and Lines (1992) propose to separate the effects of anisotropy and heterogeneity by first "removing" the anisotropy effects from the data so that conventional isotropic tomography in heterogeneous media can later be applied. The elimination of the anisotropy effect is partial and depends on the model of heterogeneities that is assumed. Qin et al. (1992) describe the model as a superposition of two parts, one isotropic and the other anisotropic. The heterogeneities in the isotropic part are described by small, square cells and the heterogeneities in the anisotropic part are described by large cells. By using ray paths computed in isotropic models for the anisotropic inversion, Qin et al. implicitly assume also that

the medium is weakly anisotropic. Chapman and Pratt (1992) and Pratt and Chapman (1992) also assume weak anisotropy but make no assumption about the type of anisotropy or heterogeneity. Pratt and Chapman's procedure is more complex for shear waves than for compressional waves, and it requires, as do all the previous methods, wide-aperture data.

The preceding papers (except Saito's) assume weakly anisotropic media in order to justify ray tracing in isotropic models. The assumption of weak anisotropy also justifies the use of Thomsen's equation for *P*-wave phase velocity to approximate the corresponding group velocity (in the papers by Stewart, Lines, and Williamson et al.). No assumptions are made about the heterogeneities (except in Saito's paper) which, as I show in appendix A, makes more difficult an accurate estimation of spatial variations in velocity anisotropy. Although all these papers show how to alleviate artifacts in the tomograms by estimating parameters that describe variations of velocity with direction, none of them (except Chapman and Pratt's) show how to transform those parameters into the five elastic constants that describe a general TI medium. Chapman and Pratt, however, don't show examples that illustrate the use of their transformation.

1.3 The goal of this thesis

This thesis focuses on the estimation of the elastic constants that describe heterogeneous TI media when the measurements, first arrival traveltimes, have narrow aperture around one axis of symmetry. I start by solving the problem for homogeneous media. Then I show that the generalization to heterogeneous media consists of fitting the data with heterogeneous elliptically anisotropic models that can be transformed into models for elastic constants. No assumptions are made about the weakness of the anisotropy or the heterogeneity and rays are traced in heterogeneous anisotropic models. Synthetic and field data examples show that the technique works well for simple structures, but, since only limited-aperture data are used, the technique produces less accurate results when the medium contains arbitrary 2-D structures. A detailed summary of each chapter follows.

1.3.1 Estimation of elastic constants in homogeneous TI media

In chapter 2, I explain how to estimate the elastic constants that describe a homogeneous TI medium from measurements near one or both axes of symmetry. The procedure consists

of fitting P- and SV-wave traveltimes with elliptical velocity functions. The result of this fitting is four elliptical velocities (direct and normal moveout) that can be transformed into four elastic constants by solving analytically a system of four equations and four unknowns. No assumptions are made about the weakness of the anisotropy. When the traveltimes correspond to SH-waves, the transformation between elliptical velocities and elastic constants is immediate because SH-wave slowness surfaces are already elliptical.

The equations developed in this chapter are valid near the axes of symmetry, regardless of their inclination. In particular, for vertical axis of symmetry, the procedure is more accurate for cross-well than for VSP geometries.

The procedure proposed in this chapter for homogeneous media is generalized to heterogeneous media in the rest of the thesis. The generalization consists of describing the heterogeneous medium as a superposition of homogeneous nonoverlapping regions. When the model is described in this way, two new methods are needed in order to calculate accurately the elliptical velocities at each region: ray tracing in anisotropic models and anisotropic traveltime tomography. The next two chapters describe these new procedures.

1.3.2 Kinematic ray tracing in anisotropic layered media

In chapter 3, I describe the details of the implementation of a kinematic ray tracing algorithm in transversely isotropic media with variable inclination of the axes of symmetry. The heart of the algorithm is the numerical solution of Snell's law at each interface.

Snell's law tells us how a plane wave changes direction when it hits an interface between two different media. When the media are isotropic, the wave (phase) velocity is the same as the ray (group) velocity, and, therefore Snell's law also tells us how to bend a ray at a given interface. When the media are anisotropic, the procedure is more complicated because rays and waves travel with different velocities in different directions, and it is thus necessary to change from one to the other either to propagate a ray through a region or to cross a boundary between two regions.

The traveltimes computed by this ray tracing agree, as expected, with the ones calculated by finite-difference elastic modeling in TI media.

The ray tracing algorithm developed in this chapter is used in chapter 4 to do anisotropic traveltime tomography for elliptically anisotropic models.

1.3.3 Tomographic estimation of elliptical velocities

Chapter 4 explains how to fit traveltimes with heterogeneous elliptically anisotropic models. The procedure is identical for any wave type, and it makes no assumptions about the weakness of anisotropy or heterogeneity because the rays are traced in heterogeneous anisotropic models.

To show the behavior of the algorithm when using limited view measurements, I present two simple synthetic examples where both anisotropy and heterogeneities are weak. These examples show that when we use iterative techniques such as conjugate gradients to solve the linearized problem, different components of the velocity converge at different speeds with different types of artifacts, which can alter the amount of anisotropy in the solution.

Different models for describing the heterogeneities are presented in this chapter. I conclude that for cross-well geometries, the estimation of elliptical velocities in 1-D models is accurate and stable, whereas in general 2-D models it is less accurate and unstable, because of the small singular values introduced in the problem by high-frequency variations in the vertical component of the slowness. As a result, the resolution of the different components of the slowness is also different, and, therefore variations in velocity anisotropy cannot be estimated at the same resolution as variations in the velocity. In appendix A, I explain in more detail the issue of resolution of the different components of slowness by examining the results of the singular value decomposition of the related matrices.

The *P*-wave field data examples presented in chapter 4 show that, even when only one wave type is available, useful results can be obtained by fitting the data with elliptically anisotropic models. If more wave types are available, all we need to do is apply the same algorithm separately to each of them and, finally, transform the results at each region into elastic constants, as described in chapter 2. The next chapter explains how to do that.

1.3.4 Estimation of elastic constants in heterogeneous TI media

In chapter 5, I use all the tools developed in the previous chapters in order to estimate spatial variations in the elastic constants that describe a TI medium. The procedure consists of two steps. First, compressional and shear-wave traveltimes are fitted using heterogeneous elliptically anisotropic models, as described in chapter 4. Second, the elliptical parameters are transformed locally into elastic constants, as described in chapter 2. The technique is illustrated with synthetic and field data examples for cross-well geometries.

Chapter 2

Estimation of elastic constants in homogeneous transversely isotropic media

The elastic constants that control P- and SV-wave propagation in a transversely isotropic medium can be estimated by using P- and SV-wave traveltimes from either cross-well or VSP geometries. This chapter explains the procedure, which consists of two steps. First, elliptical velocity models are used to fit the traveltimes near one axis. The result is four elliptical parameters that represent direct and normal moveout velocities near the chosen axis for P- and SV-waves. Second, the elliptical parameters are used to solve a system of four equations and four unknown elastic constants. The system of equations is solved analytically, yielding simple expressions for the elastic constants as a function of direct and normal moveout velocities. For SH-waves, the estimation of the corresponding elastic constants is easier because the phase velocity is already elliptical. The procedure for homogeneous media introduced in this chapter is generalized to heterogeneous media as explained in chapter 5, by using a tomographic technique described in chapters 3 and 4.

2.1 Introduction

The estimation of elastic constants in anisotropic media from lab measurements differs from the estimation of elastic constants from field measurements in two basic ways. First,

in the lab the medium can be assumed to be homogeneous and therefore the propagation of the energy can be safely modeled using straight ray paths. In the field, this assumption is often inadequate and ray bending needs to be properly considered. Second, in the lab it is possible to measure the velocities along all axes of symmetry, which simplifies the calculation of the corresponding elastic constants. In the field, however, the measurements usually have limited aperture, and therefore velocities in one direction have to be estimated by fitting a model to velocities measured in different directions. These two difficulties explain why, when using field data, in situ estimation of elastic constants has been rare, unless a simple model is assumed to describe the anisotropy.

Elliptical anisotropy is the simplest model of anisotropy, since it introduces only one more degree of freedom, and wave and ray relationships are similar to the isotropic case. Elliptical anisotropy is not only simple but also useful when the aperture of the experiment is such that the slowness surface is not properly sampled and is difficult to estimate more than two ray velocities, one based on the arrivals along a certain axis (direct velocities), and the other based on the curvature around that axis (normal moveout velocities). However, since most rocks do not exhibit elliptical anisotropy, the convenient properties of this type of anisotropy haven't found wide applicability, except in a few cases when the departures from isotropy are small or when the measurements are taken around an axis of symmetry.

A model commonly used to describe velocity anisotropy in the earth is the transversely isotropic (TI) model. Even though a TI model hardly ever reduces to an elliptically anisotropic one (Thomsen, 1986), a TI model appears elliptically anisotropic near the axes of symmetry. This property of transverse isotropy is used by Muir (1990a) and Dellinger et al. (1993) to approximate P- and SV-wave slowness surfaces and impulse responses of general TI media with ellipses fitted near *both* horizontal and vertical axes. In a later paper, Muir (1990b) suggests the transformation of the elliptical parameters into elastic constants by using well known expressions that relate them (Levin, 1979; Levin, 1980). However, Muir implicitly assumes in this paper that traveltimes near both axes are available, which doesn't often happen.

In this chapter I show how to obtain the elastic constants that control P- and SV-wave propagation in TI media from limited aperture traveltimes, either from VSP or from cross-well geometries. I start by fitting the traveltimes for P- and SV-waves with elliptical time-distance relations near a single axis (either vertical or horizontal). The result is four velocities: two based on the time-of-arrival and distance along an axis of symmetry (the

direct velocities) and two based on the differential traveltime and differential distance as the direction is perturbed (the normal moveout velocities). I use these four elliptical parameters to solve analytically a system of four equations and four unknown elastic constants. Since the procedure is based on fitting the data with elliptical velocity models, it is exact when estimating elastic constants from *SH*-wave traveltimes.

The data aperture is constrained in two different ways. First, it should be large enough to ensure that there is sufficient curvature to estimate the normal moveout velocities. Second, it should be narrow enough to ensure that the elliptical fit remains accurate for the given wave type. I show in this chapter that there is an intermediate range of ray angles that satisfy these two requirements in the estimation of elastic constants from either VSP or cross-well geometries.

The calculations presented here are valid for homogeneous media. When the model is heterogeneous, it can be described as a superposition of homogeneous regions, and the elliptical parameters needed at each region can be estimated tomographically, as chapter 4 explains. Once the elliptical parameters at each cell are estimated, the procedure developed here for homogeneous media can be applied at each cell to obtain 2-D maps of elastic constants. Chapter 5 presents examples of such a procedure.

The equations I use in this chapter to transform elastic constants into elliptical parameters (forward mapping) are not new. They are the same as the ones summarized by Muir (1990b), which can also be found in Levin (1979) and Levin (1980). What is new is the simultaneous solution of these equations near each axis to obtain elastic constants as a function of elliptical parameters (inverse mapping).

I start by rederiving the basic equations for forward mapping from the expression of *P*- and *SV*-wave phase velocities in TI media. The calculations are done near both the horizontal and the vertical axes. Then, using these expressions, I solve the inverse mapping analytically. The final section illustrates the use of the technique when estimating the elastic constants of a homogeneous medium from impulse responses sampled near either the vertical axis or the horizontal axis, to simulate VSP and cross-well configurations, respectively.

2.2 Forward mapping

By doing forward modeling we create data from a given set of model parameters. When the data form a different set of model parameters, I prefer to call the process forward mapping to emphasize that the transformation is done between spaces that cannot be measured directly. In this section I explain how to do the mapping from the elastic constants of a TI medium to different sets of phase velocities.

2.2.1 From elastic constants to phase velocities

The phase velocity expression for P- and SV-waves in TI media is (Auld, 1990)

$$\begin{aligned} 2W_{P,SV}(\theta) &= (W_{33}+W_{44})\cos^2\theta + (W_{11}+W_{44})\sin^2\theta \\ &\pm\sqrt{[(W_{33}-W_{44})\cos^2\theta - (W_{11}-W_{44})\sin^2\theta]^2 + 4(W_{13}+W_{44})^2\sin^2\theta\cos^2\theta}, \end{aligned} \tag{2.1a}$$

where $W_{P,SV}(\theta)$ is the phase velocity squared, and θ is the phase angle from the vertical. W_{ij} is the $(ij)^{th}$ elastic modulus divided by density, with units of velocity squared; I refer to the quantity W_{ij} as an *elastic constant* in the remainder of this chapter. The plus sign $(+)$ in front of the square root corresponds to P-waves and the minus sign $(-)$ to SV-waves. For SH-waves, the expression for the phase velocity is (Auld, 1990)

$$W_{SH}(\theta) = W_{44}\cos^2\theta + W_{66}\sin^2\theta. \tag{2.1b}$$

Near the vertical and horizontal axes ($\theta \approx 0$ and $\theta \approx 90$) equation (2.1a) is elliptical. The velocities that describe the corresponding ellipses are called elliptical velocities. In the next two sections, I rederive equations contained in previous papers (Levin, 1979; Levin, 1980; Muir, 1990b) that are needed to calculate these elliptical velocities from the elastic constants. The expressions that result are used later in the chapter to solve the inverse mapping when the data have a narrow aperture.

2.2.2 From elastic constants to phase velocities near the vertical axis

Expanding equation (2.1a) around $\theta = 0$ and neglecting terms in $\sin^4\theta$, results in

$$\begin{aligned} 2W_{P,SV}(\theta) &= (W_{33}+W_{44})\cos^2\theta + (W_{11}+W_{44})\sin^2\theta \\ &\pm\left((W_{33}-W_{44})\cos^2\theta - (W_{11}-W_{44})\sin^2\theta + \frac{2(W_{13}+W_{44})^2}{W_{33}-W_{44}}\sin^2\theta\right). \end{aligned} \tag{2.2}$$

Choosing the positive root yields the P-wave phase velocity near the vertical axis, as follows:

$$W_P(\theta) = W_{P,z}\, c^2 + W_{P,x\mathrm{NMO}}\, s^2, \tag{2.3}$$

where $c = \cos\theta$, $s = \sin\theta$,

$$W_{P,z} = W_{33}, \tag{2.4}$$

and

$$W_{P,x\mathrm{NMO}} = W_{44} + \frac{(W_{13}+W_{44})^2}{W_{33}-W_{44}}. \tag{2.5}$$

$W_{P,z}$ is the vertical P-wave phase velocity squared and $W_{P,x\mathrm{NMO}}$ is the horizontal normal moveout (NMO) phase velocity squared.

Choosing the negative root in equation (2.3) yields SV-wave phase velocities near the vertical axis, as follows:

$$W_{SV}(\theta) = W_{SV,z}\, c^2 + W_{SV,x\mathrm{NMO}}\, s^2, \tag{2.6}$$

where

$$W_{SV,z} = W_{44}, \tag{2.7}$$

and

$$W_{SV,x\mathrm{NMO}} = W_{11} - \frac{(W_{13}+W_{44})^2}{W_{33}-W_{44}}. \tag{2.8}$$

The previous expressions for the NMO velocities agree with the results of Thomsen (1986) and Vernik and Nur (1992).

The expression for SH-wave phase velocities near the vertical axis is

$$W_{SH}(\theta) = W_{SH,z}\, c^2 + W_{SH,x\mathrm{NMO}}\, s^2, \tag{2.9}$$

where

$$W_{SH,z} = W_{44}, \tag{2.10}$$

and

$$W_{SH,x\mathrm{NMO}} = W_{SH,x} = W_{66}. \tag{2.11}$$

2.2.3 From elastic constants to phase velocities near the horizontal axis

P- and *SV*-wave phase velocities near the horizontal axis can be obtained by interchanging W_{11} and W_{33} and c^2 and s^2 wherever they occur in equations (2.3) through (2.8). Thus, for *P*-waves the result is

$$W_P(\theta) \;=\; W_{P,x}\; s^2 + W_{P,z\mathrm{NMO}}\; c^2, \tag{2.12}$$

where

$$W_{P,x} \;=\; W_{11}, \tag{2.13}$$

and

$$W_{P,z\mathrm{NMO}} \;=\; W_{44} + \frac{(W_{13}+W_{44})^2}{W_{11}-W_{44}}. \tag{2.14}$$

For *SV*-waves, the expression for the phase velocity near the horizontal axis is

$$W_{SV}(\theta) \;=\; W_{SV,x}\; s^2 + W_{SV,z\mathrm{NMO}}\; c^2, \tag{2.15}$$

where

$$W_{SV,x} \;=\; W_{44}, \tag{2.16}$$

and

$$W_{SV,z\mathrm{NMO}} \;=\; W_{33} - \frac{(W_{13}+W_{44})^2}{W_{11}-W_{44}}. \tag{2.17}$$

Near the horizontal axis the *SH*-wave phase velocities are

$$W_{SH}(\theta) \;=\; W_{SH,x}\; s^2 + W_{SH,z\mathrm{NMO}}\; c^2, \tag{2.18}$$

where

$$W_{SH,x} \;=\; W_{66}, \tag{2.19}$$

and

$$W_{SH,z\mathrm{NMO}} \;=\; W_{SH,z} \;=\; W_{44}. \tag{2.20}$$

In the rest of the chapter I refer to the elliptical parameters $W_{P,x}$, $W_{P,z}$, $W_{P,x\mathrm{NMO}}$, $W_{P,z\mathrm{NMO}}$, $W_{SV,x}$, $W_{SV,z}$, $W_{SV,x\mathrm{NMO}}$, $W_{SV,z\mathrm{NMO}}$, $W_{SH,x}$, $W_{SH,z}$, $W_{SH,x\mathrm{NMO}}$, and $W_{SH,z\mathrm{NMO}}$ as W_*, direct, or NMO phase velocity squared for *P*-, *SV*-, and *SH*-waves.

2.3 Inverse mapping

The preceding equations that relate phase velocities and elastic constants suggest several approaches to solve the inverse mapping that depend on the recording geometry, the recording aperture, and the wave types available. From *SH*-wave phase velocities near either axis, it is always possible to estimate W_{44} and W_{66} because the NMO velocities are equal to corresponding direct velocities. However, from *P*- and *SV*-wave phase velocities near either axis, the estimation of the corresponding elastic constants is not straightforward. This section explains what to do in such a case.

2.3.1 Using *P*- and *SV*-wave full aperture phase velocities

To estimate W_{11}, W_{33}, W_{44}, and W_{13} directly from equation (2.1a), we need at least four phase velocities at four different angles between 0 and 90 degrees. W_{ij} is the solution of a system of nonlinear equations where the independent term is formed by these phase velocities. Along the axes, the system of equations is almost diagonal, and the estimation of three elastic constants (W_{33}, W_{11}, and W_{44}) is straightforward:

$$W_{33} = W_{P,z}, \tag{2.21a}$$

$$W_{11} = W_{P,x}, \tag{2.21b}$$

$$W_{44} = W_{SV,z} = W_{SV,x}. \tag{2.21c}$$

The elastic constants are estimated directly from phase velocities along the axes. W_{13} can be estimated from the previous elastic constants and one phase velocity at an oblique angle, typically 45 degrees.

This approach, though simple in theory, is not applicable in many practical situations because wide aperture data are required (i.e., the angles of the observations must include 0, 90 degrees, and one intermediate measurement) to simplify the system of equations. This is not the case for most single-geometry data sets (either surface, or cross-well or VSP) where no rays travel along at least one axis and therefore phase velocities along both axes cannot be estimated without having to assume a velocity symmetry (e.g., isotropic, elliptical, or TI).

2.3.2 Using P- and SV-wave narrow aperture phase velocities

Elastic constants from phase velocities near the vertical

When the phase angles are close to zero, it is possible to estimate elastic constants from the corresponding phase velocities by using equations (2.4), (2.5), (2.7), and (2.8), a system of four equations and four unknowns. The independent term (that I will explain how to obtain in section 2.4, "Obtaining the phase velocities") is formed by $W_{P,z}$, $W_{P,x\text{NMO}}$, $W_{SV,z}$, and $W_{SV,x\text{NMO}}$. The solution of this system of equations is

$$W_{33} = W_{P,z}, \tag{2.22a}$$

$$W_{44} = W_{SV,z}, \tag{2.22b}$$

$$W_{13} = \sqrt{(W_{P,x\text{NMO}} - W_{SV,z})(W_{P,z} - W_{SV,z})} - W_{SV,z}, \tag{2.22c}$$

$$W_{11} = W_{SV,x\text{NMO}} + W_{P,x\text{NMO}} - W_{SV,z}. \tag{2.22d}$$

In (2.22d), W_{11} is a linear combination of elliptical parameters independent of the horizontal P-wave phase velocity, unlike the W_{11} estimated from equation (2.21c). Equation (2.22d) says, roughly, that summing P- and SV-wave NMO velocities (squared) is the same as summing the elastic constants that control the horizontal wave propagation. The examples in the final section of the chapter show the range of angles near the vertical for which these equations are valid.

Since this approximation simultaneously uses the elliptical parameters of two ellipses fitted near the vertical, I call it *vertical*, double elliptic approximation, analogous to Muir's double elliptic approximation that uses horizontal and vertical ellipses to approximate the slowness surface and impulse response for all angles (Muir, 1990a; Dellinger et al., 1993). It is important to recognize the differences between these two approximations. On the one hand, the *vertical*, double elliptic approximation is used to estimate elastic constants from phase velocities near the vertical axis. Slowness surfaces and impulse responses can be calculated from these elastic constants using (2.1a) and the exact relationships between phase and group velocities. On the other hand, Muir's double elliptic approximation is used to estimate directly slowness surfaces and impulse responses from data near both axes without having to know the elastic constants.

Fitting P- and SV-wave phase velocities with ellipses near the vertical is not the same as using the vertical, double elliptic approximation. However, the fitting is a necessary

intermediate step in the estimation of elastic constants using equations (2.22). When the elliptical fitting is done near the horizontal axis, the result is the *horizontal*, double elliptic approximation, as follows.

Elastic constants from phase velocities near the horizontal

When the phase angle is close to 90 degrees, the expressions for the elastic constants as a function of P- and SV-wave phase velocities are obtained by solving the system of equations (2.13), (2.14), (2.16), and (2.17), with the following result:

$$W_{11} = W_{P,x}, \tag{2.23a}$$

$$W_{44} = W_{SV,x}, \tag{2.23b}$$

$$W_{13} = \sqrt{(W_{P,z\text{NMO}} - W_{SV,x})(W_{P,x} - W_{SV,x})} - W_{SV,x}, \tag{2.23c}$$

$$W_{33} = W_{SV,z\text{NMO}} + W_{P,z\text{NMO}} - W_{SV,x}. \tag{2.23d}$$

This set of equations forms the *horizontal*, double elliptic approximation. It uses elliptical P- and SV-wave phase velocities near the horizontal to approximate the elastic constants. Notice that the estimation of W_{33} is independent of the P-wave phase velocity along the vertical axis. Equations (2.23) can be obtained from (2.22) by interchanging W_{11} and W_{33}, and x and z.

The estimation of W_{33} from near-horizontal phase velocities [equation (2.23d)] and W_{11} from near-vertical phase velocities [equation (2.22d)] is in both cases the sum of NMO velocities minus W_{44}. I show in appendix A that when estimating velocities tomographically, NMO velocities correspond to the smallest singular values of the problem. The largest singular values correspond to velocities estimated from rays that travel along the axes. Therefore, as expected, estimating W_{33} from cross-well traveltimes alone is a harder problem than estimating W_{11} from the same data. The opposite is true when estimating W_{33} and W_{11} from VSP measurements.

2.3.3 Using only P-wave phase velocities near the axes

When the medium is TI and no information is available about SV-wave phase velocities, it is still possible to obtain four elastic constants from only P-wave phase velocities near both axes. This is done by solving the system of equations (2.4), (2.5), (2.13), and (2.14),

which yields

$$W_{11} = W_{P,x}, \tag{2.24a}$$

$$W_{33} = W_{P,z}, \tag{2.24b}$$

$$W_{44} = \frac{W_{P,x\mathrm{NMO}}W_{P,z} - W_{P,z\mathrm{NMO}}W_{P,x}}{W_{P,x\mathrm{NMO}} + W_{P,z} - W_{P,z\mathrm{NMO}} - W_{P,x}}, \tag{2.24c}$$

$$W_{13} = \sqrt{(W_{P,x\mathrm{NMO}} - W_{44})(W_{P,x} - W_{44})} - W_{44}. \tag{2.24d}$$

This set of equations forms the P-wave, double elliptic approximation of the elastic constants in a TI medium.

In this approximation, as well as in the previous ones, the assumption of transverse isotropy is crucial. When the medium is isotropic ($W_{P,x} = W_{P,z} = W_{P,x\mathrm{NMO}} = W_{P,z\mathrm{NMO}}$) there is no way to calculate W_{44} (the shear modulus) from P-wave phase velocities alone because equation (2.24c) is indeterminate. When the medium is weakly anisotropic the estimation of W_{44} using this approximation may still be unreliable because both the numerator and the denominator in (2.24c) are close to zero. We will see from the examples later in the chapter that even when the medium is moderately anisotropic this approximation breaks down quickly for phase angles not close to the axes, unlike the previous vertical and horizontal double elliptic approximations [equations (2.22) and (2.23), respectively] that have a wider range of validity.

If only SV-wave phase velocities near the axes are available, it is not possible to obtain the corresponding elastic constants, because the system of equations (2.7), (2.8), (2.16), and (2.17) is underdetermined.

2.4 Obtaining the phase velocities

Equations (2.3) , (2.6), (2.12), and (2.15) show that the phase velocities of P- and SV-waves are elliptical near the axes of symmetry. Those of SH-waves are also elliptical [as equation (2.1b) shows]. When the phase velocity has an elliptical shape, the corresponding impulse response is also elliptical (Levin, 1978; Byun, 1982). Therefore, the group slowness expression that corresponds to these equations has the general form

$$S^2(\phi) = S_z^2 \cos^2\phi + S_x^2 \sin^2\phi, \tag{2.25}$$

where ϕ is the ray angle measured from the vertical, and S_* (the ray slowness) is

$$S_*^2 = \frac{1}{W_*}. \tag{2.26}$$

To estimate S_*, I use the expression for the traveltime of a ray that travels a distance $l = \sqrt{\Delta x^2 + \Delta z^2}$ between two points:

$$t^2 = \Delta x^2 S_x^2 + \Delta z^2 S_z^2. \tag{2.27}$$

This equation, which has the same form as the isotropic moveout equation, is obtained after multiplying equation (2.25) by l^2. Velocities estimated from the curvature around one axis of symmetry using this traveltime equation are called NMO velocities, and velocities estimated from arrival times along the same axis are called direct velocities. Hence the different names chosen for the phase velocities W_*.

2.5 Using traveltimes to estimate elastic constants

The procedure for estimating the elastic constants of a homogeneous TI medium from traveltime measurements near one axis of symmetry is the following:

1. Fit the traveltimes with elliptically anisotropic models, one model for each wave type. This gives direct and NMO group slownesses.

2. From the direct and NMO group slownesses, find the corresponding direct and NMO phase velocities, using equation (2.26).

3. From the estimated phase velocities, find the elastic constants, using the equations that correspond to the given recording geometry [either (2.22) or (2.23)]. For *SH*-waves, the estimated phase velocities squared are the same as the corresponding elastic constants.

This procedure can be generalized to heterogeneous media by describing the model as a superposition of homogeneous blocks. Chapters 3 and 4 explain the basic ingredients of this approach which are anisotropic ray tracing and tomographic estimation of elliptical velocities.

2.6 Examples

This section contains examples that illustrate how four elastic constants of a homogeneous TI medium can be estimated when the data are (a) P- and SV-wave traveltimes from VSP geometries with different apertures, (b) P- and SV-wave traveltimes from cross-well geometries with different apertures, and (c) P-wave traveltimes from cross-well and VSP geometries with different apertures.

The impulse response is given, and it is the same for all examples. The elastic constants that describe the medium are: $\sqrt{W_{11}} = 7400$, $\sqrt{W_{33}} = 6295$, $\sqrt{W_{13}} = 5575$, and $\sqrt{W_{44}} = 2160$, all with units of (ft/s) (Byun and Corrigan, 1990). I calculate the ellipse that fits the impulse response near the chosen axis by using a ray along the axis and a ray close to the axis. Once I have found the four needed elliptical parameters I use equation (2.22), (2.23), or (2.24) to convert those elliptical parameters into elastic constants.

2.6.1 Estimating W_{ij} from VSP P- and SV-wave traveltimes

Figure 2.1 shows how the vertical double elliptic approximation works for different angles around the vertical. The parameters of the ellipses that approximate the impulse response have been calculated at the angles shown by the straight lines. The left column compares the given impulse responses for P- and SV-waves (continuous lines) with the elliptical approximations around the vertical (dashed lines). With the four elliptical parameters obtained for each aperture, I calculate the elastic constants of the medium by using equation (2.22). From the estimated elastic constants, I then calculate the corresponding impulse responses for both P- and SV-waves. The result is shown in the central column (dashed lines) together with the given impulse responses. In most cases (except with the 40-degree aperture) the agreement is excellent. With the 40-degree aperture the horizontal P-wave group velocity has been overestimated and the shear wave triplication is larger than expected. The right column shows the absolute value of the percentage error made in the estimation of the elastic constants. For small angles ($\leq$ 10 degrees), the error is negligible. For angles between 10 and 30 degrees, the error is smaller in W_{11} (A) than in W_{13} (F). For large angles, the error in W_{11} (A) is the largest, almost 30 percent. Notice that up to 30 degrees, even though the error in the estimation of the elastic constants is not zero but a few percent, the differences between given and estimated impulse responses are hard to see.

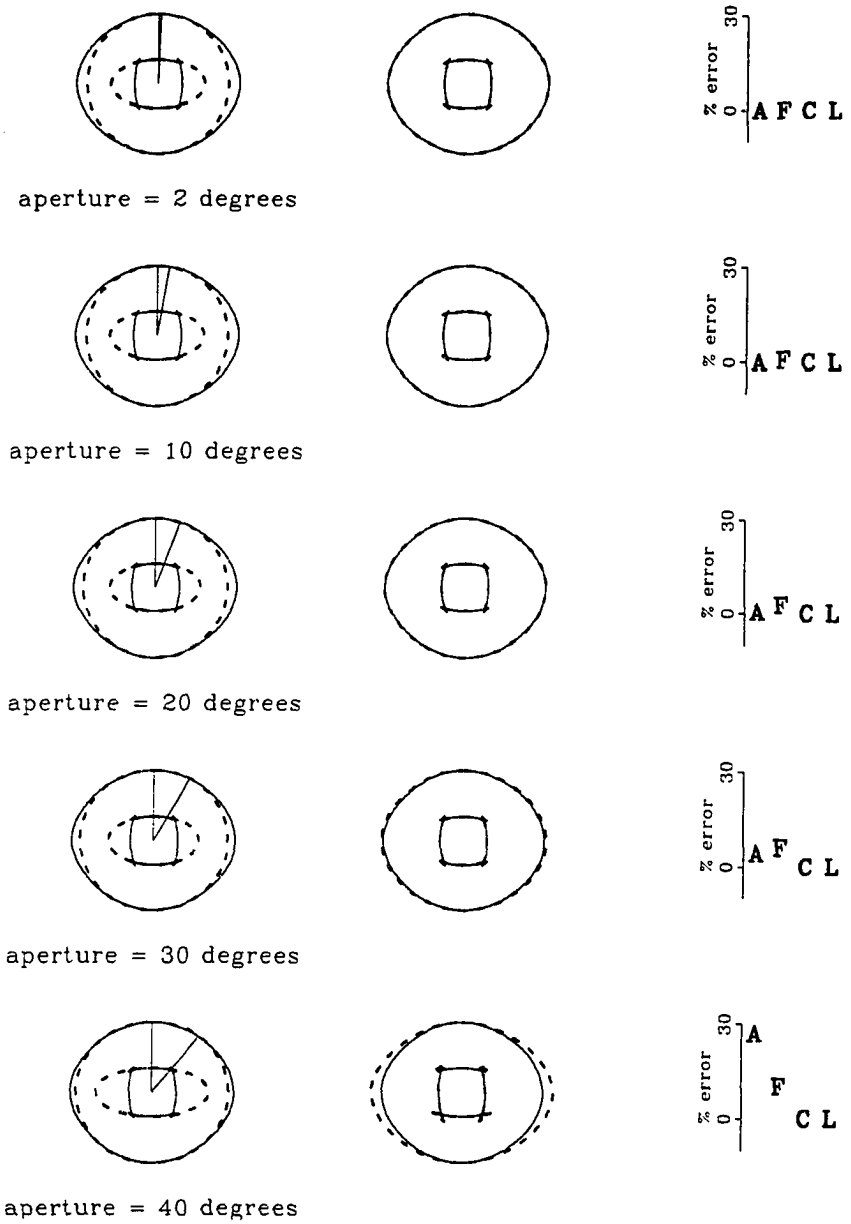

Figure 2.1: Left: impulse response for P- and SV-waves (continuous lines) compared with their elliptical approximations around the vertical (dashed lines). Center: given impulse responses (continuous) compared with the ones calculated from the estimated elastic constants (dashed). Right: absolute value of the error made in the estimation of the elastic constants when using the vertical, double elliptic approximation. The elastic constants are A = W_{11}, F = W_{13}, C = W_{33}, and L = W_{44}. The density is assumed to be unity.

In Figure 2.1, the elliptical approximations to the impulse responses are calculated using two ray angles at a time, one zero and one nonzero. Figure 2.2 shows what happens when all these angles (or different VSP offsets) are used simultaneously to calculate the elliptical approximations and the elastic constants. The horizontal P-wave group velocity is now slightly overestimated, and the shear velocities are retrieved well. The errors in the estimated elastic constants are six percent in W_{11} (A) and four percent in W_{13} (F). The errors made when using only large angles have been compensated by also using small angles.

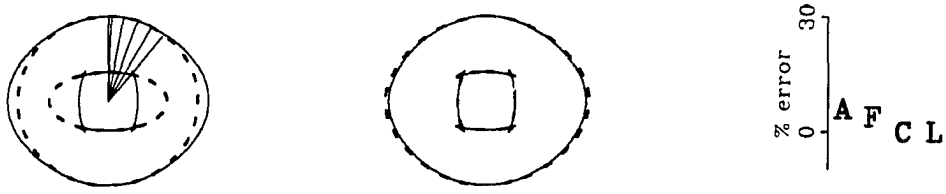

Figure 2.2: Left: impulse response for P- and SV-waves (continuous lines) compared with their elliptical approximations around the vertical (dashed lines). All ray angles shown are used simultaneously to calculate the elliptical approximations. Center: given impulse responses (continuous) compared with the ones calculated from the estimated elastic constants (dashed). Right: absolute value of the error made in the estimation of the elastic constants when using the vertical, double elliptic approximation. The elastic constants are A = W_{11}, F = W_{13}, C = W_{33}, and L = W_{44}.

2.6.2 Estimating W_{ij} from cross-well P- and SV-wave traveltimes

Figure 2.3 shows how the horizontal, double elliptic approximation works for different ray angles measured from the horizontal. When comparing this case with the VSP case (Figure 2.1), we see that the approximation works better for ray angles around the horizontal than around the vertical, even when the angles are large. The estimated impulse responses agree well with the given ones, and the errors in the elastic constants are negligible for angles less than 30 degrees.

The reason the horizontal, double elliptic approximation works better than the vertical, double elliptic approximation is that the elliptical approximation for P-wave impulse response is more adequate at larger angles around the horizontal than around the vertical, where the group velocity is lower. For P-waves, the elliptic approximations around the vertical are almost circular, which explains why in practice the NMO velocity is a good estimate for the actual vertical velocity of the medium.

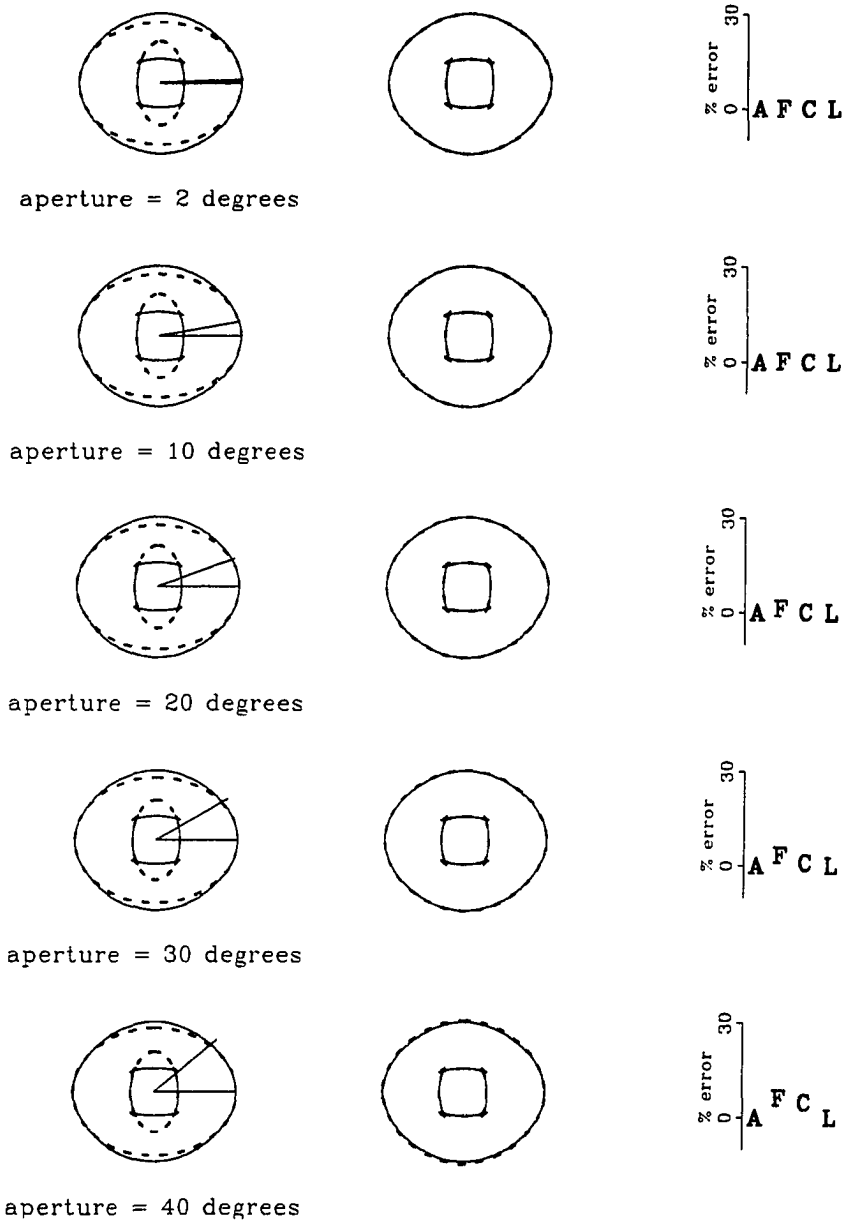

Figure 2.3: Left: impulse response for P- and SV-waves (continuous lines) compared with their elliptical approximations around the vertical (dashed lines). Center: given impulse responses (continuous) compared with the ones calculated from the estimated elastic constants (dashed). Right: absolute value of the error made in the estimation of the elastic constants when using the horizontal, double elliptic approximation. The elastic constants are A = W_{11}, F = W_{13}, C = W_{33}, and L = W_{44}.

Figure 2.4 shows that when small and large ray angles are used simultaneously to calculate the elliptical approximations around the horizontal, the result is roughly an average of the results shown in Figure 2.3. The agreement between given and estimated impulse responses is excellent and the error in the estimation of the elastic constants is $\approx$ two percent for W_{13} (F) and $\approx$ one percent for W_{33} (C).

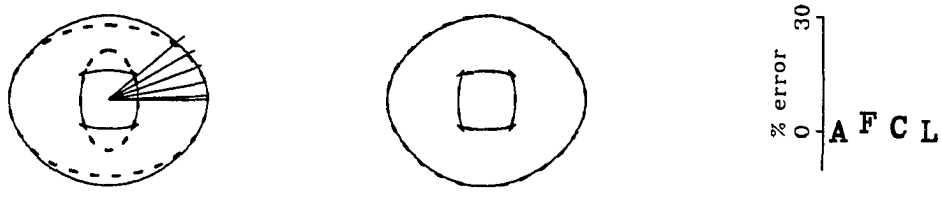

Figure 2.4: Left: impulse response for P- and SV-waves (continuous lines) compared with their elliptical approximations around the vertical (dashed lines). All ray angles shown are used simultaneously to calculate the elliptical approximations. Center: given impulse responses (continuous) compared with the ones calculated from the estimated elastic constants (dashed). Right: absolute value of the error made in the estimation of the elastic constants when using the horizontal, double elliptic approximation. The elastic constants are A = W_{11}, F = W_{13}, C = W_{33}, and L = W_{44}.

2.6.3 Estimating W_{ij} from cross-well and VSP P-wave traveltimes

For TI media, the elastic constants that control the P- and SV-wave propagation can be estimated from P-wave measurements near the axes, as equation (2.24) shows. Figure 2.5 is an example. The left column shows the given P-wave impulse response (continuous line) and the approximating ellipses (dashed lines) around the horizontal and around the vertical for two different apertures. The central column shows the given and approximate impulse responses for P- and SV-waves, the approximate impulse responses calculated from the estimated elastic constants. The right column shows the absolute value of the error made in the estimation of the elastic constants. Unlike the previous approximations, the P-wave, double elliptic approximation is valid only at very small angles ($\approx$ two degrees). At greater angles it yields highly inaccurate results, particularly in the estimation of W_{44} (L), which controls the shear wave propagation along the axes. Note that for an aperture of 10 degrees, the shear wave impulse response has been considerably underestimated.

This approximation may be hard to use in practical situations because it works only for very small angles near the axes.

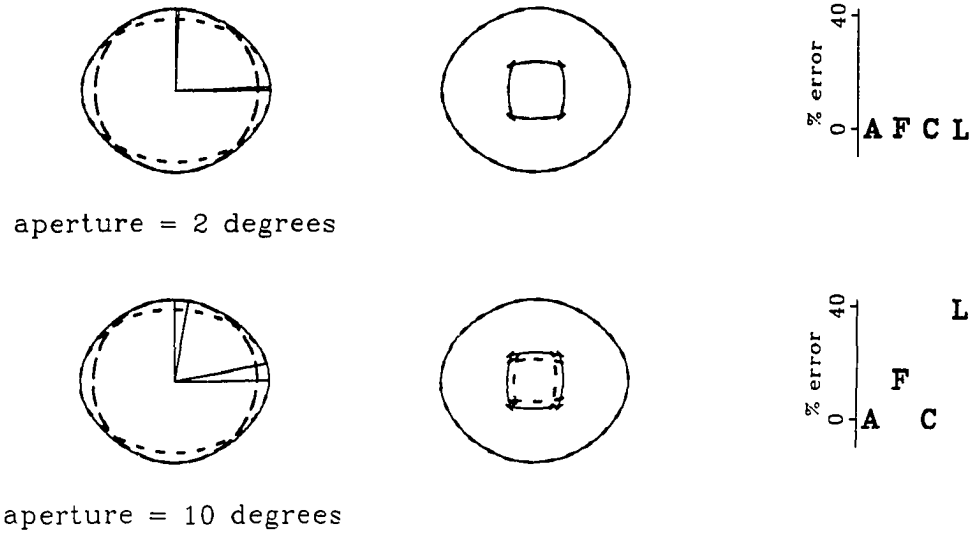

Figure 2.5: P-wave impulse response used to estimate the elastic constants from measurements around the axes. Left: given P-wave impulse response (continuous lines) and elliptical approximations around the axes (dashed lines). Center: given impulse response (continuous) and estimated ones (dashed) for P- and SV-waves. Right: absolute value of the error made in the estimation of the elastic constants when using the P-wave double elliptic approximation.

2.7 Constraints on elliptical velocities in layered media

I have shown that traveltimes from both compressional and shear waves are necessary for an accurate estimation of the elastic constants from measurements near the axes of symmetry. However, in cases when only one set of traveltimes is available, we may still obtain useful information about the medium from the elliptical velocities that best fit the given traveltimes, if we know in advance possible causes of the anisotropy of the medium.

In particular, when the anisotropy is caused by fine layering of isotropic materials, as Backus (1962) shows, $W_{66} \geq W_{44}$, which, combined with the energy constraints on W_{ij}, leads to

$$W_{11} \geq W_{44}. \tag{2.28}$$

For this type of anisotropy, an additional inequality is provided by Berryman (1979) and Helbig (1979):

$$W_{13} < W_{13E}, \tag{2.29}$$

where

$$W_{13E} = \sqrt{(W_{11} - W_{44})(W_{33} - W_{44})} - W_{44} \tag{2.30}$$

is a particular value of W_{13} that makes expression (2.1a) elliptical for P-waves and circular for SV-waves. By combining equation (2.28) and equation (2.30), results

$$W_{33} \geq W_{44}. \tag{2.31}$$

Then, by using equations (2.28), (2.29), and (2.31), and fact that in general

$$W_{11} \geq W_{33}, \tag{2.32}$$

it is possible to obtain bounds for the normal moveout velocities derived in previous sections. The procedure is simple. One bound is obtained from the equation of the corresponding normal moveout velocity as a function of the elastic constants. The other bound is obtained by using equation (2.29). The results can be summarized as follows:

$$W_{SV,x} < W_{P,x\text{NMO}}, W_{SV,x\text{NMO}} < W_{P,x}, \tag{2.33}$$

$$W_{SV,z} < W_{P,z\text{NMO}}, W_{SV,z\text{NMO}} < W_{P,z}. \tag{2.34}$$

These inequalities are valid when the axis of symmetry is either vertical or horizontal.

If the anisotropy is caused by fine layering of isotropic materials then the relative sizes of the direct and NMO velocities are given by inequalities (2.33) and (2.34). In other words, fine layering $\Rightarrow$ (2.33) or (2.34). However, the reverse [i.e., (2.33) or (2.34) $\Rightarrow$ fine layering] is not necessarily true but it can aid the interpretation when the causes of anisotropy are suspected or when a complete inversion of all the elastic constants is not possible. For example, from cross-well measurements the estimated $W_{P,z\text{NMO}}$ is smaller than $W_{P,x}$ when the axis of symmetry is vertical (i.e., $W_{P,z} < W_{P,x}$) but this is not necessarily the case when the axis of symmetry is horizontal (i.e., $W_{P,z} > W_{P,x}$). Notice that inequalities (2.33) and (2.34) are strict. When direct and normal moveout velocities are found to be equal, the anisotropy of the medium cannot be caused by fine layering.

When the conditions $W_{SV,x\text{NMO}} = W_{SV,z}$ and $W_{SV,z\text{NMO}} = W_{SV,x}$ are substituted into equations (2.8) and (2.17) respectively, we obtain $W_{13} = W_{13E}$, and therefore P-wave velocities are elliptical and SV-wave velocities are circular. This means that, for shear waves, isotropy around one axis indicates that the velocities are isotropic for all angles.[1]

[1]Here *isotropy* means that the phase velocity is circular. This use of the term does not take into account the nature of the particle motion, which may not correspond to a pure SV-mode (Dellinger, 1991).

For compressional waves, isotropy around one axis does not always mean isotropy for all angles. When the condition $W_{P,x\text{NMO}} = W_{P,x}$ is substituted into equation (2.14), we get $W_{13} = W_{11} - 2W_{44}$, and when $W_{P,x\text{NMO}} = W_{P,z}$ in equation (2.5), it follows that $W_{13} = W_{33} - 2W_{44}$. None of these values of W_{13} transform (2.1a) into a circle, unless $W_{11} = W_{33}$.

2.8 Conclusions

I have shown how to estimate the elastic constants of homogeneous TI media from *P*-, *SV*-, and *SH*-wave traveltimes near a single axis of symmetry (either from VSP or cross-well geometries). The technique uses the parameters obtained by fitting traveltimes near one axis with elliptical models. For *SH*-wave traveltimes, the estimation of the corresponding TI elastic constants is simple because *SH*-wave phase velocities are also elliptical in TI media. For *P*- and *SV*-wave traveltimes, four parameters are needed to estimate the phase velocities at all angles from measurements near one axis. These parameters are the direct and NMO phase velocities for *P*- and *SV*-waves.

The transformation from elliptical parameters to elastic constants is simple for both VSP and cross-well geometries.

The accuracy in the estimation of the elastic constants from the elliptical parameters depends on the accuracy in the estimation of the NMO velocities. For small ray angles the approximation is excellent when using either VSP or cross-well geometries because the elliptical approximations are adequate in both cases. In practice, however, using only small ray angles may hinder an accurate estimation of NMO velocities. For intermediate ray angles, the estimation of vertical *P*-wave velocities from cross-well geometries is more accurate than the estimation of horizontal *P*-wave velocities from VSP. This is because the elliptical approximation for the *P*-wave impulse response fits wider angles around the horizontal than around the vertical where the group velocity is smaller. For large ray angles the approximation doesn't work because elliptical fits are not as accurate.

When compressional and shear velocity logs are also available, they can be used either to add redundancy in the estimation of W_{11} and W_{44} or to check whether the assumption of transverse isotropy is valid, in particular when using cross-well measurements where vertical velocities are not well sampled.

In chapter 5, I show how we can combine this technique and anisotropic traveltime

tomography to estimate spatial variations of elastic constants. But to do anisotropic traveltime tomography, we should first be able to trace rays in anisotropic models. The next chapter explains how.

Chapter 3

Kinematic ray tracing in anisotropic layered media

The first step toward estimating tomographically elliptical velocities in heterogeneous anisotropic media is to be able to do ray tracing. In this chapter, I review a procedure to trace rays in layered transversely isotropic models with dipping interfaces. Group velocities are used to propagate the ray across each homogeneous layer, and phase velocities are used to find out how a given ray changes its direction when impinging on an interface. The equation that relates the ray parameter of the incident ray with the angle of the emergent phase at each interface is studied in detail. Finally, examples of ray tracing in simple anisotropic models are shown.

3.1 Introduction

Estimating velocity anisotropy tomographically from cross-well traveltime data is a process that often has two kinds of nonlinearity: the anisotropy itself and the ray bending from one iteration to the next. Under certain conditions one of these nonlinearities can be neglected while the computations related to other one are simplified. For example, assuming weak anisotropy, Pratt and Chapman (1992), and Chapman and Pratt (1992) proposed to do the ray tracing in isotropic media and to use those rays to back project in the anisotropic model. As I show in chapter 4, the problem can be simplified even more if the velocity contrasts are small enough that the rays traced on the anisotropic model are straight and the only nonlinearity that remains is in the estimation of the anisotropy. Unfortunately,

these simplifications are not generally valid and therefore the problem needs to be solved by tracing rays appropriately in inhomogeneous anisotropic media.

Methods for dynamic ray tracing in inhomogeneous anisotropic media have been proposed by Červený (1972), Hanyga (1982), Jech and Pšenčík (1989), and Gajewski and Pšenčík (1990), among others. These methods are based on the solution of the dynamic ray tracing equations. To solve only the kinematic problem (what is needed to do traveltime tomography), Byun (1982, 1984) proposed a different technique based on the application of Snell's law at each interface.

In this chapter, I review and implement Byun's procedure for kinematic, anisotropic ray tracing. From the boundary conditions at each interface, I derive the equation that relates the ray parameter p of the incident phase to the angle of the transmitted phase. Using this equation and the equations that relate phase and group velocities, I describe a procedure that alternatively uses each type of velocity to propagate a ray across a layer and to figure out how it changes direction when impinging on an interface. The last section gives examples of P-wave ray tracing for a cross-well geometry in different layered transversely isotropic models. In chapter 4, I use this ray tracing procedure to do traveltime tomography in elliptically azimuthally anisotropic media.

3.2 Boundary conditions

A wave impinging on a plane interface between two media must satisfy the kinematic boundary condition

$$\mathbf{v}_1 = \mathbf{v}_1, \tag{3.1}$$

which states that the particle velocity must be continuous at all points on the boundary between medium 1 and medium 2 (Auld, 1990).

If the wave field is described as a superposition of functions of the form $\exp(i\mathbf{kr})$, the condition (3.1) implies that for both incident and scattered waves the component of $\mathbf{k}$ tangential to the boundary ($\mathbf{k}_{||}$) must be the same. If we divide $\mathbf{k}$ by the frequency ω of the incident wave and define a vector $\tilde{\mathbf{k}}$ of magnitude $1/v$ (where v is the phase velocity) as follows:

$$\tilde{\mathbf{k}} = \frac{\mathbf{k}}{\omega} = \frac{\mathbf{k}}{\|\mathbf{k}\|}\frac{1}{v}, \tag{3.2}$$

the continuity of $\mathbf{k}_{||}$ implies the continuity of $\tilde{\mathbf{k}}_{||}$, usually called ray parameter $\mathbf{p}$ for which

$$\mathbf{p_1} = \mathbf{p_2}. \tag{3.3}$$

Since we know that $\mathbf{p}$ is parallel to the interface, the ray parameter is usually considered as a scalar p with a positive or negative sign in front to indicate the sign of the angle of the incident phase with respect to the normal.

Auld (1990) examines condition (3.3) by looking at the corresponding slowness surfaces (a plot of $\|\tilde{\mathbf{k}}\|$ as a function of its direction), as Figure 3.1 shows. In this figure the slowness surfaces for both P- and S-waves are represented for each isotropic medium. The vector $CA = AB = \mathbf{p}$ is the projection on the interface of the point on the slowness surface that corresponds to the incident P-wave phase. From the construction of Figure 3.1 it is possible to derive easily Snell's law that gives the angles of the scattered phases for both P- and S-waves:

$$\begin{aligned} p &= \frac{1}{v_{1_P}}\sin(\theta_{P_i}) = \frac{1}{v_{2_P}}\sin(\theta_{P_t}) = \frac{1}{v_{2_S}}\sin(\theta_{S_t}) \\ &= \frac{1}{v_{1_S}}\sin(\theta_{S_r}) = \frac{1}{v_{1_P}}\sin(\theta_{P_r}). \end{aligned} \tag{3.4}$$

Snell's law tells us how a given phase changes its direction when it crosses the interface between two media. It also tells us how rays change direction when crossing an interface, but the medium must be isotropic for this to be true, as in Figure 3.1. In isotropic media, since rays and waves travel in the same direction with the same velocity, boundary conditions valid for waves are also used to predict the behavior of rays. In anisotropic media, however, this simplification is no longer valid because, in general, rays and waves travel with different velocities in different directions as shown in Figure 3.2.

3.3 Initial value ray tracing

When the medium is horizontally layered and isotropic, tracing a ray across the different interfaces is easy. From the medium's velocities and the direction of the ray at the source (p), successive applications of (3.4) tell us how a ray changes its direction as it travels. The only angles that matter are those of the incident and refracted rays. If the layers dip the problem is slightly more complicated because p has to be calculated every time the

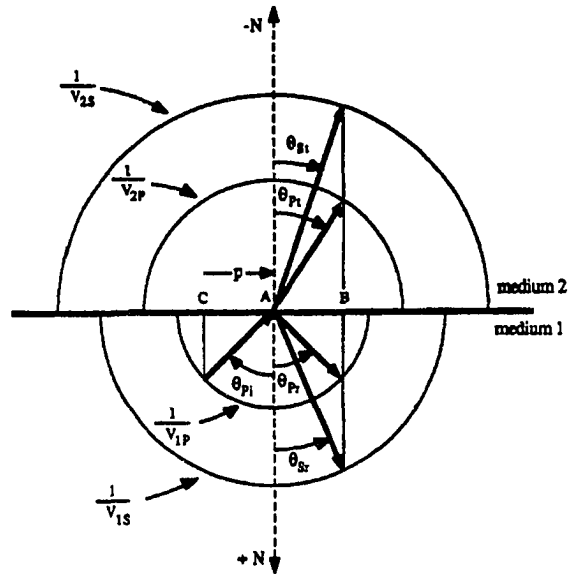

Figure 3.1: Plane-wave scattering at a plane boundary between two isotropic media. From this construction Snell's law can be easily derived. Ray and phase directions are equal.

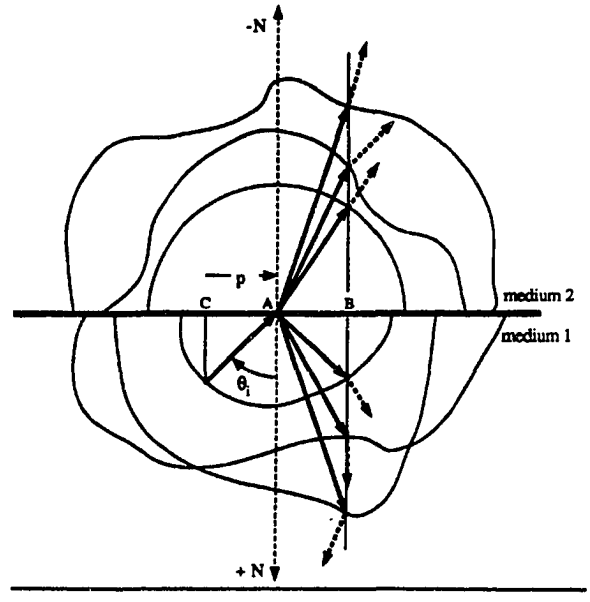

Figure 3.2: Plane-wave scattering at a plane boundary between two anisotropic media. The slowness surfaces are separated and nonspherical. Ray directions (dashed arrows at the slowness surfaces) and phase directions (continuous arrows) are no longer the same.(Modified from Aki and Richards, 1980.)

ray reaches a new interface and we have to consider with three instead of two angles at each boundary.

When the medium is anisotropic, we have to consider with seven angles at each interface to figure out how a ray changes its direction. All these angles (positive counterclockwise) are shown in Figure 3.3. The continuity of the slowness across the interface [equation (3.3)] is expressed as follows:

$$p = \frac{\sin(\theta_i + \gamma_1)}{v_1(\theta_i)} = \frac{\sin(\theta_t + \gamma_2)}{v_2(\theta_t)}, \tag{3.5}$$

where $v_1(\theta_i)$ and $v_2(\theta_t)$ are the phase velocities in the corresponding media evaluated at the incident and transmitted phase angles, respectively. The sums $(\theta_i + \gamma_1)$ and $(\theta_t + \gamma_2)$ have to be calculated considering the proper signs of the angles. From equation (3.5) we can see that when $p = 0$ (normal incidence) the angle of the transmitted phase does not depend on the phase velocity and is $\theta_t = -\gamma_2$. Any other relation derived from (3.5) must reproduce this simple result.

Given the function $v(\theta)$ for each medium, equation (3.5) describes how the incident phase $\tilde{\mathbf{k}}$ changes its direction when crossing the interface between two media. However, (3.5) does not show what happens to the direction and velocity of the associated ray. These two quantities can be calculated from the equations that relate phase and ray velocities (Byun, 1984):

$$v(\theta) = V(\phi)\cos(\phi - \theta), \tag{3.6a}$$

$$\tan(\phi - \theta) = \frac{1}{v(\theta)}\frac{dv(\theta)}{d\theta}, \tag{3.6b}$$

$$V^2(\phi) = v^2(\theta) + \left(\frac{dv(\theta)}{d\theta}\right)^2, \tag{3.6c}$$

where $V(\phi)$ is the ray velocity along the ray angle ϕ.

Equations (3.5) and (3.6) are the basic relations for tracing a ray in a medium where $v(\theta)$ and γ are given for each layer. Byun (1984) proposes the following procedure to do so: (1) Assign a value to $\theta = \theta_i$ at the source position. (2) Repeat the next steps for each layer: (a) Evaluate $v(\theta)$ and $\frac{dv(\theta)}{d\theta}$ at the corresponding θ. (b) Find ϕ_t and $V(\phi_t)$ from equation (3.6). (c) Trace a ray along the angle ϕ_t until it reaches the next interface. (d) Find p of the incident wave using equation (3.5). (e) Solve equation (3.5) for θ_t. (3) Return to step 2a.

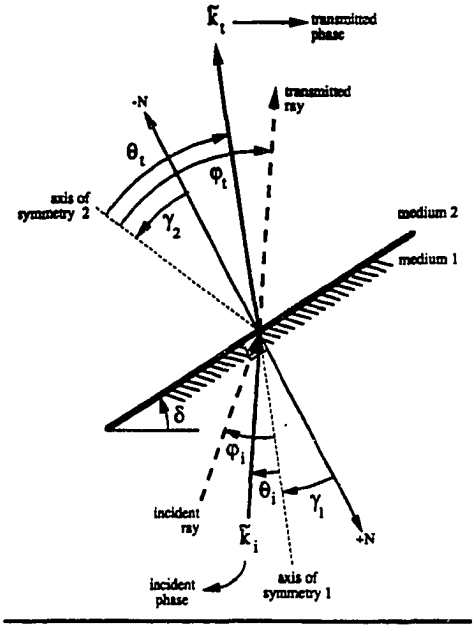

Figure 3.3: Incident (i) and transmitted (t) group and phase angles of a ray impinging on a plane interface between two transversely isotropic media.

The previous ray tracing procedure is valid for any phase velocity function $v(\theta)$. What changes from one choice of the velocity function to another is how to solve step 2e [to find θ_t as a function of p using equation (3.5)]. The next section focuses on how to accomplish this step when the medium is transversely isotropic.

3.4 Solving for the phase angle

3.4.1 *P*- and *SV*-waves

In a transversely isotropic medium, the phase velocity $v(\theta)$ for *P*- and *SV*-waves is expressed as follows (Auld, 1990):

$$\begin{aligned} 2\rho v^2(\theta) &= c_{11}\sin^2(\theta) + c_{33}\cos^2(\theta) + c_{44} \\ &\pm \sqrt{[(c_{11}-c_{44})\sin^2(\theta) + (c_{44}-c_{33})\cos^2(\theta)]^2 + (c_{13}+c_{44})^2\sin^2(2\theta)}, \end{aligned} \tag{3.7}$$

where c_{ij} are four of the five elastic constants that describe a homogeneous transversely isotropic medium. The plus sign (+) in front of the square root corresponds to *P*-waves and the minus sign (−) to *SV*-waves. ρ is the density.

An equation for the transmitted phase angle θ_t as a function of the incident p can be obtained by substituting equation (3.7) into equation (3.5) which results in the following fourth-order polynomial in $\tan(\theta_t)$:

$$a_0 + a_1 \tan(\theta_t) + a_2 \tan^2(\theta_t) + a_3 \tan^3(\theta_t) + a_4 \tan^4(\theta_t) \;=\; 0, \tag{3.8}$$

where the coefficients a_i are given in appendix B. A similar expression obtained by Byun (1984) is not correct because $\theta_t = -\gamma_2$ is not a root of the polynomial when $p = 0$, as equation (3.5) predicts.

As shown in appendix B, the coefficients a_i are the same for both P- and SV-waves [the $\pm$ in front of the square root in equation (3.7) is lost in the derivation of (3.8)], and they are independent of the sign of p. In principle, by solving this equation at each interface, it should be possible to find the angle of the transmitted phase by computing the arctangent of one of its roots. However, the procedure is not straightforward. On the one hand, we have to identify the solutions that correspond to p or $-p$ and P- or SV-waves. On the other hand, finding an angle from its tangent is not a one-to-one transformation because $\tan(\theta) = \tan(\theta + n\pi)$ and therefore infinite angles satisfy equation (3.8). Aside from these problems, we usually have to deal with the difficulties of solving equation (3.8) numerically.

Let's first examine the numerical problems. It is well known that most algorithms used to find roots of polynomials fail in the presence of multiple (or close to multiple) roots. This is the case with equation (3.8) when $p = 0$. From equation (3.5), we find that in this case the transmitted phase angle is $\theta_t = -\gamma_2$ and therefore it is not necessary to solve equation (3.8) when $p = 0$. Problems may also arise when $p \approx 0$ because the roots are close to being multiple. The way I found around this problem is based on the assumption that the slowness surface is a smooth function of θ and that therefore when $p \approx 0$, $v_2(\theta_t) \approx v_2(-\gamma)$. If this is true, $\theta_{t_0} = -\gamma_2$ can be used as starting point to find θ_t by successive applications of equation (3.5) as follows:

$$\theta_{t_{i+1}} \;=\; \sin^{-1}(p v_2(\theta_{t_i})) - \gamma_2. \tag{3.9}$$

Typically, only one iteration is required.

Figure 3.4 shows how to solve equation (3.8) graphically. From the construction with the slowness surfaces, we can see that the infinite roots of equation (3.8) mentioned earlier in this section correspond to only eight different points in the slowness surfaces for both

P- and *SV*-waves. In this figure I also assume that the incident phase (not shown) is crossing the interface from medium 1 to medium 2. For simplicity, I assume that both media are isotropic. The slowness surfaces in medium 2 are represented half by continuous circles and half by dotted circles. The slowness surfaces in medium 1 are not shown. For a given $\pm p$ value at the interface, this figure shows the position of all the possible points in the *P* and *SV* slowness surfaces whose angle measured from the symmetry axis satisfies equation (3.8). These points are obtained by simple application of the kinematic boundary condition (3.3). The points *A*, *B*, *C*, and *D* are the solutions for negative p and the points *H*, *G*, *F*, and *E*, obtained by adding $\pm\pi$ to the previous solutions are the solutions for positive p. If $|p| > \frac{1}{v_p}$, two of the roots of (3.8) are complex and there are no transmitted *P*-waves. If $|p| > \frac{1}{v_s}$, the four roots are complex and there are no transmitted *SV*-waves either. I assume that when the transmitted ray travels parallel to the interface, it doesn't go back to the previous medium, which is a simplification of the actual behavior of head waves.

If we take "1" as the axis of symmetry in Figure 3.4, we see that when the axis of symmetry and the normal to the interface are parallel, the arctangent of the roots of equation (3.8) give the angles of the points *A*, *B*, *E*, and *F*. This is because the FORTRAN function ATAN gives its results in the interval $(-\pi/2, +\pi/2)$, which is exactly the domain of the phase angle measured from the axis of symmetry. "2" is also an axis of symmetry in this example because the medium is isotropic. If we take "2" as the axis of symmetry, the roots of equation (3.8) give the points *E*, *F*, *G*, and *H*. None of these points is the correct one when, for example, a *P*-wave impinges on the interface with negative p. In this case, the point *B* is the solution.

The preceding example tells us that when the axis of symmetry and the normal to the interface are not parallel, the roots of equation (3.8) may not give the expected direction for the refracted phase. For this reason, it is necessary to examine all eight angles and pick the one that verifies equation (3.5) for the desired wave type (with this, the number of possible angles is reduced from eight to two) and produces a ray pointing toward the expected direction (which further reduces the number of angles from two to one). This procedure will be explained in more detail in the next section, which concerns *SH*-waves.

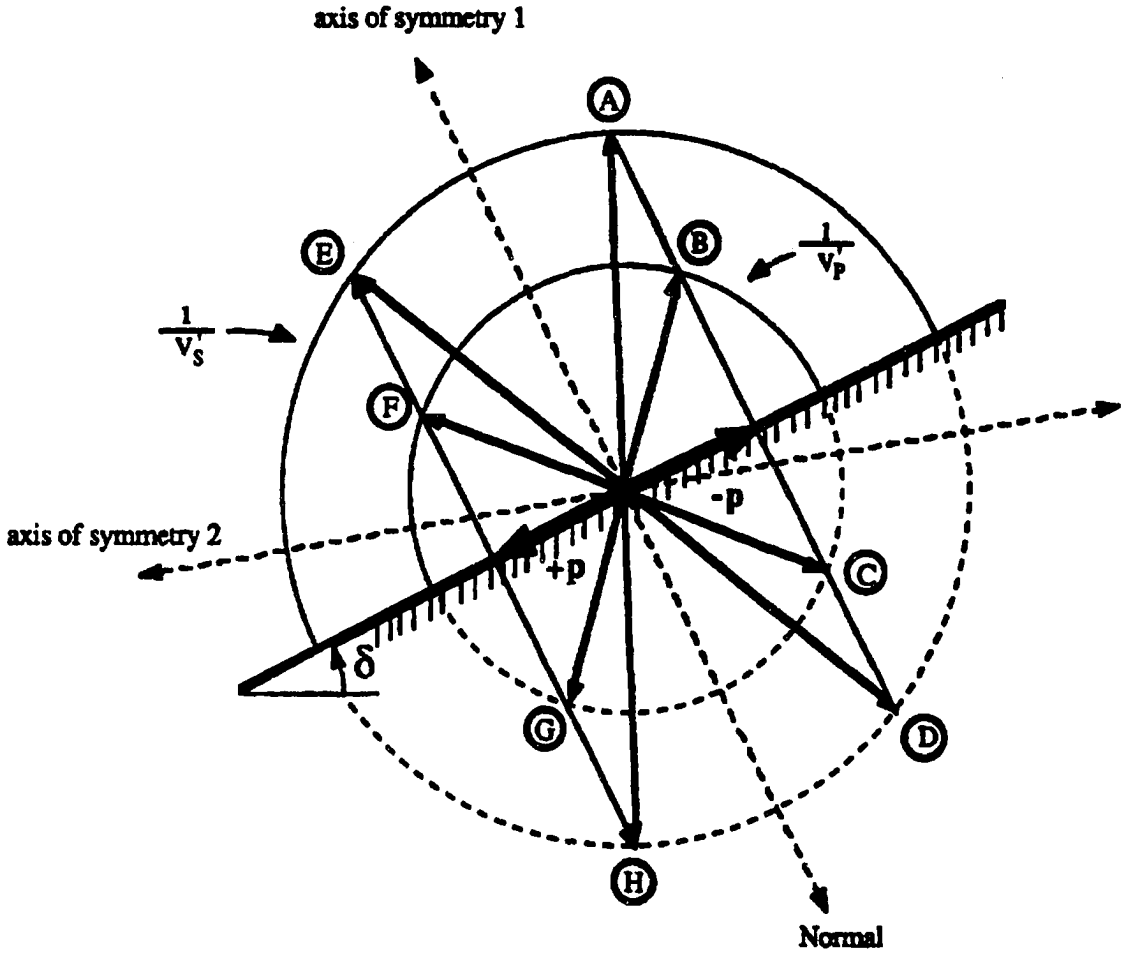

Figure 3.4: Graphical solution for the angle of the transmitted phase as a function of the incident p. The tangent of the angles at A, B, C, D, E, F, G, and H are roots of equation (3.8). Among these eight angles, only one reproduces the incident p for the corresponding wave type in the expected direction. When solving equation (3.8) numerically, only those angles at ± 90 degrees from the axis of symmetry are obtained. The axes of symmetry 1 and 2 are two of the possible axes of symmetry of the isotropic medium in which the transmitted phase travels.

3.4.2 *SH*-waves

SH-waves in a transversely isotropic medium have elliptical slowness and wave surfaces. An elliptical slowness surface may not be a good *global* (i.e., for all angles) approximation for a P or SV slowness surface in a transversely isotropic medium, but it is a good *paraxial* approximation. Hence the importance of elliptical anisotropy in data fitting, specially when the measurements have limited aperture, as I explain in chapter 2.

The procedure explained in the preceding section for P- and SV-waves can be also used to trace rays when the medium is elliptically anisotropic. To see how this can be done, let's first rewrite the expression for the phase velocities (3.7):

$$\begin{aligned} 2\rho v^2(\theta) &= (c_{11}-c_{44})\sin^2(\theta)+(c_{33}-c_{44})\cos^2(\theta)+2c_{44} \\ &\pm \Big([(c_{11}-c_{44})\sin^2(\theta)+(c_{33}-c_{44})\cos^2(\theta)]^2 \\ &+ [(c_{13}+c_{44})^2-(c_{11}-c_{44})(c_{33}-c_{44})]\sin^2(2\theta)\Big)^{1/2}. \end{aligned}$$

To convert this equation into that of an ellipse (or a circle), we need to zero the coefficient of $\sin^2(2\theta)$ inside the square root. This is done by choosing

$$c_{13} = \sqrt{(c_{11}-c_{44})(c_{33}-c_{44})}-c_{44}.$$

This substitution, however, doesn't simplify the numerical computations.

Byun (1982) shows an alternative way to do the ray tracing that is computationally simpler than using the procedure for P- and SV-waves. He shows that when the slowness surfaces are elliptical the calculation at each interface of the refracted ray angle ϕ_t is simpler, because the phase angle θ_t does not need to be explicitly computed. Byun's expression for the ray parameter as a function of the ray's angle at each interface is

$$p = \frac{v_{\|}^{-2}\sin(\gamma_2)+v_{\perp}^{-2}\cos(\gamma_2)\tan(\phi_t)}{\sqrt{v_{\|}^{-2}+v_{\perp}^{-2}\tan^2(\gamma_2)}}, \tag{3.10}$$

where $v_{\|}$ and $v_{\perp}$ are the *SH*-wave velocities in the directions parallel and perpendicular to the axis of symmetry. After doing some algebra it is possible to solve for the ray angle ϕ_t, which yields

$$\tan(\phi_t) = \left(\frac{v_{\perp}}{v_{\|}}\right)\frac{sin(\gamma_2)\cos(\gamma_2)\pm\sqrt{v_{\|}^2\cos^2(\gamma_2)+v_{\perp}^2\sin^2(\gamma_2)-(pv_{\|}v_{\perp})^2}}{p^2v_{\perp}^2-\cos^2(\gamma)}. \tag{3.11}$$

Since equation (3.11) is independent of the sign of p, it gives the solutions of (3.10) for both positive and negative p. The correct ϕ_t is the one that gives the expected sign of p and corresponds to a ray in the desired direction.

If we take the extra step of solving explicitly for the phase angle at each interface, we have to choose among the four different points in the slowness surface whose angles satisfy equation (3.5), the one that produces a ray pointing in the desired direction. The "desired direction" depends on the type of problem for which the ray tracer is used. Figure 3.5 shows how to pick the roots that correspond to transmitted rays, the ones needed in transmission traveltime tomography. In this figure, the horizontal distance from the center of the each ellipse to the vertical line is equal to the incident p. As we see, to obtain transmitted rays (dashed arrows with a black head), it is enough to pick the root that produces a ray pointing toward medium 2. In some cases the transmitted ray can travel parallel to the interface with the phase direction (continuous arrows) parallel to it or not (Figures 3.5f and 3.5e, respectively). The emergent phase angle may be greater than 90 degrees for the transmitted ray, as shown in Figure 3.5g. The ray pointing toward medium 2 may also go backwards, as Figure 3.5h shows. When the vertical line doesn't intersect the ellipse, there are no transmitted but only reflected rays (in which the angle of incidence is greater than the critical angle). However, to keep track more easily of the rays that hit the interface at post-critical angles, I assume that they continue traveling along the interface. The inversion procedure described in chapter 4 doesn't use these rays.

3.5 Model of heterogeneities

In this chapter, the rays are traced in heterogeneous models that are superposition of homogeneous transversely isotropic layers with dipping interfaces. The interfaces are not allowed to cross within the area of interest. Each layer is defined by the intersects and dips of the boundaries, the five elastic constants that define a transversely isotropic medium and the orientation of the axis of symmetry with respect to the vertical. When the anisotropy is elliptical, the five elastic constants are substituted by the velocities in the direction parallel and perpendicular to the axis of symmetry. This type of model simplifies the two-point ray tracing procedure described in the next section.

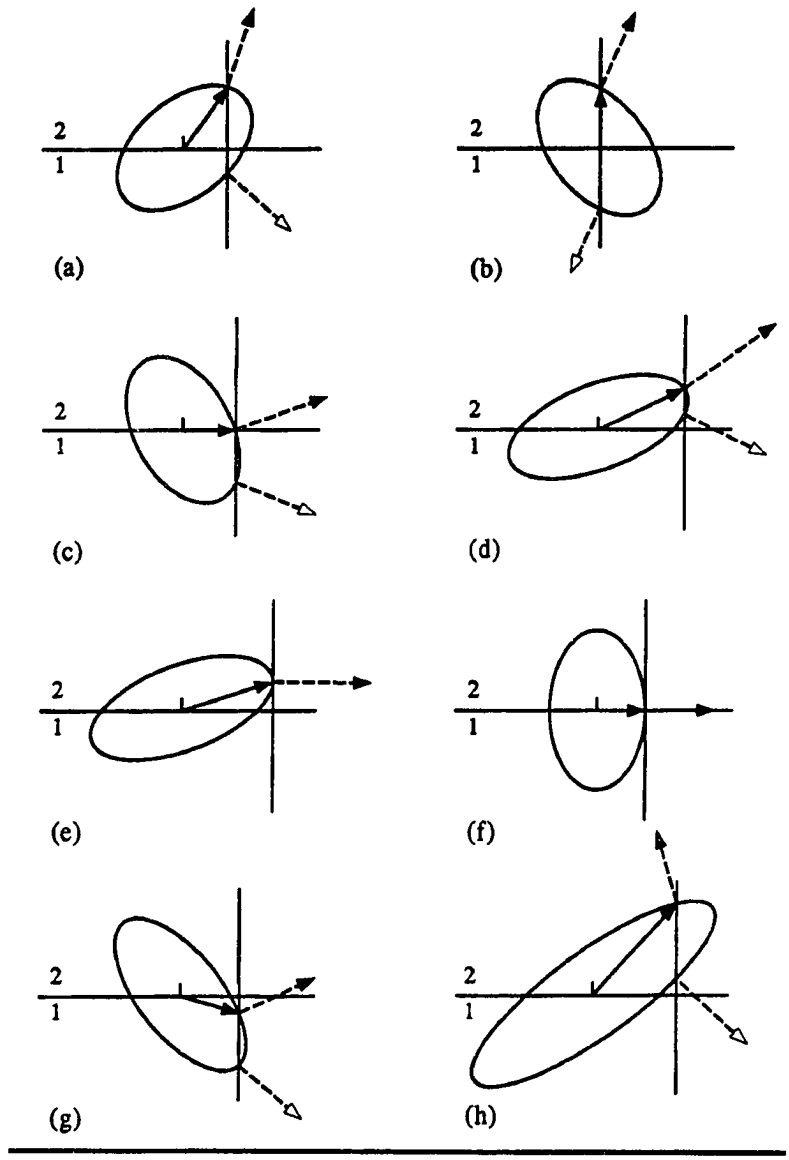

Figure 3.5: Roots of equation (3.5) (scattered phase angles) for negative p when the slowness surface is elliptical. Only the slowness surface in medium 2 is shown. In each case, the incident p is measured from the center of the ellipse to the vertical line. Continuous arrows show the scattered phase directions that correspond to transmitted rays (dashed arrows with a black head). Dashed arrows with a white head show ray directions with the same p but pointing towards medium 1. (a) Most common case. (b) Normal incidence ($p = 0$). (c) Phase direction parallel to the interface, ray not. (d) Two phase directions less than 90 degrees. (e) Ray direction parallel to the interface, phase not. (f). Both ray and phase directions parallel to the interface. (g) Two phase directions greater than 90 degrees. (h) One ray going backwards.

3.6 Two-point ray tracing

In transmission traveltime tomography, we usually need to link every source with the corresponding receiver positions. I do this, with the initial value ray tracing described in sections 3.3 and 3.4, as follows:

1. A sparse fan of rays is traced from the given source position. The aperture of this fan is greater than the aperture of the receiver positions. The end points of these rays (z_{end}) and the shooting angles (α_{init}) are saved.

2. The angle α_{init} that corresponds to a given receiver location is obtained (by using splines interpolation) from the relation α_{init} as a function of z_{end}. This relation is a function almost everywhere. In some places it can be multivalued because the same receiver location can correspond to different shooting angles (all of them greater than the critical angle). The points at which the function is multivalued must be removed before the interpolation. Because of the way the heterogeneities are described, α_{init} as a function of z_{end} always increases or always decreases (except where multivalued at post-critical angles or at triplications).

3. A ray is traced along the newly found α_{init}, and the z_{end} that results is compared to the expected receiver position. If the difference is greater than a predetermined value, I update the table α_{init} as a function of z_{end} is updated with the latest values of α_{init} and z_{end}, and return to step (2). If the difference is smaller than a predetermined value, the ray has been captured.

3.7 Examples

The following examples, show fans of P-wave ray paths in different models for a cross-well configuration. The fans are traced at constant intervals in the phase angle that only correspond to constant intervals in the ray angle when the medium is isotropic. This is shown in Figure 3.6a, where rays have been traced in the simplest model: homogeneous isotropic. When the model is transversely isotropic with vertical axis of symmetry, the density of rays changes with the angle, as Figure 3.6b shows. Figure 3.6c shows the ray paths in a homogeneous transversely isotropic model in which the axis of symmetry is tilted with respect to the vertical ($\gamma = 30$). When two-point ray tracing for the same

receiver positions is performed in the corresponding homogeneous models, we don't see any difference among the three ray path diagrams because the ray angles depend only on the relative positions of source and receivers. The three cases differ only in the traveltimes.

Models like the ones shown in Figure 3.7 may arise from different combinations of deposition, erosion, and rotation of the layers involved. The finely layered areas can be modeled as homogeneous anisotropic layers with axis of symmetry perpendicular to the layering. The only difference between the two models in Figure 3.7 is in the axis of symmetry of the third layer. Figure 3.8 show the rays traced through these models for a source at 3500 feet. The elastic constants for each layer are listed in Table 3.1.

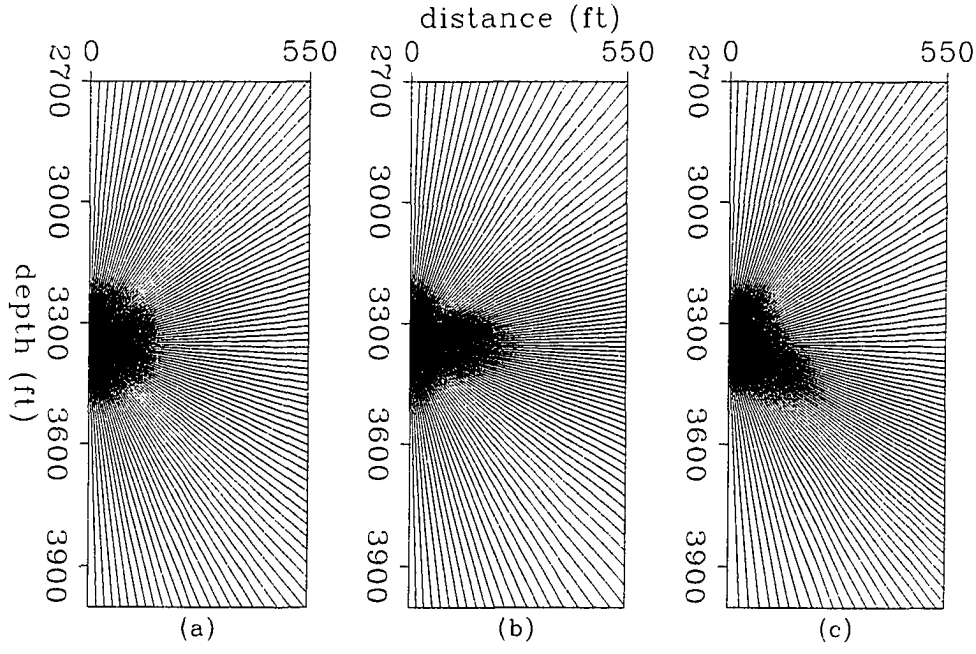

Figure 3.6: P-wave ray paths in different homogeneous models for a source located at 3350 feet. (a) Isotropic. (b) Transversely isotropic with vertical axis of symmetry. (c) Transversely isotropic with $\gamma = -30$. Note how the density of rays with angle changes in the anisotropic models. The elastic constants used in (b) and (c) are $(c_{11}/\rho)^{1/2} = 9894$, $(c_{33}/\rho)^{1/2} = 9005$, $(c_{44}/\rho)^{1/2} = 4949$, and $(c_{13}/\rho)^{1/2} = 5655$, all in (ft/s). The density ρ is assumed to be unity.

To check the accuracy of calculated P- and SV-wave traveltimes, I ran a finite-difference anisotropic elastic modeling algorithm (Karrenbach, 1992) using the layered model shown in Figure 3.9, assuming a VSP geometry with the source at the surface separated 390 feet from the receiver well. The ray tracing was performed on the same model. Figure 3.10

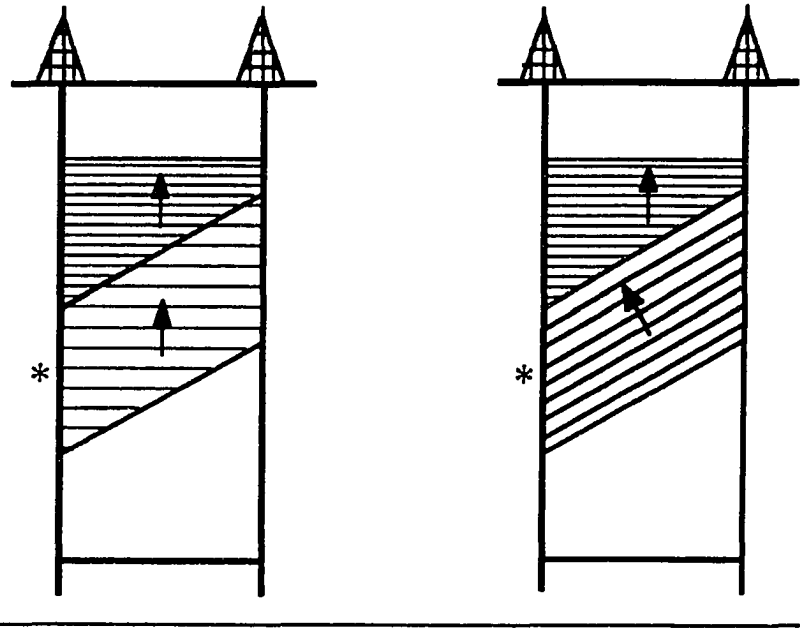

Figure 3.7: Heterogeneous anisotropic models. Two of the four homogeneous blocks are anisotropic with the orientation of the axes of symmetry indicated by the arrows. The axis of symmetry is perpendicular to direction of fine layering. In both models, layers 1 and 4 (from top to bottom) are isotropic. The third block of thin layers in the model at the left ($\gamma = 0$) can be the result of deposition in an eroded boundary whereas the same block in the model at the right ($\gamma = 30$) can be the result of tilting after deposition over a plane boundary. The position of the source is shown by an asterisk ($*$).

Layer 1	Layer 2	Layer 3	Layer 4
$V_{11} = 9005$	$V_{11} = 9894$	$V_{11} = 12545$	$V_{11} = 9005$
$V_{33} = 9005$	$V_{33} = 9005$	$V_{33} = 10845$	$V_{33} = 9005$
$V_{44} = 4949$	$V_{44} = 4949$	$V_{44} = 5968$	$V_{44} = 4949$
$V_{13} = 5655$	$V_{13} = 5655$	$V_{13} = 6805$	$V_{13} = 5655$

Table 3.1: Elastic constants $V_{ij} = \sqrt{c_{ij}/\rho}$ [in (ft/s)] of the models shown in Figure 3.7. In all cases, the elastic constants are referred to the axis of symmetry of the corresponding layer. Layers are counted from top to bottom. The density ρ is assumed to be unity.

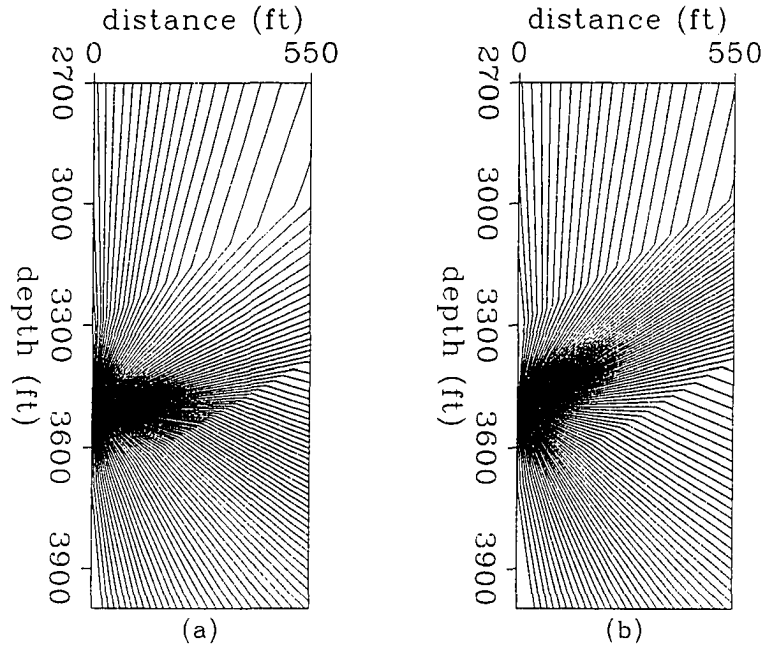

Figure 3.8: P-wave ray paths in the models of Figure 3.7 for a source located at 3500 feet. (a) Vertical axis of symmetry. (b) Tilted axis of symmetry.

shows the results of both the finite-difference elastic modeling and the anisotropic ray tracing. The first arrivals for P- and SV-waves predicted by the finite-difference modeling agree with the traveltimes computed by ray tracing. By picking the appropriate root in equation (3.8), reflections or conversions at the interfaces can also be modeled with ray tracing. Figure 3.10 also shows the traveltimes of reflected arrivals from a selected interface.

3.8 Conclusions

This chapter has reviewed the basic steps for tracing rays in layered transversely isotropic models, emphasising the calculation of the angle of the transmitted phase as a function of the ray parameter of the incident phase. When the angle of incidence is small, I use a different procedure for estimating the angle of the transmitted phase than when the angle of incidence is large. In the latter case, the transmitted phase angles are calculated from the roots of a four-order polynomial in the tangent of the angle for P- and SV-waves and analytically for SH-waves. The appropriate root must reproduce the p of the incident

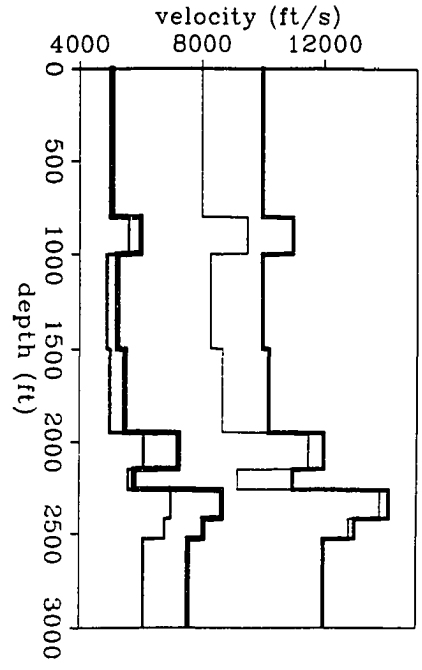

Figure 3.9: Elastic constants (in units of velocity) varying with depth. This model was used to run the ray tracing algorithm and compare the results with those of the finite-difference elastic modeling. From left to right the four curves represent $(c_{44}/\rho)^{1/2}$, $(c_{13}/\rho)^{1/2}$, $(c_{33}/\rho)^{1/2}$, and $(c_{11}/\rho)^{1/2}$, respectively.

phase for the given wave type, producing a ray in the desired direction.

The algorithm is tested by comparing the traveltimes calculated in a heterogeneous transversely isotropic model with those computed by finite-difference elastic modeling. Both sets of traveltimes are in perfect agreement.

In the next chapter, I use this method of anisotropic ray tracing as a part of a more general algorithm to do anisotropic traveltime tomography.

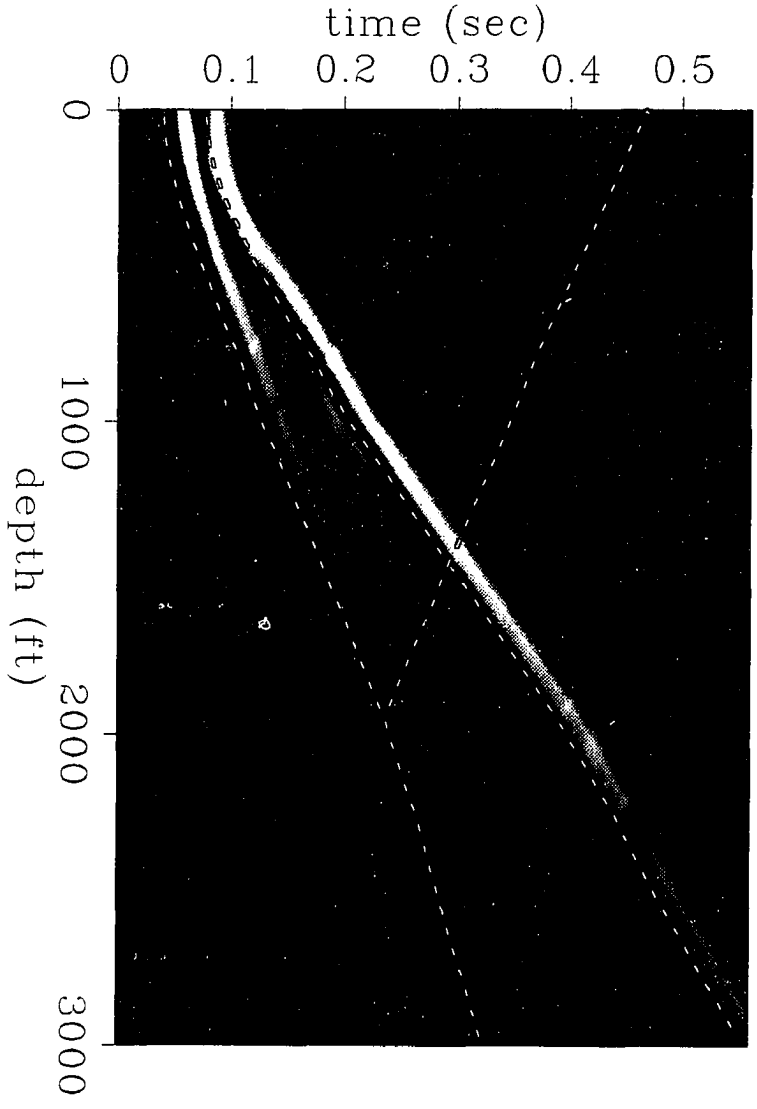

Figure 3.10: Result of the finite-difference elastic modeling through the model shown in Figure 3.9. The dashed lines are created by ray tracing. Traveltimes of P-wave reflected arrivals from one interface have been also calculated by ray tracing.

Chapter 4

Tomographic estimation of elliptical velocities

To estimate elastic constants from traveltime measurements it is first necessary to fit the traveltimes with elliptical velocity functions. As described in chapter 2, when the model is homogeneous and the axis of symmetry is vertical, only two parameters for each wave type are needed to describe the elliptical velocity functions. When the model is heterogeneous, however, the elliptical velocity functions need to be estimated at each point in space. Thus the problem of estimating them, which in homogeneous media is highly overdetermined, becomes in heterogeneous media a highly underdetermined problem. This chapter describes a tomographic approach for solving it. The underdeterminedness is resolved by using models for the heterogeneities that contain information about the expected variations in the medium. I show synthetic and field data examples that illustrate the application of the technique, which uses the anisotropic ray tracing algorithm developed in chapter 3.

4.1 Introduction

Depending on the degree of anisotropy and fine layering of the medium, tomograms obtained from cross-well traveltime data under an isotropic assumption may be significantly in error. These errors are analogous to the mispositions obtained with surface seismic methods when, in an anisotropic environment, stacking velocities are used to convert times into depths. The need to eliminate these errors provides one reason for using an anisotropic model in tomographic traveltime inversion. Another reason is that we are

solving more than an imaging problem, since it is well known that anisotropy is a useful tool for studying lithology and the degree of stratification in sedimentary rocks. Taking velocity anisotropy into account in tomographic traveltime inversion helps us to gain useful information about reservoir and nonreservoir rocks.

Additional subsurface information (e.g., layer depths or vertical slownesses) is required for estimating anisotropy from surface seismic measurements (Levin, 1978). For this reason, in recent studies where anisotropy has been quantified, either a different geometry like VSP has been used (Byun and Corrigan, 1990; White et al., 1983) or the surface seismic information has been combined with well-logs (Banik, 1984). Observing that velocity anisotropy does not affect *P*-wave horizontal moveout considerably, Winterstein (1986) estimated the required layer thicknesses using velocities obtained form *P*-wave velocity analysis. Then, from *SH*-wave velocity analysis, he was able to estimate velocity anisotropy.

The main difference between tomographic velocity estimation from surface measurements and cross-well or VSP traveltimes is that the former requires a priori knowledge of reflector positions whereas the other methods do not. The only positions needed to estimate velocities from direct path, cross-well traveltimes are the source and receiver locations. Eliminating reflector mapping from the problem may make the estimation of other effects such as velocity anisotropy simpler in the cross-well environment. However, fewer attempts have been made to estimate velocity anisotropy from cross-well measurements. Stewart (1988) and Williamson et al. (1993) has proposed a modification to methods based on algebraic reconstruction techniques to include the effect of anisotropy. By using the weak anisotropy expression for the phase velocities given by Thomsen (1986) to fit the traveltimes, Stewart and Williamson et al. appear to assume the equality of group and phase velocities, which is, in general, not true. McCann et al. (1989) show how an isotropic inversion improved after assuming a fixed amount of anisotropy. Winterstein and Paulsson (1990) have estimated a vertical velocity gradient from VSP and cross-well data assuming a transversely isotropic model. Chapman and Pratt (1992) and Pratt and Chapman (1992) estimated velocity anisotropy in a general 2-D medium assuming weak anisotropy in order to justify isotropic ray tracing. Saito (1991) and Lines (1992) proposed to separate the effects of anisotropy and heterogeneity by first "removing" the anisotropy effects from the data so that conventional isotropic tomography in heterogeneous media can later be applied.

As I show in chapter 2, a general TI medium can be approximated by fitting *P*- and *S*-wave traveltimes with ellipses either around the horizontal or around the vertical (assuming a vertical axis of symmetry). Muir (1990), and Dellinger et al. (1993) show that when *P*- and *S*-wave traveltimes around both the horizontal and the vertical are available, a general TI medium can also be approximated by fitting the data with ellipses. What is needed to use these two different approximations in heterogeneous media is a procedure to find the parameters that describe the ellipses as a function of the position. This chapter focuses on such a procedure.

I show in this chapter how to fit tomographically transmitted traveltimes with heterogeneous elliptically anisotropic models. When *P*- and *S*-wave traveltimes are available, the images obtained can be transformed into elastic constants of a TI media as explained in chapter 2. I also show that if only one wave type is available, the images obtained can still provide useful information about the medium. The model of heterogeneities is required to be piecewise continuous and the formulation is identical for any wave type. No assumptions are made about the weakness of either anisotropy or heteroneneities.

Certain types of azimuthally anisotropic media can approximated with the model of velocity and heterogeneity used in this chapter, in particular those formed by dipping transversely isotropic layers. This is done by also considering as a variable the inclination of the axis of symmetry. The estimation of this variable may help the interpreter to characterize the amount of structural deformation that has undergone the different formations in the reservoir and may also help in the identification of structural unconformities.

I have studied the effects of the limited view of the measurements (from cross-well geometries) in the estimation of both slowness components for different models of heterogeneity, concluding that the technique is stable and accurate when used to invert 1-D (layered) models if the range of ray angles is "wide enough." In 2-D models, the estimation of lateral variations in the vertical component of the slowness is particularly difficult from cross-well geometries alone. Consequently, 2-D spatial variations in velocity anisotropy cannot be estimated at the same resolution as that of variations in velocity. I also show that when iterative techniques such as conjugate gradients are used to estimate the anisotropic parameters, early termination of the iterations (a way to damp the solution) may produce artificial anisotropy. This problem worsens in two dimensions.

A theoretical discussion of the technique is followed by examples with cross-well synthetic data and field data from an Amoco Gulf Coast site and the British Petroleum (BP)

Devine test site.

4.2 Forward modeling

The traveltime for a ray that travels a distance d in a homogeneous medium with elliptical anisotropy and the axis of symmetry forming an angle γ with respect to the vertical (Figure 4.1) is

$$t = \sqrt{\frac{(\Delta x \cos\gamma + \Delta z \sin\gamma)^2}{V_\perp^2} + \frac{(-\Delta z \cos\gamma + \Delta x \sin\gamma)^2}{V_\parallel^2}}, \tag{4.1}$$

where $\sqrt{\Delta x^2 + \Delta z^2} = d$, and $V_\parallel$ and $V_\perp$ are the velocities in the directions parallel and perpendicular, respectively, to the axis of symmetry. Appendix C explains how to derive this expression.

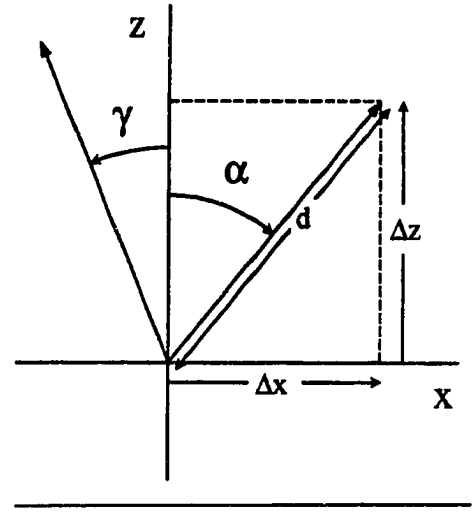

Figure 4.1: Ray traveling a distance d in a medium with a tilted axis of symmetry. α and γ are the angles (positive counterclockwise) of the ray and the axis of symmetry, respectively, in relation to the vertical.

If the model is described as a superposition of N homogeneous orthogonal regions, the traveltime for the i^{th} ray traveling across the j^{th} region is

$$t_{i,j} = \sqrt{\frac{(\Delta x_{i,j} \cos\gamma_j + \Delta z_{i,j} \sin\gamma_j)^2}{V_{\perp_j}^2} + \frac{(-\Delta z_{i,j} \cos\gamma_j + \Delta x_{i,j} \sin\gamma_j)^2}{V_{\parallel_j}^2}}. \tag{4.2}$$

Note that each homogeneous region is characterized by three parameters: two velocities and the angle of the axis of symmetry with respect to the vertical. From here on I refer to

these parameters as interval parameters. In the preceding equation, $\sqrt{\Delta x_{i,j}^2 + \Delta z_{i,j}^2}$ is the distance traveled by the i^{th} ray in the j^{th} cell. The sum of expressions like equation (4.2) can be used to compute the traveltime from source to receiver for a ray that travels in a heterogeneous medium, assuming that the ray path is known. In chapter 3, I explain how to do the anisotropic ray tracing.

Figure 4.2 shows an example of the type of model I consider in this chapter. It consists of homogeneous elliptically anisotropic blocks separated by straight interfaces with variable dip (a_j) and intercept (b_j). I assume that all axes of symmetry of the different layers lie in the plane of the survey. If $\Delta x_{i,j}$ and $\Delta z_{i,j}$ are defined as

$$\Delta x_{i,j} = x_{i,j+1} - x_{i,j}, \tag{4.3a}$$

$$\Delta z_{i,j} = z_{i,j+1} - z_{i,j}, \tag{4.3b}$$

the expression (4.2) for the traveltime $t_{i,j}$ of the i^{th} ray in the j^{th} cell becomes

$$t_{i,j} = \sqrt{\Delta X_{i,j}{}^2 S_{\perp_j}^2 + \Delta Z_{i,j}{}^2 S_{\|_j}}, \tag{4.4}$$

where $S_{\perp_j}$, $S_{\|_j}$, $\Delta X_{i,j}$, and $\Delta Z_{i,j}$ are equal to

$$S_{\perp_j} = \frac{1}{V_{\perp_j}},$$

$$S_{\|_j} = \frac{1}{V_{\|_j}},$$

$$\Delta X_{i,j} = \Delta x_{i,j} \cos\gamma_j + (a_{j+1} x_{i,j+1} + b_{j+1} - a_j x_{i,j} - b_j) \sin\gamma_j,$$

$$\Delta Z_{i,j} = -(a_{j+1} x_{i,j+1} + b_{j+1} - a_j x_{i,j} - b_j) \cos\gamma_j + \Delta x_{i,j} \sin\gamma_j.$$

The point $(x_{i,j},\ z_{i,j})$ is the intersection between the i^{th} ray and the j^{th} interface. If the axis of symmetry is vertical ($\gamma_j = 0$), it follows that $\Delta X_{i,j} = \Delta x_{i,j}$ and $\Delta Z_{i,j} = \Delta z_{i,j}$.

Besides the interval parameters previously introduced, I have added two more parameters to describe how the boundaries that separate different intervals may change their positions. I call them boundary parameters. Figure 4.2 shows how to count both intervals and boundaries.

The total traveltime for a ray that travels from source to receiver is

$$t_i(\boldsymbol{m}) = \sum_{j=1}^{N} t_{i,j}(\boldsymbol{m}) \qquad i = 1, ..., M, \tag{4.5}$$

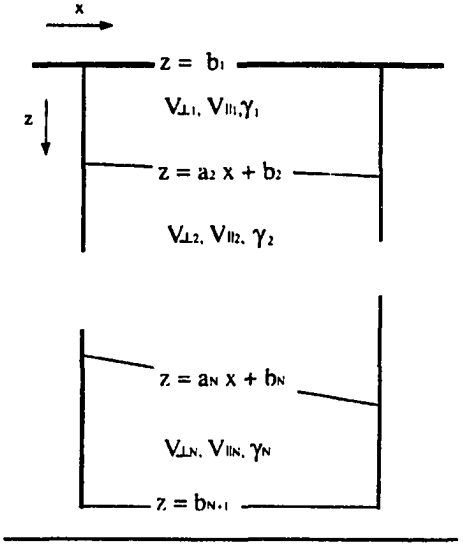

Figure 4.2: Model of velocities and heterogeneities. The top and bottom interfaces are horizontal ($a_1 = a_{N+1} = 0$) and located at known depths. This model is neither 1-D nor fully 2-D, but something in between. Therefore, I call it 1.5-D.

where $\boldsymbol{m}$ is the vector of model parameters of $5N$ elements:

$$\begin{aligned} \boldsymbol{m} &= (m_1, ..., m_N, m_{N+1}, ..., m_{2N}, m_{2N+1}, ..., m_{3N}, m_{3N+1}, ..., m_{4N}, m_{4N+1}, ..., m_{5N}) \\ &= (S_{\perp_1}, ..., S_{\perp_N}, S_{\|_1}, ..., S_{\|_N}, \gamma_1, ..., \gamma_N, b_1, ..., b_N, a_1, ..., a_N), \end{aligned} \tag{4.6}$$

and M is the total number of traveltimes. The dimension of $\boldsymbol{m}$ can be reduced if some of the parameters remain fixed during the inversion. For example, if the axes of symmetry are known to be vertical, the components $\gamma_1, ..., \gamma_N$ are not used or if the position of the cells is fixed (e.g., when discretizing the model using square pixels), the parameters $b_1, ..., b_N, a_1, ..., a_N$ are not used either.

Equation (4.5) is the system of nonlinear equations that relates the model parameters to the measured traveltimes. A linearized version of these equations is used in the next section to solve the inverse modeling problem. When the medium is isotropic (i.e., $S_{\perp_j} = S_{\|_j} = S_j$), equation (4.5) reduces to the familiar expression that approximates traveltimes computed in an isotropic model (McMechan, 1983):

$$\begin{aligned} t_i &= \sum_{j=1}^{N} S_j \sqrt{\Delta x_{ij}{}^2 + \Delta z_{ij}{}^2} \\ &= \sum_{j=1}^{N} S_j d_{ij}, \end{aligned}$$

where d_{ij} is the length of the i^{th} ray in the j^{th} cell.

4.3 Inverse modeling

In order to understand how to do the decoupling of anisotropy and heterogeneity (when both effects can be separated), let us consider first the case of homogeneous elliptically anisotropic media with a vertical axis of symmetry ($S_\perp = S_x$ and $S_{||} = S_z$). From studying this case, it is possible to draw some general conclusions about the estimation of velocities that vary with both direction and position.

4.3.1 Homogeneous media

When the model is homogeneous and isotropic, we usually estimate the slowness S of the homogeneous medium that "best" fits the traveltimes by simply averaging all the slownesses S_i obtained from the individual rays as follows:

$$S = \frac{1}{M}\sum_{i=1}^{M} S_i = \frac{1}{M}\sum_{i=1}^{M} \frac{t_i}{l_i}, \tag{4.7}$$

where l_i is the source-receiver distance and M the total number of traveltimes.

When the model is homogeneous and elliptically anisotropic, the two slowness components S_x and S_z that best fit the traveltimes can be obtained by generalizing the average (4.7). This generalization is, as expected, in a least-squares sense. From expression (4.1) we can see that the relation between t^2 and S_x^2 and S_z^2 is linear. Therefore, for a given set of traveltimes and source-receiver locations, it is possible to set up a least-squares problem to find the vector $\boldsymbol{m} = (S_x, S_z)$ of the homogeneous medium. Defining $M_x = S_x^2$ and $M_z = S_z^2$, the least-squares problem is

$$\underset{\sim}{\mathbf{M}} \begin{pmatrix} M_x \\ M_z \end{pmatrix} = \boldsymbol{d}, \tag{4.8}$$

where

$$\underset{\sim}{\mathbf{M}} = \begin{pmatrix} {\Delta x_1}^2 & {\Delta z_1}^2 \\ {\Delta x_2}^2 & {\Delta z_2}^2 \\ \vdots & \vdots \\ {\Delta x_M}^2 & {\Delta z_M}^2 \end{pmatrix},$$

and

$$\boldsymbol{d} = \begin{pmatrix} t_1^2 \\ t_2^2 \\ \vdots \\ t_M^2 \end{pmatrix}.$$

Equation (4.8) can be solved in different ways. The most common approach is to use the normal equations, which results in

$$\begin{pmatrix} M_x \\ M_z \end{pmatrix} = (\underset{\sim}{\mathbf{M}}^T \underset{\sim}{\mathbf{M}})^{-1} \underset{\sim}{\mathbf{M}}^T \boldsymbol{d}. \tag{4.9}$$

However, the normal equations may have undesirable features with respect to numerical stability, because the condition number of $\underset{\sim}{\mathbf{M}}^T\underset{\sim}{\mathbf{M}}$ is the square of the condition number of $\underset{\sim}{\mathbf{M}}$. If $\underset{\sim}{\mathbf{M}}$ is only moderately ill-conditioned, $\underset{\sim}{\mathbf{M}}^T\underset{\sim}{\mathbf{M}}$ is severely ill-conditioned. For this reason, methods that do not amplify the condition number of $\underset{\sim}{\mathbf{M}}$ should be used to solve systems like (4.8) (e.g., QR factorization).

For estimating M_x and M_z *simultaneously* and *accurately*, $\underset{\sim}{\mathbf{M}}$ has to be well conditioned. This is not the case when most of the elements of the matrix satisfy either $\Delta x_i^2 \gg \Delta z_i^2$ or $\Delta z_i^2 \gg \Delta x_i^2$. These two inequalities describe cases in which most rays are traveling close to the horizontal or the vertical. In such cases, it is difficult to estimate simultaneously both components of the vector $\boldsymbol{S}$ because the limited view of the measurements results in severe ill-conditioning. This can be understood by trying to estimate M_x and M_z using the simple cross-well experiment shown in Figure 4.3, where $\Delta x^2 \gg \Delta z_i^2$. In this case

$$\underset{\sim}{\mathbf{M}} = \begin{pmatrix} \Delta x^2 & \Delta z_1^2 \\ \Delta x^2 & \Delta z_2^2 \end{pmatrix}.$$

The eigenvalues of this matrix are

$$\lambda_{\pm} = \frac{\Delta x^2 + \Delta z_2^2 \pm \sqrt{(\Delta x^2 - \Delta z_2^2)^2 + 4\Delta x^2 \Delta z_1^2}}{2}.$$

Since $\Delta x^2 \gg \Delta z_i^2$, the eigenvalues to the first order are

$$\lambda_+ \approx \Delta x^2 + \Delta z_1^2,$$
$$\lambda_- \approx \Delta z_2^2 - \Delta z_1^2.$$

The largest eigenvalue of $\underset{\sim}{\mathbf{M}}$ is related to the horizontal component of the slowness, and the smallest one is related to the vertical component. In contrast, for a VSP-like geometry, the

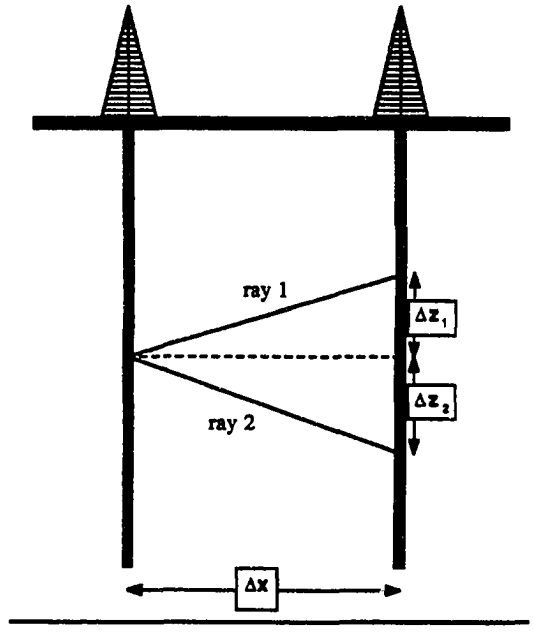

Figure 4.3: Cross-well experiment with two rays.

largest eigenvalue is related to S_z and the smallest one to S_x (Dellinger, 1989). Increasing the number of rays M without increasing the aperture does not solve the problem. In such a case, the largest eigenvalue of the matrix $(\underset{\sim}{\mathbf{M}}^T \underset{\sim}{\mathbf{M}})$ tends to $\sum_{i=1}^{M} \Delta x_i^4$ and the smallest one tends to zero again.

Having seen the difficulties of trying to estimate variations of velocity with direction in homogeneous media, let's look at what happens when we try to do the same in heterogeneous media.

4.3.2 Heterogeneous media

When estimating velocities tomographically in heterogeneous media, the goal is to estimate two different sets of coupled unknowns: the model parameters and the ray paths. The usual way to decouple them is by invoking Fermat's principle, which "justifies" the trick of assuming one to estimate the other in an iterative fashion, as long as the magnitude of the changes from one step to the next are kept small.

Once we have estimated the ray paths, we need to solve the system of nonlinear equations (4.5) in order to find a new model in which rays are again traced. One way

to solve (4.5) is as a sequence of linearized steps starting from a given initial model $\boldsymbol{m}_0$. The first step is to approximate such an equation by its first-order Taylor series expansion centered about a given model $\boldsymbol{m}_0$:

$$\begin{aligned} t_i(\boldsymbol{m}) &\approx t_i(\boldsymbol{m}_0) + \nabla t_i(\boldsymbol{m}_0) \cdot (\boldsymbol{m} - \boldsymbol{m}_0) \\ &= t_i(\boldsymbol{m}_0) + \sum_{n=1}^{5N} \underset{\sim}{\mathbf{J}}_{in} (m_n - m_{0n}), \end{aligned} \tag{4.10}$$

where the elements of the Jacobian $\underset{\sim}{\mathbf{J}}_{in}$ are

$$\underset{\sim}{\mathbf{J}}_{in} = \left. \frac{\partial t_i}{\partial m_n} \right|_{\boldsymbol{m}=\boldsymbol{m}_0}.$$

The explicit forms of these derivatives are given in appendix D. In contrast with the Jacobian for the isotropic case, the matrix $\underset{\sim}{\mathbf{J}}$ when the medium is anisotropic depends *explicitly* on the interval parameters of the reference model $\boldsymbol{m}_0$. In the isotropic case, the Jacobian depends only on the lengths of the rays at each pixel, and, therefore, when the rays are straight the estimation of slowness becomes a linear problem because the Jacobian is constant. In the anisotropic case, however, the problem is still nonlinear even if the rays are straight. Ray bending introduces an additional type of nonlinearity into the problem.

If we assume that $t_i(\boldsymbol{m})$ represents one component of the vector $\boldsymbol{t}$ of measured traveltimes, we can compute the perturbations $\Delta \boldsymbol{m}_n = (m_n - m_{0n})$ once the traveltimes in the reference model $\boldsymbol{m}_0$ have been calculated. The perturbation $\Delta \boldsymbol{m} = (\boldsymbol{m} - \boldsymbol{m}_0)$ is the solution of the following system of equations:

$$\underset{\sim}{\mathbf{J}} \Delta \boldsymbol{m} = \Delta \boldsymbol{t}, \tag{4.11}$$

where $\Delta t_i = t_i(\boldsymbol{m}) - t_i(\boldsymbol{m}_0)$. In practice, only a fraction r of the correction $\Delta \boldsymbol{m}$ is added to the given model:

$$\boldsymbol{m}_1 = (\boldsymbol{m}_0 + r \Delta \boldsymbol{m}),$$

where r (the step length) is usually kept small to avoid large changes in the ray paths from one iteration to the next.

In appendix A, I compute the singular value decomposition (SVD) of the matrix $\underset{\sim}{\mathbf{J}}$ for the following models with fixed interfaces: 1-D isotropic, 1-D anisotropic, 2-D isotropic and 2-D anisotropic. The results are roughly a combination of the results I derived in

the section "Homogeneous media" and the results previously published for isotropic heterogeneous media (Bregman et al., 1989; Pratt and Chapman, 1992); that is, the more sensitive part of the model related to the largest singular values of the Jacobian, corresponds roughly to vertical variations in the horizontal component of the slowness, whereas the less sensitive part of the model corresponds to horizontal and high-frequency variations in the vertical component of the slowness. As a consequence, in two dimensions, S_x and S_z cannot be estimated with the same resolution because a large part of the variations in S_z are in the null space of the problem. In one dimension, S_x and S_z can be estimated with the same resolution only when the smallest singular values of the problem can be also retrieved. The last section of this chapter shows examples that illustrate this issue.

Based on the observations derived from the SVD that estimating anisotropy and heterogeneities in 1-D models is by far an easier problem than in 2-D models, I consider intermediate models like the one shown in Figure 4.2 where the only type of lateral variations allowed in the model are as straight interfaces with variable dip and intercept.

In the examples shown later, the system of linear equations (4.11) is solved using the LSQR variant of the conjugate gradients algorithm (Nolet, 1987), which has been proved to be faster than SIRT methods (Nolet, 1985; Van der Sluis and Van der Vorst, 1987).

4.3.3 Constraints

Prior information about the real medium can be introduced in the inversion in two ways: with the starting model and with bounds on the variations of the parameters being estimated. In this particular algorithm, both these forms of prior information are *essential* for a reliable estimation of the vector $\boldsymbol{m}$.

If the starting model is "far" from the "true" answer the algorithm may not converge at all, or, if it does, it may produce a wrong answer. Although this problem may happen with any nonlinear inversion, it can be shown that if the starting model is "close" to the true answer, a linearized solution of the nonlinear system of equations (4.5) converges quadratically (Gill et al., 1981). Therefore, any information introduced in the initial model (especially about dips) helps the algorithm converge to a more reliable estimate of the actual medium.

When the interfaces are allowed to change position from one iteration to the next, the algorithm has to ensure that each new model does not contain crossing interfaces in the area of interest. If two interfaces cross after adding $r\Delta\boldsymbol{m}$ to the given model, the

step length r is reduced until those interfaces do not cross after the correction. Once the model is updated and no crossing interfaces are found, the algorithm checks whether thin layers have been created or not, and, if so, those layers are eliminated from the inversion, reducing by a multiple of five the number of model parameters (five parameters for each layer eliminated). The layers are eliminated by comparing their thicknesses with a predetermined minimum layer thickness, as long as the corresponding boundaries are parallel (also within a predetermined range of angles). If the predetermined minimum thickness is too small, the solution may contain layers with artificially high (or low) velocities, and if the minimum is too big, spatial resolution in the model may be lost.

Whenever information is available about the position and dip of certain layers of the medium (from well logs, for example) it should also be used to constrain the corresponding interfaces in the model.

When appropriate, especially in 2-D models, the solution should also be required to be smooth.

4.3.4 Which is the axis of symmetry?

Every ellipse has two axes of symmetry. The inversion algorithm proposed in this chapter can estimate the inclination with respect to the vertical of either one, depending on which axis is closer to the vertical in the initial model. In either case, the estimated parameters describe the same *elliptical velocity function.*

Another way to understand why the inversion can estimate the inclination of either axis of symmetry is to examine the traveltime equation (4.1). We can obtain an identical equation if in (4.1) we switch $V_{||}$ and $V_{\perp}$, changing at the same time γ by $\gamma \pm \pi/2$. This means that the traveltimes are affected only by the elliptical function of velocities, regardless of how such a function is described. Figure 4.4 shows how a given ellipse can be described with two different sets of parameters.

If the inversion procedure is constrained to estimate the same axis of the ellipse (either the major or the minor) for every layer, it can be more difficult (or impossible) to get a reliable estimate of the real elliptical velocity function of the medium, especially in cases when the axis of symmetry in the initial model is far from the actual axis of symmetry.

Because of this property of ellipses, it is easier for the algorithm to estimate inclinations of axes of symmetry close to the vertical or close to the horizontal than intermediate inclinations that are not close to either axis.

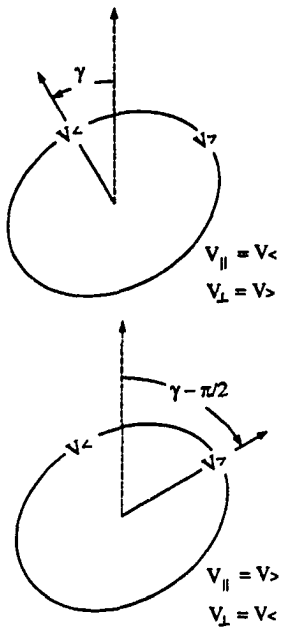

Figure 4.4: The same ellipse represented in two different ways by interchanging $V_\perp$ and $V_{||}$ and rotating the axis of symmetry $-\pi/2$. Traveltimes are affected by the velocity function (elliptical in this case) regardless of how that function is described.

4.4 Synthetic examples

In this section, I show the application of the inversion algorithm just described in different situations that demonstrate its advantages and weaknesses when used to invert cross-well traveltimes. First, I consider the case of traveltimes generated in a 1-D isotropic model that are inverted using a 1-D anisotropic model with fixed boundaries and vertical axes of symmetry. This first example, which can be considered a linear inversion because the velocity variations are nearly one percent, illustrates several issues related to the convergency of the algorithm. Second, I show what happens when the assumption of layering is relaxed and a full 2-D anisotropic inversion is performed with data generated in a weakly varying 2-D isotropic model. Finally, I show an example of the inversion that uses the intermediate 1.5-D model shown in Figure 4.2. Unlike the first two examples, the final example doesn't assume either weak heterogeneity or weak anisotropy, and the orientation of the axis of symmetry varies through the model. All the models are assumed to be elliptically anisotropic. Chapter 5 addresses the more general case of transversely isotropic models.

4.4.1 1-D inversion

Synthetic data were generated through the 1-D isotropic model shown in Figure 4.5, using a geometry of 17 sources and 17 receivers equally spaced at the source and receiver well, respectively.

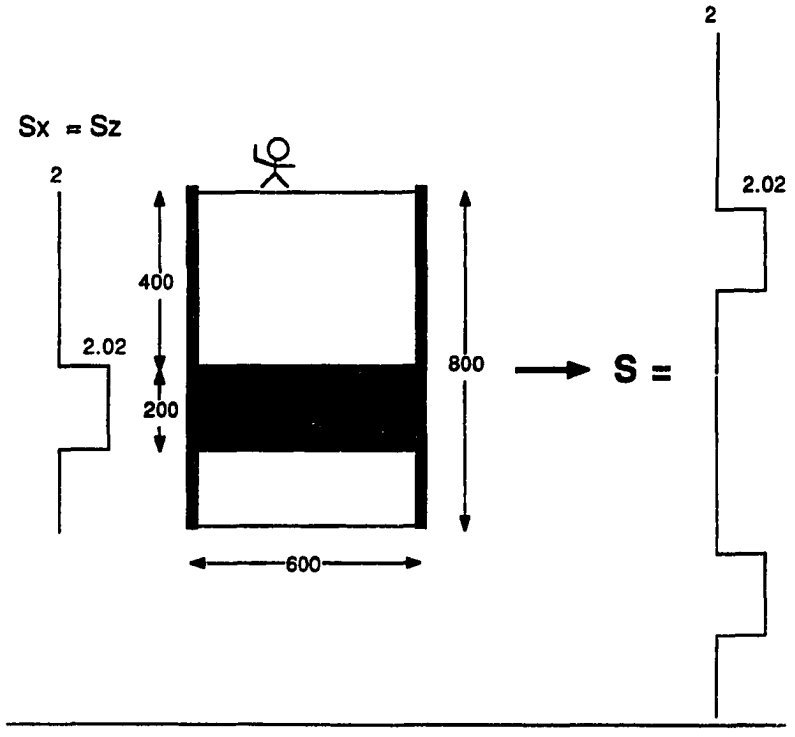

Figure 4.5: 1-D isotropic model used to test the algorithm. At the right, the two components of the slowness are plotted one after the other. They represent the slowness vector that describes this model. The first half of the vector corresponds to the horizontal component and the second half to the vertical.

The inversion is constrained by allowing only vertical variations in the model. This constraint eliminates instabilities and nonuniqueness in the inversion associated with lateral variations, retaining only those variations associated with the vertical component of the slowness, which is not sampled sufficiently by the cross-well recording geometry. The constraint also reduces the dimension of $\boldsymbol{m}$ to $2N$ instead of $5N$. I call the reduced vector $\boldsymbol{S}$, instead of $\boldsymbol{m}$, to suggest that it only contains information about the slownesses at each layer, and not about the positions of the boundaries and orientations of the axes of symmetry.

If we plot components of the slowness vector $\boldsymbol{S}$ [equation (4.6)] for this model, we obtain the profile shown at the right side of Figure 4.5. Both slowness components are identical because the model is isotropic. In this example, the slowness contrast between the background and the anomalous layer is small (one percent), and therefore the propagation of the energy can be safely modeled by straight ray paths.

The image area was divided into 100 layers of equal thickness (8 feet). The inversion process has to estimate 200 parameters from 289 traveltimes. Figure 4.6 shows the slowness vector obtained after 60 conjugate gradients (CG) iterations. There is no difference between the given $\boldsymbol{S}$ (Figure 4.5) and the estimated one (Figure 4.6). Note that the results can be represented either as a function of depth or as a function of the index of the slowness vector. In the two next results the depth axis is omitted.

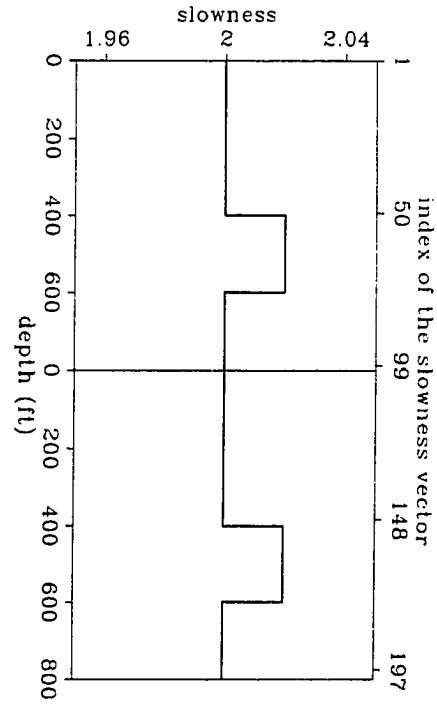

Figure 4.6: Result of the inversion of the synthetic data generated with the model shown in Figure 4.5. The first half of the curve corresponds to the horizontal component of slowness and the second half to the vertical component.

Figure 4.7 shows how the algorithm converges toward the answer as a function of the CG-iterations. The result shown in Figure 4.6 corresponds in Figure 4.7 to 60 CG-iterations along the axis *cg iterations*. The two "hills" represent the slowness at the anomalous layer. Convergence is achieved when the top and the bottom of the hills are

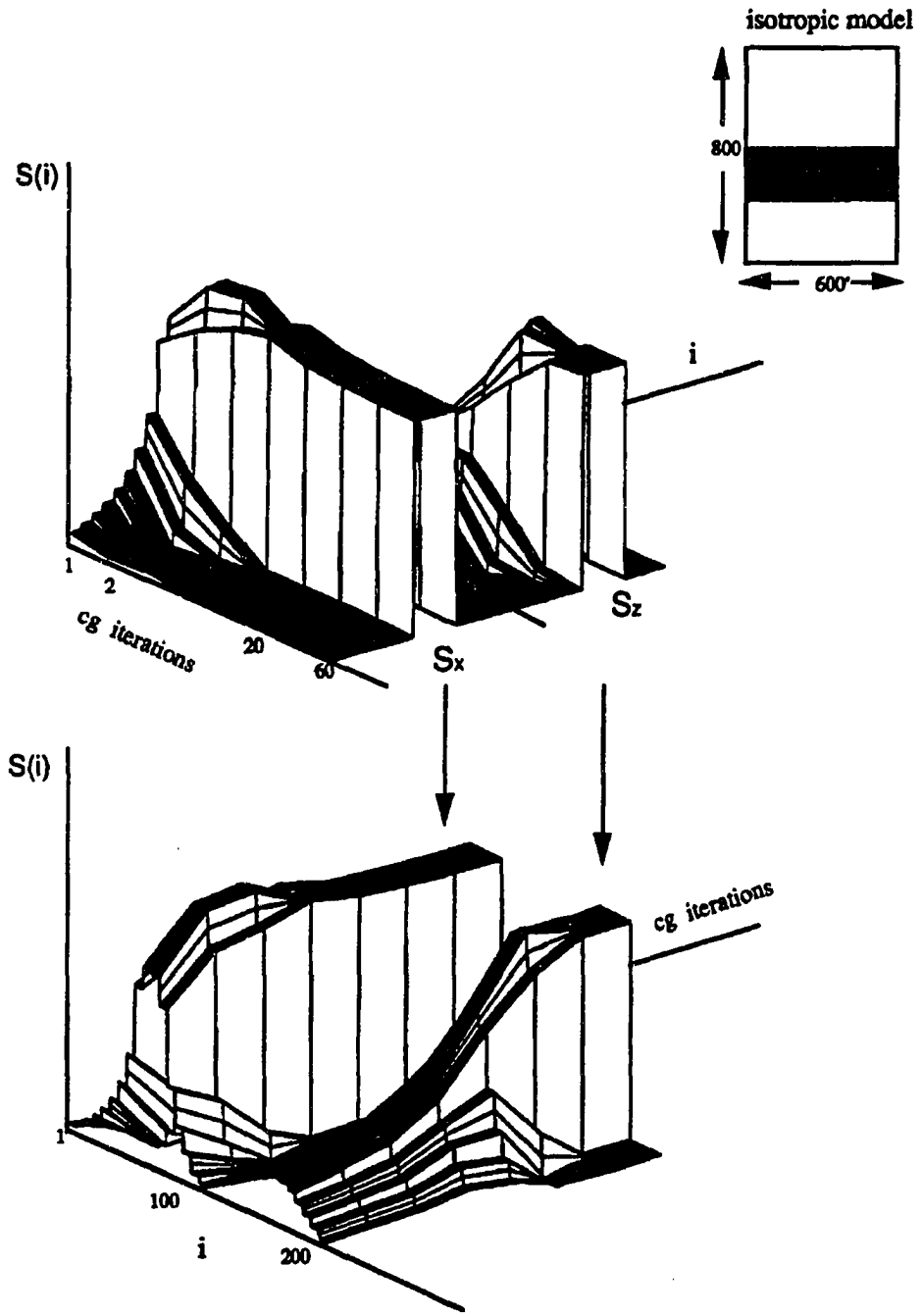

Figure 4.7: Variations of the slowness vector as a function of the number of conjugate gradient iterations. The original model is shown at the top. The axes "i" and "cg iterations" have been interchanged from the top to the bottom plot.

flat for an increasing number of CG-iterations. The horizontal component of the slowness converges faster than the vertical component. This is because in the given model the horizontal component of the slowness in the anomalous layer is better sampled than the vertical component: the range of ray angles (absolute values) is from 0 to 53 degrees [$53 \approx \arctan(\frac{800}{600})$], which is a typical range for cross-well experiments. Because of this bias of cross-well geometries toward the horizontal, the largest singular values of the problem (1-D anisotropic) are related to the horizontal component of the slowness, as appendix A shows.

When synthetic data is generated through the model shown at the top of Figure 4.8 (where the well-to-well separation is shorter), both components converge at the same rate. This is because the vertical component of the slowness is better sampled in this example because the range of ray angles is wider. The angles vary between 0 and 76 degrees [$76 \approx \arctan(\frac{800}{200})$].

The preceding results tell us that if it is not possible to do "enough" CG-iterations in order to reach the flat top of both hills (Figures 4.7 and 4.8), we may wrongly conclude that the medium is anisotropic because components of the slowness in different directions may converge with different speeds. Severely limited view problems as well as low signal-to-noise ratios are some of the factors that may limit the amount of CG-iterations that can be performed before the smallest singular values of the problem start affecting the solution.

4.4.2 2-D inversion

To test the performance of the algorithm in inverting data generated in a 2-D model, I computed synthetic traveltimes through the isotropic model shown in Figure 4.9. The separation between contiguous sources and receivers is 10 feet. Each receiver gather only uses sources located at ± 50 degrees from the horizontal. With a geometry like this, I simulate the geometry of a field data examples to be analyzed later. As in the previous example in 1-D, the slowness contrast between the anomaly and the background is small (five percent), and therefore straight rays can be used again.[1]

The unknown model was discretized in 241 $\times$ 46 pixels (5 $\times$ 5 ft^2 each), and therefore

[1] My implementation of the anisotropic ray tracing algorithm described in chapter 3 is not valid for 2-D anisotropic models described as a superposition of square pixels. However, if the rays are assumed to be straight because of small velocity contrasts, tracing rays in elliptically anisotropic models is reduced to computing the corresponding traveltimes by using equation 4.5.

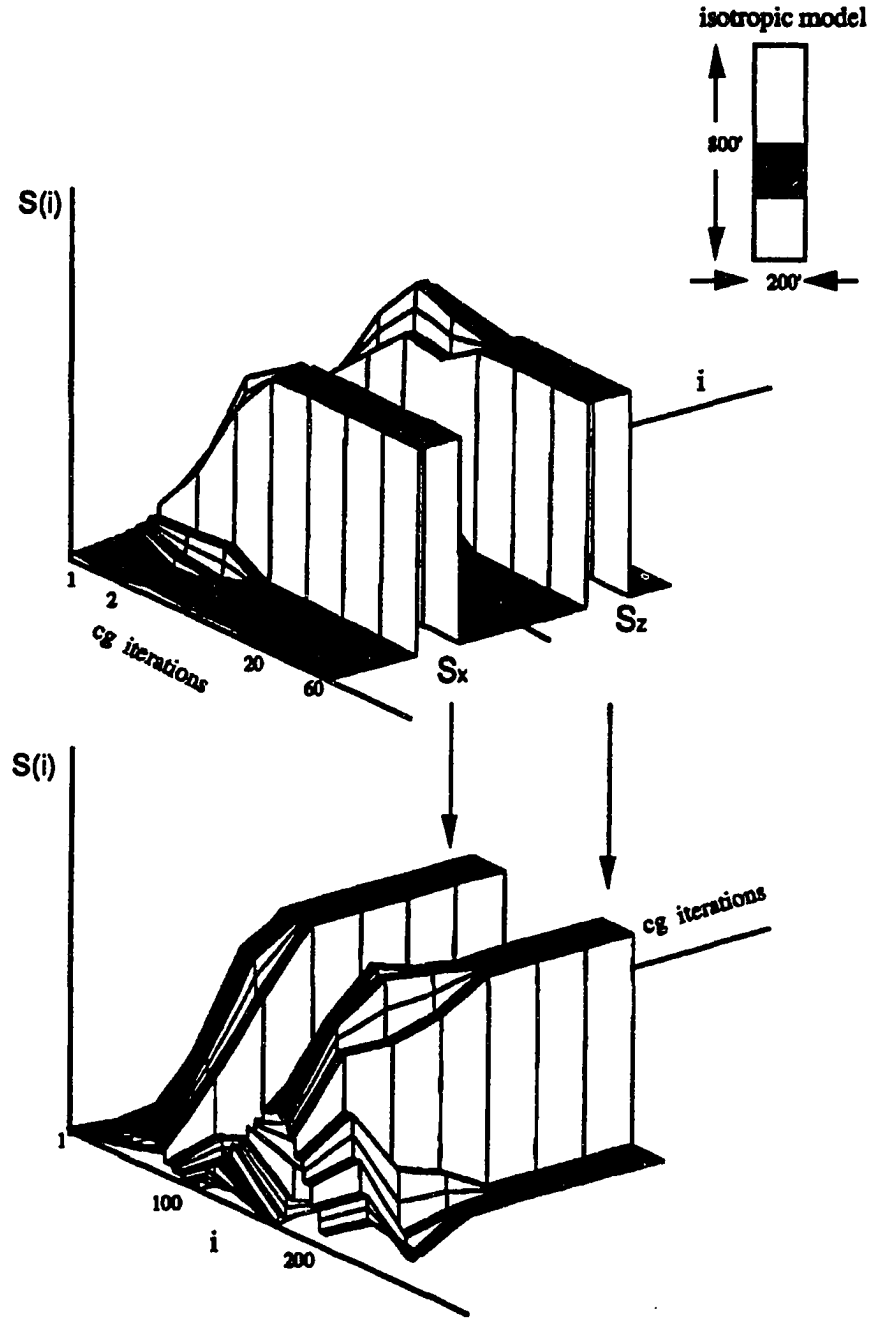

Figure 4.8: Variations of the slowness vector as a function of the number of conjugate gradient iterations. The only difference between the model shown at the top and the model of Figure 4.7 is in the horizontal dimension. The axes "i" and "cg iterations" have been interchanged from one plot to the other.

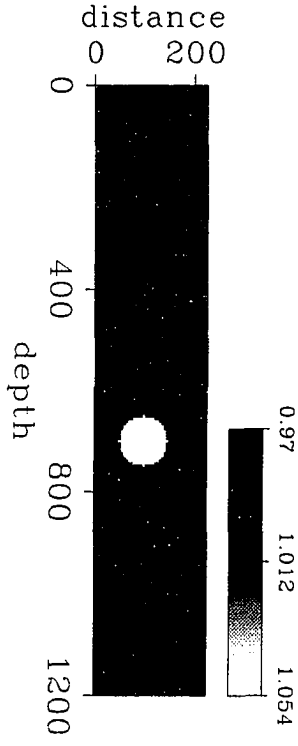

Figure 4.9: 2-D isotropic slowness model. The radius of the circular anomaly is $r = 50$ and is centered at $(100, 700)$. The background slowness is 1.0, and the slowness of the disc is 1.05.

the inversion has to estimate $241 \times 46 \times 2$ parameters from 2200 synthetic traveltimes. Figure 4.10 shows the results of the inversion. The slowness of the isotropic circular anomaly is better estimated by the horizontal than by the vertical component of the slowness in the anisotropic model This is not the case in the 1-D inversion, where both slowness components can be perfectly recovered even though the vertical component of the slowness is not properly sampled. The extra information introduced in that problem by assuming that the model is layered compensates for the limitations produced by the limited view of the measurements. In the 2-D inversion, where the unknowns are less constrained, the better sampling of the horizontal component results in its better recovery when compared with the vertical component and, as a consequence, artificial anisotropy is introduced by the reconstruction. In this noise-free example such anisotropy is not greater than three percent, as the ratio $\frac{S_x}{S_z}$ in Figure 4.10 shows. Doing more CG-iterations does not help to reduce this artificial anisotropy to zero, as in the 1-D inversion (Figures 4.7

and 4.8). This is because S_z contains more information than S_x in the null space, as I show in appendix A. In the present case the images did not change after 120 CG iterations.

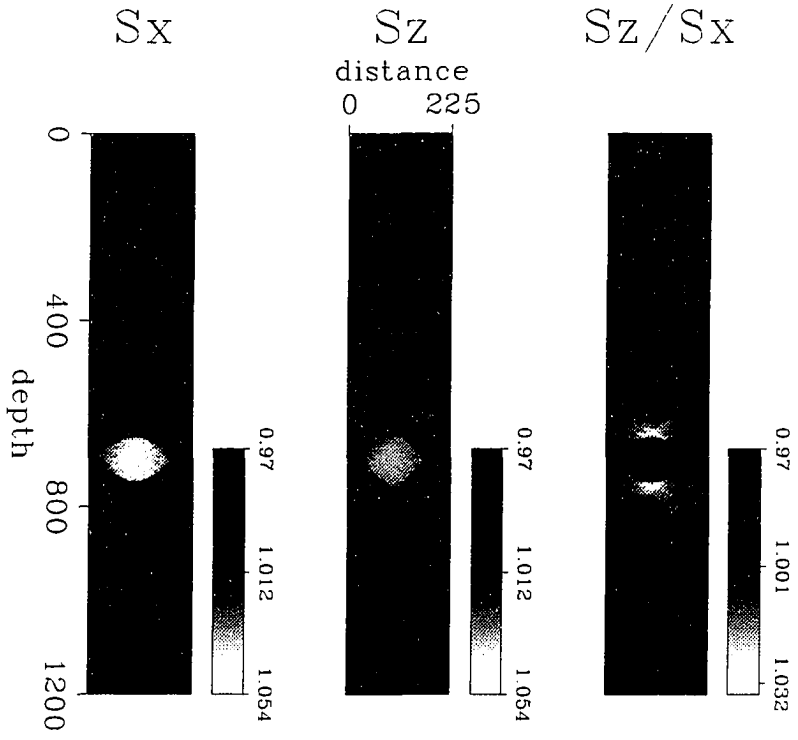

Figure 4.10: Reconstructed horizontal and vertical component of the slowness. The ratio of the two components at the right shows the artificial anisotropy introduced by the reconstruction. Ideally, in this isotropic model, the ratio of slownesses should be unity everywhere.

This example shows that when the velocity contrasts are small, the anisotropy introduced by the inversion can be of the same order as the expected heterogeneities. The artifacts in both slowness components are similar to the well-known truncation artifacts in isotropic inversion, although they are different from one component to the other. Rays that travel horizontally do not influence significantly the estimation of S_z as they do the estimation of S_x. Therefore, the estimated S_x is smeared along the horizontal direction whereas S_z is not. When data from only one geometry are used, the different character of the artifacts for each slowness component can limit our ability to recover variations in actual anisotropy at the same resolution of variations in velocity. This difficulty is apparent in the application to field data later in this chapter.

Since the inversion algorithm introduces anisotropy in the results when the model is fully 2-D, it may be difficult to separate small variations in anisotropy from reconstruction artifacts. If the anisotropy is too weak, it may fall below the level of noise of the reconstruction artifacts and be unable to be reliably estimated. Therefore, when the heterogeneities are described as a superposition of orthogonal square pixels, algorithms based on the weak anisotropy assumption (Stewart, 1988; Chapman and Pratt, 1992; Lines, 1992; Williamson et al., 1993) will produce reliable estimates of anisotropy only if the actual anisotropy is not too weak.

4.4.3 1.5-D inversion

In this example, 4992 traveltimes were generated through the model shown in Figure 4.11 for a geometry where sources were located within ± 45 degrees with respect to the horizontal at each receiver position. I used the anisotropic ray tracing algorithm described in chapter 3 to compute the synthetic traveltimes and to trace the rays needed in the nonlinear inversion. The starting model used for the inversion was homogeneous isotropic described by 17 horizontal layers of equal thickness. The inclination used for the axis of symmetry was $\gamma = 0$ in all layers. Figure 4.12 shows the initial positions of the boundaries in the starting model. By starting the iterations with this model, I wanted to test how the interfaces arranged themselves to create a dipping layer not present in the initial model.

The inversion was constrained by not allowing parallel layers (within ± 5 degrees) to be thinner than 15 feet. No smoothing was applied to the model after each iteration.

Figure 4.13 shows the result of the inversion after tracing rays 35 times, with few conjugate gradient iterations between each ray tracing. The boundaries have moved with respect to their initial positions, and the initial 17 layers have been reduced to 10 to allow the positioning of the dipping layers at the correct depths with the correct dips. The inclinations of the axes of symmetry estimated by the algorithm are also correct. Figure 4.14 compares profiles at $x = 0$ of the real model (Figure 4.11) and the estimated one (Figure 4.13). The agreement is almost perfect.

In this example it was possible to estimate correctly both small and moderate dips (between 0 and 30 degrees), but the answer to the question about the maximum and minimum dips that can be retrieved from the data depends in general on the aperture of the recording geometry, the interval between sources and receivers, and the frequency of the data.

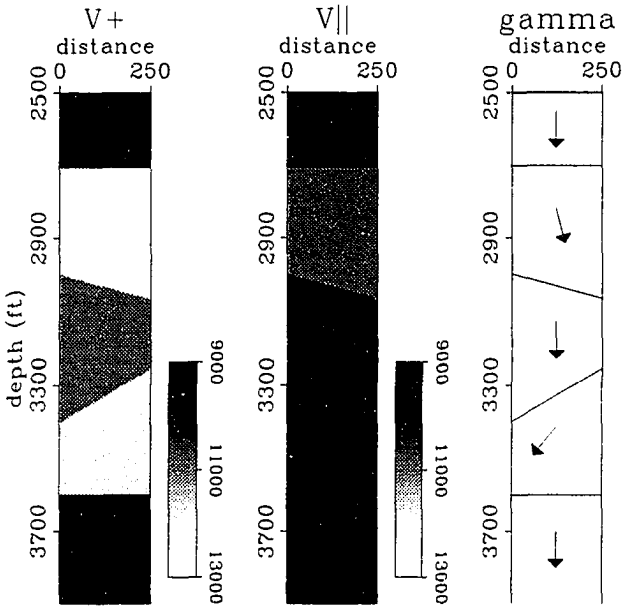

Figure 4.11: 1.5-D model used to test the inversion. The third interface dips 15 degrees and the fourth one -30. The inclination of the axis of symmetry in the second layer is -15 degrees and 40 degrees in the fourth layer. The ratio $\frac{V_\perp}{V_{||}}$ at the fourth layer is 1.26. The gray scale shows variations in velocity. "$V+$" stands for $V_\perp$, "$V||$" for $V_{||}$, and "gamma" for γ.

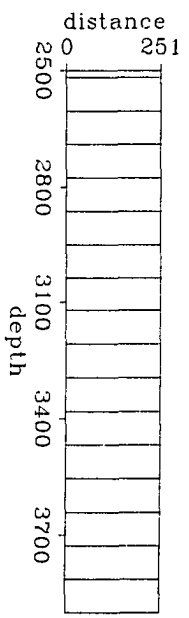

Figure 4.12: Initial position of the interfaces in the starting model (homogeneous isotropic). The velocity is equal to 12 000 ft/sec, and the inclination of the axes of symmetry with respect to the vertical is zero for all layers.

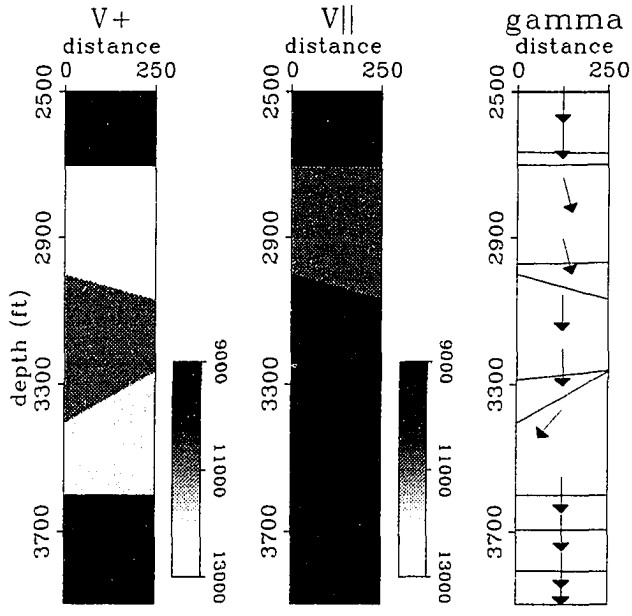

Figure 4.13: 1.5-D anisotropic inversion. Notice how the interfaces have changed their initial positions. The position of each arrow's head shows the interval that corresponds to each γ. The gray scale shows variations in velocity.

4.5 Field data examples

Anisotropic traveltime tomography was also performed with cross-well P-wave traveltimes recorded at an Amoco Gulf Coast site and BP's Devine test site.

At these two sites, the wells are not confined to a single plane. Instead, they deviate gradually from the vertical plane that contains them at the near surface. I have taken this effect into account by following this two-step procedure:

1. Find the true 3-D distances between sources and receivers.

2. Assume that one well is vertical (for example, the source well) and locate the receivers at the corresponding true relative distances and true depths in the other well, which is equivalent to locating the origin of the coordinates to measure the distances at the source well.

When correcting for the well deviation in this way, actual source-receiver separations are used in the inversion.

To measure the closeness between measured and calculated traveltimes, I use the mean

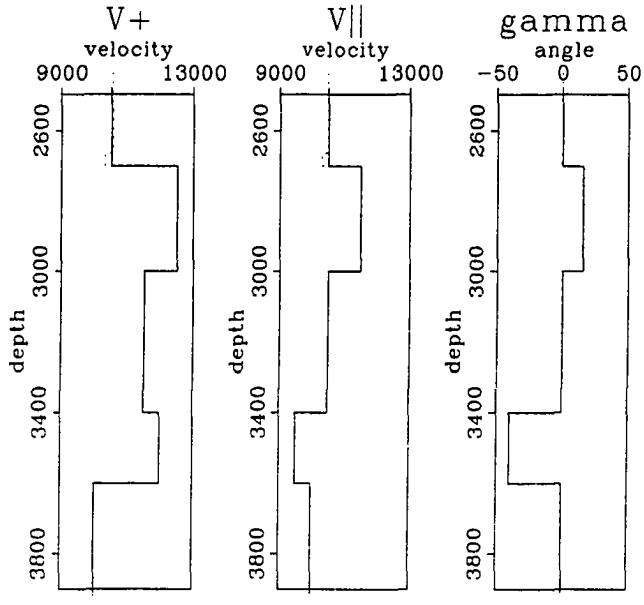

Figure 4.14: Profile at $x = 0$ of the real model and the estimated one (Figures 4.11 and 4.13, respectively). The continuous line represents the real model; the dashed one represents the result of the inversion. The agreement between real and estimated parameters is almost perfect.

absolute value of the residuals

$$error = \frac{1}{M}\sum_{i=1}^{M}|t_{c_i} - t_{r_i}|, \tag{4.12}$$

where t_{r_i} and t_{c_i} are the measured and calculated traveltimes, respectively, and M is the total number of traveltimes.

When the real velocities are elliptical, the direct velocity along one axis and the normal moveout (NMO) velocity around the perpendicular axis are equal. For this reason, no distinction was made between direct and NMO velocities in the synthetic examples of the previous section. In field data applications, however, such a distinction needs to be made because in general the rocks are not elliptically anisotropic. Therefore, after doing anisotropic traveltime tomography with a given data set, we must label the velocities appropriately (either direct or NMO) before procceding to estimate the elastic constants of the medium as explained in chapter 2. Moreover, even if the mapping to elastic constants is not possible because the data set is incomplete, we should still label the velocities correctly before interpreting the results.

4.5.1 Gulf Coast site

Cross-well data were acquired jointly by Amoco Production Company and Stanford University at an on-shore Gulf Coast site in Southeast Texas. The overall survey geometry is illustrated in Figure 4.15. This geometry is similar to the one used in the synthetic example of 2-D inversion. The source, a piezoelectric bender bar, produced a sweep signal with frequencies between 400 Hz and 1600 Hz. The data were recorded with a sample interval of 0.1 msec. More details about the site and geometry are found in Harris et al. (1990).

Nearly 5000 *P*-wave first arrival times were picked from the correlated data. In general, I found that the traveltimes corresponding to the near horizontal rays (or near vertical offsets) were more difficult to pick than those at far offsets.

Because the shots are within ±50 degrees with respect to the horizontal at each receiver location, we can expect most of the data to be modeled appropriately using elliptical anisotropy, as I show in chapter 2 by fitting a *P*-wave impulse response with ellipses estimated from data at different apertures, up to 40 degrees.

The relative position of the two wells, taking into account the deviation, is shown in Figure 4.16. To use the true relative distances, it is necessary to move the receiver positions horizontally in the deviated well. For this reason, the receiver positions in Figure 4.16 look slightly smeared in the horizontal direction. The selection of the vertical well used as a reference to measure the relative deviations is irrelevant if we assume that the model is 1-D. In two dimensions different distorsions may occur depending on which well is chosen as a reference and how strong the actual 2-D variations are.

1-D inversion

The simplest inversion that we can possibly do assumes a homogeneous isotropic model. The result is the mean velocity [equation (4.7)], V_{iso} = 8452 ft/sec. The next step is to assume that the model is still homogeneous but elliptically anisotropic. Using equation (4.8) I found that V_x = 8586 ft/sec and $V_{z\mathrm{NMO}}$ = 8079 ft/sec.[2] For this particular recording geometry (Figure 4.15), V_{iso} is closer to V_x than to $V_{z\mathrm{NMO}}$, which means that the "averaging" of the horizontal and vertical directions that the isotropic inversion implicitly

[2]Since only *P*-waves are used in the field data examples of this chapter, I have omitted the "*P*" when talking about $V_{P,x}$ and $V_{P,z\mathrm{NMO}}$.

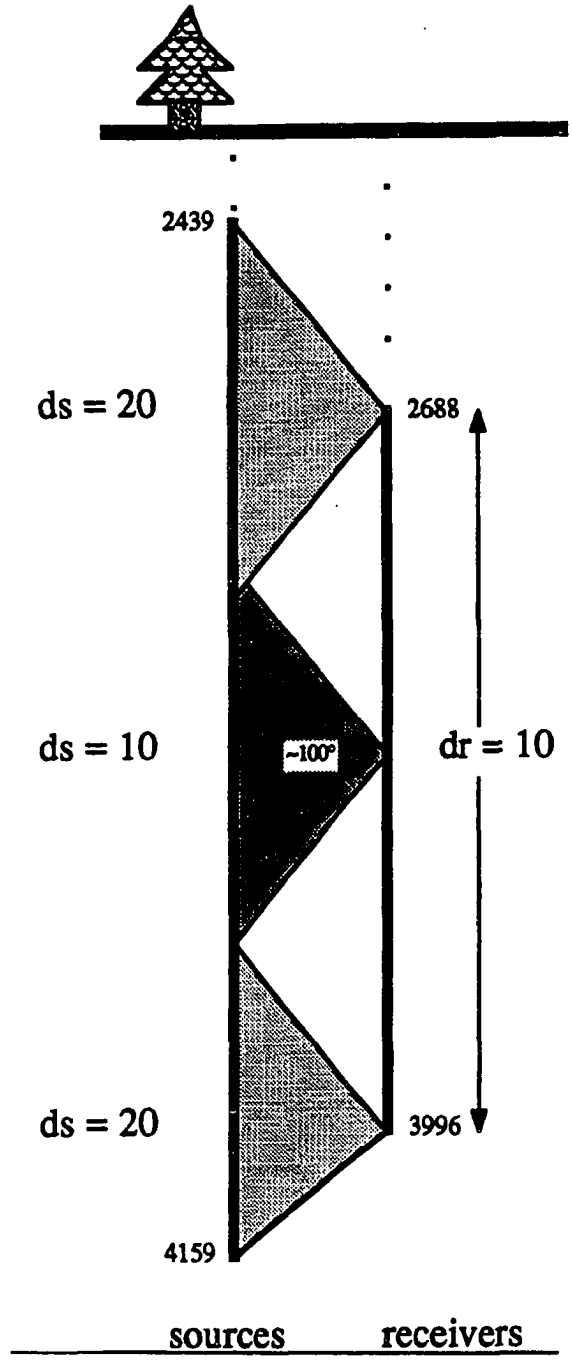

Figure 4.15: Overall survey geometry illustrating the shooting pattern. Receivers are spaced at $dr = 10$ feet between 2688 and 3996 feet. Sources are spaced at $ds = 10$ feet intervals in the primary target zone, and $ds = 20$ feet above and below the target zone. The average separation between wells is 225 feet.

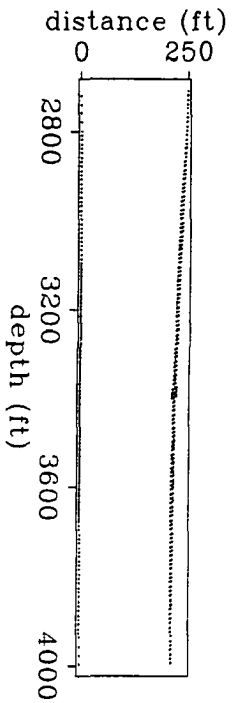

Figure 4.16: Positions of the source and receiver wells plotted after considering their relative deviations. Each dot represents a source or a receiver position (left and right respectively). The density of sources is larger at the middle of the surveyed area than at the extremes.

does is not a simple arithmetic average. As I show later, the same conclusion can be drawn when the model is heterogeneous.

The mean absolute value of the residual [equation (4.12)] for the homogeneous isotropic model is 1.04 ms. When the model is homogeneous anisotropic, *error* = 0.94 ms.

Figure 4.17 shows the result of the isotropic inversion when the model is one dimensional. The traveltimes used correspond to rays below 2705 feet and above 4000 feet. This depth interval was discretized in 60 horizontal layers of equal thickness (21.583 feet). Straight rays were used to compute synthetic traveltimes since, according to Harris et al. (1990), small velocity variations are expected in this site. The 2-D isotropic, straight-ray tomogram shown in a later subsection is similar to the 2-D isotropic, curved-ray tomogram obtained by Harris et al. (1990). I did conjugate gradient iterations (40) until no appreciable changes were seen either in the model or in the error (4.12), which is equivalent to reaching the flat part of the hills in Figure 4.7. For the model shown in Figure 4.17, *error* = 0.67 ms.

Then, I allowed the 1-D model to be anisotropic. Figure 4.18 shows the result of the

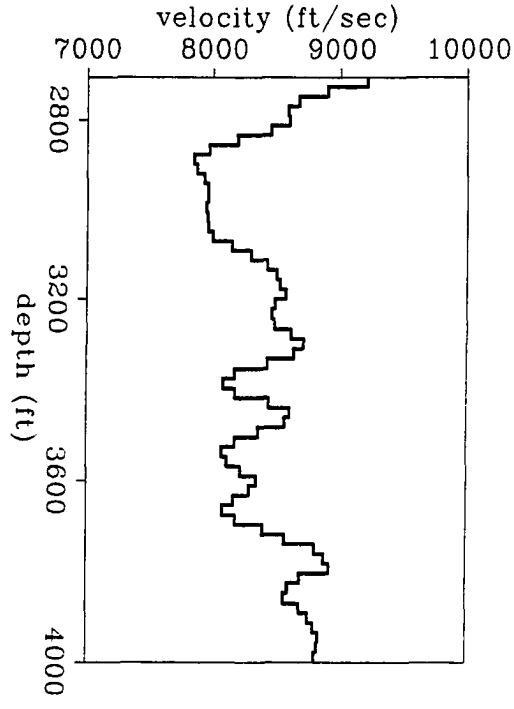

Figure 4.17: 1-D isotropic inversion. The thickness of each layer is 21.583 feet.

inversion. For traveltimes computed through this model, *error* = 0.59 ms. The thick curve represents the horizontal velocity, and the thin one represents the vertical NMO velocity. The first thing one notice is that V_x is generally larger than $V_{z\mathrm{NMO}}$. Figure 4.19 compares V_x and $V_{z\mathrm{NMO}}$ with V_{iso}. In general, V_{iso} is closer to V_x than it is to $V_{z\mathrm{NMO}}$, which is consistent with the previous results of the inversion assuming a homogeneous medium. This means that for the type of recording geometry used (ray angles between 0 and ±50 degrees) the isotropic inversion is affected primarily by the horizontal component of the velocity. Since there are fewer rays at large angles, the isotropic inversion is less constrained by them.

At this site, sonic logs were available at both wells (Figure 4.20). Sonic logs sample the vertical component of velocity a few inches away from the well, at frequencies ($\sim$ 10 kHz) much larger than the typical frequency of the cross-well data ($\sim$ 1 kHz). To compare the information obtained from these two types of measurements (1-D tomogram and velocity logs), I did some averaging to the logs. First, I averaged each slowness log in blocks of thickness equal to the layer thickness in the 1-D tomographic inversion. I then averaged

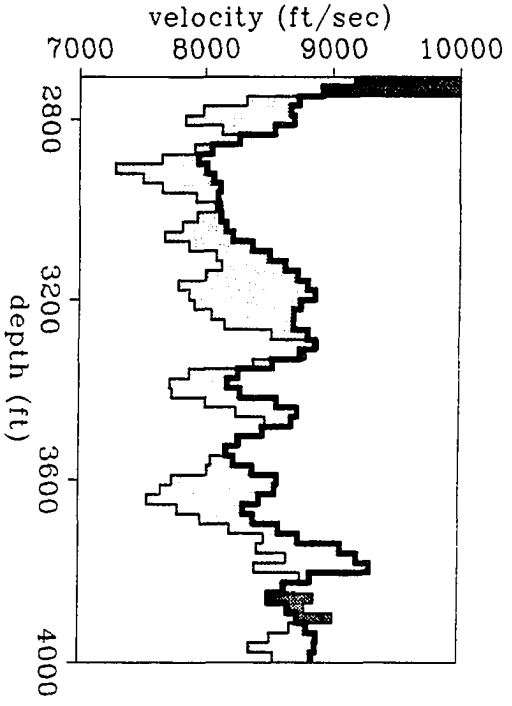

Figure 4.18: 1-D anisotropic inversion. The thickness of each layer is 21.583 feet. The differences between V_x (thick line) and $V_{z\mathrm{NMO}}$ (thin line) are represented by two colors: light gray when $V_x > V_{z\mathrm{NMO}}$, and dark gray when $V_x < V_{z\mathrm{NMO}}$.

the two averaged slowness logs into a single one. The purpose of the last averaging was to produce a single curve to compare with the $V_{z\mathrm{NMO}}$ estimated by the inversion algorithm. Figure 4.21 compares the average velocity log with V_{iso}, V_x, and $V_{z\mathrm{NMO}}$. When compared with V_{iso} and V_x, $V_{z\mathrm{NMO}}$ is not only much closer to the average sonic velocity but also better correlated with it. Figure 4.21 shows that assuming an elliptical model for the velocities is an improvement over assuming a circular, that is, isotropic one.

The comparison between the average sonic velocity and $V_{z\mathrm{NMO}}$ has to be interpreted carefully, because each curve averages the medium velocities in a different way where the medium changes laterally. On the one hand, the average log assumes that at each depth the medium has only two velocities that contribute with equal weight to the estimate (mean). On the other hand, the way the inversion averages the lateral changes in the medium properties when computing $V_{z\mathrm{NMO}}$ is not clear at this point. It is also not clear at this point how the potential errors of inverting for 1-D variations in a 2-D medium propagate into the solution. Some parts of the real medium show lateral variations, which becomes evident when performing the 2-D inversion.

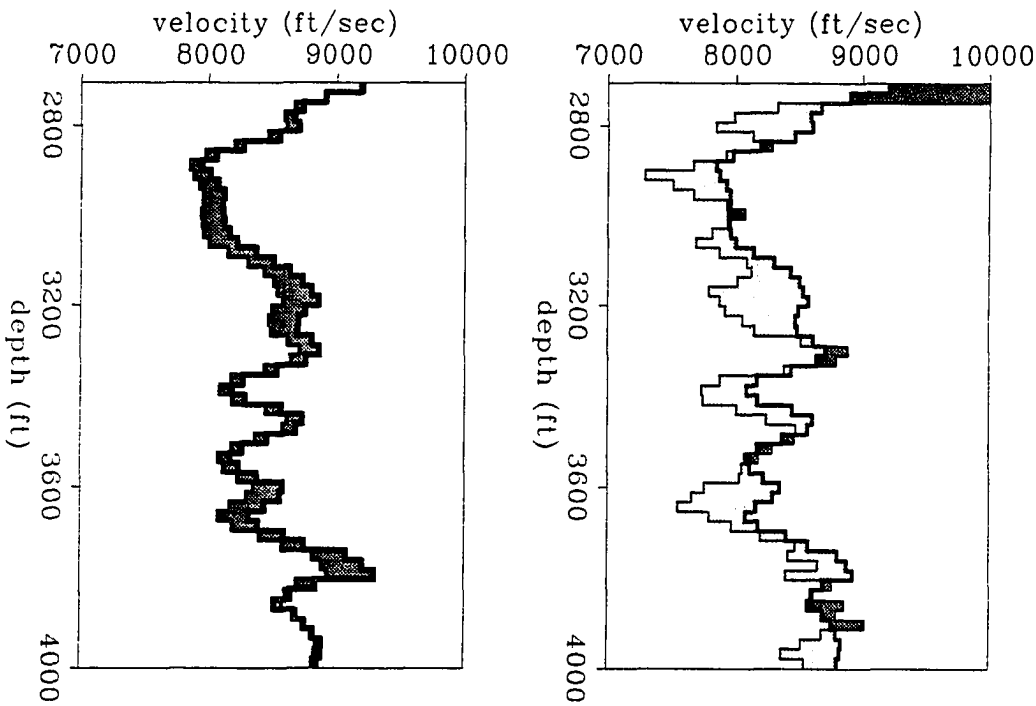

Figure 4.19: Comparison between isotropic and anisotropic layered inversion. Left: V_{iso} (thin line) and and V_x (thick line). Right: V_{iso} (thick line) and $V_{z\mathrm{NMO}}$ (thin line). The differences between the isotropic and anisotropic inversion are represented by two colors: light gray when $V_{iso} > V_x$ or $V_{z\mathrm{NMO}}$, and dark gray when $V_{iso} < V_x$ or $V_{z\mathrm{NMO}}$.

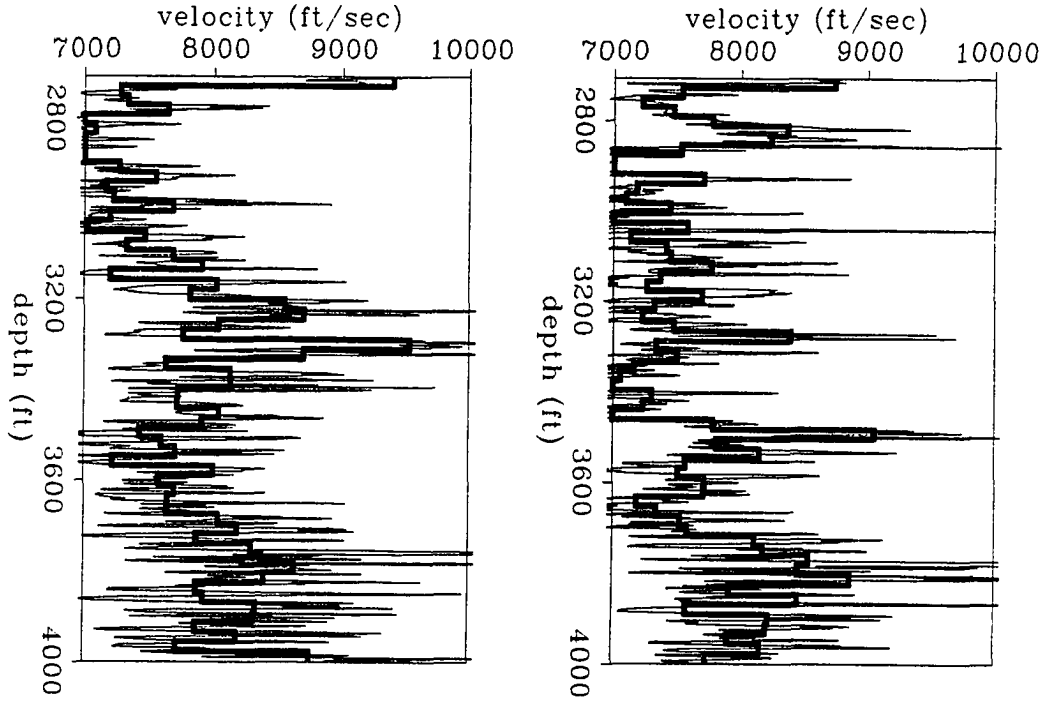

Figure 4.20: Sonic logs at the source well (left) and receiver well (right). The thin line represents the original log. The thick line represents the corresponding log averaged in 60 layers of equal thickness (21.583 feet).

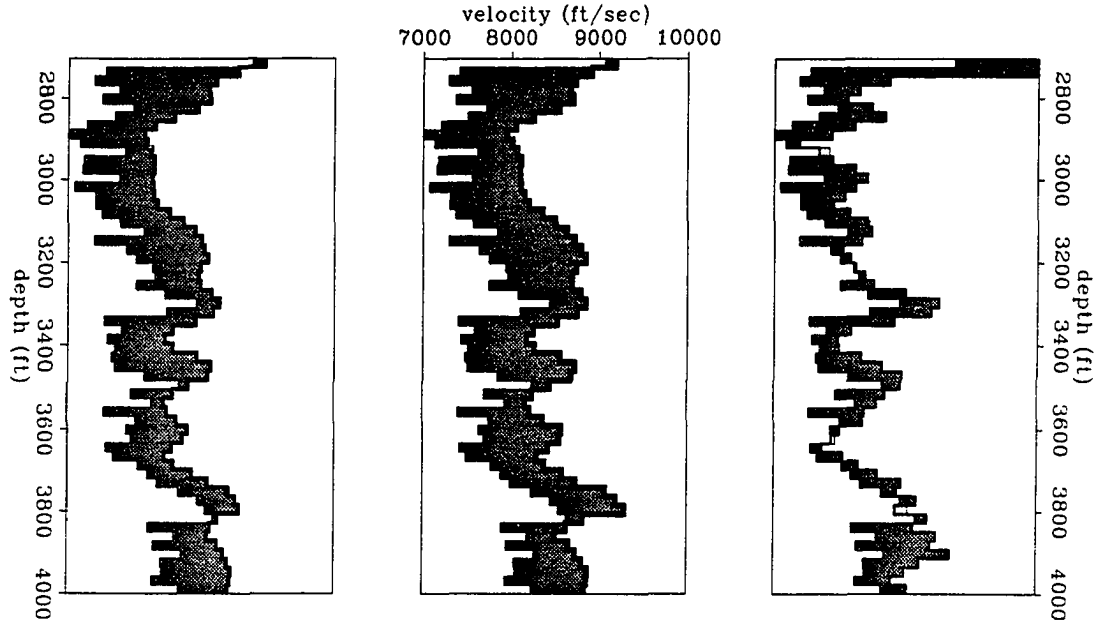

Figure 4.21: Average velocity log (V_z) compared with V_{iso} (left), V_x (center), and $V_{z\text{NMO}}$ (right). $V_{z\text{NMO}}$ is closer and better correlated with the velocity log.

Figure 4.21 also shows that $V_{z\text{NMO}}$ is systematically larger than the log velocity V_z, which is just the opposite of what I expected from (2.34), if the anisotropy is assumed to be caused by fine layering. In a later section, I explain different sources of biases in the inversion that may explain this result.

The ratio $V_x/V_{z\text{NMO}}$ is roughly correlated with the lithology, as shown in Figure 4.22. In this figure, the thick line corresponds to the ratio $V_x/V_{z\text{NMO}}$, and the thin one corresponds to the average spontaneous potential (SP) log. The average SP log was obtained by blocking each log separately, taking the average of the results, and removing a linear trend with depth in the final average. There is a good correlation between large SP values (that indicate the presence of shales) and large anisotropy ratio. The same happens for low SP values (sands) and isotropic layers. When interpreting these results, however, we must keep in mind that each curve represent a different type of average of the lateral changes in medium properties.

In the anisotropic inversion of this data set, in order to reach a good compromise between resolution and stability, I used 60 layers of 21.583 feet each. Reducing the layer thickness by half has the effect (not shown) of increasing the resolution at the expense of

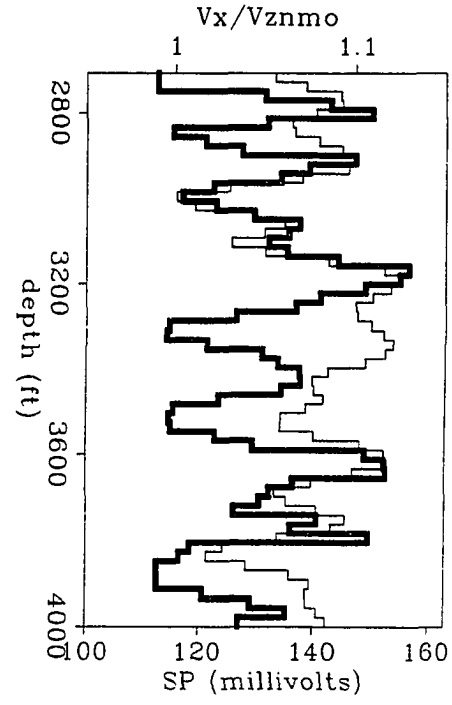

Figure 4.22: Anisotropy ratio $V_x/V_{z\text{NMO}}$ (thick line) compared with the SP log (thin line).

large variations and instabilities in the vertical component of the velocity that is not well sampled by the recording geometry. The horizontal component of velocity is generally more stable than the vertical for smaller layer thicknesses. Obviously, at the expense of resolution, increasing the layer thickness made the inversion more stable.

2-D inversion

When the relationship between the data and the unknown is linear, we should obtain the model that best fit the data in only one solution of the ray tracing problem. When the problem is nonlinear one approach is to solve it as a sequence of linearized steps. We usually call these steps *external* iterations, to differentiate them from the *internal* iterations needed to solve each linear problem when using iterative techniques such as conjugate gradients. Ideally, if the problem has n unknowns, each external iteration should consist of m CG-steps (m internal iterations), where $m \leq n$ is the number of different singular values. When dealing with field data, however, we might not be able to take that many steps because of the presence of the noise. Noise can affect the solution of

each linearized problem in the following ways: (a) it might be amplified into the model by the smallest singular values recovered when m iterations are performed, and (b) it might considerably affect the accuracy of the search directions and, consequently, the position of the minimum associated with the solution. Therefore, we have to deal carefully with the noise.

Under the straight-ray assumption, only one external iteration was needed in the 1-D inversion to find the model shown in Figure 4.18. By selecting the layer thickness appropriately, I was able to do the CG-iterations required to reach convergency without being much affected by the noise. Thicker layers damped the solution, whereas thiner layers introduced instabilities. In two dimensions, however, the situation is different. I found here that the results were more sensitive to noise in the data than the 1-D solutions. This is not surprising because in two dimensions, as explained in appendix A, we are trying to estimate high-frequency variations in $S_{z\mathrm{NMO}}$, which are related to the smallest singular values of the problem that amplify the noise.

Because of the sensitiveness to the noise of the 2-D inversion, it is necessary to avoid doing "many" CG-iterations at each linearized step. After doing several tests that combined in different ways external and internal iterations with mean-average smoothing of the slowness model, I adopted a conservative approach to minimize the error (4.12). The approach consisted of the following steps:

1. Compute traveltimes in the given model, calculate the matrix $\underset{\sim}{\mathbf{J}}$, and find the residuals.

2. Approximate the solution of the linear problem (4.11) by applying a few (typically one or two) CG-iterations. Limiting the number of CG-iterations is, for practical purposes, equivalent to damping (Scales and Gersztenkorn, 1988).

3. Smooth the updated slowness model.

4. Repeat the preceding steps until there is no reduction in the sum (4.12). When this happens, either stop the process or increase the number of CG-iterations by one and check whether further reductions in the residuals are obtained.

When the problem is linear, the solution is not obtained in only one iteration because of the presence of the noise.

When the previous procedure was applied to estimate an isotropic model from the data, I obtained the image shown in Figure 4.23 (*error* = 0.54 ms). In this case, the unknown model was discretized into 131 × 26 square cells (10 × 10 ft^2 each). It is interesting to note that adding more degrees of freedom to describe the heterogeneity (i.e., more cells) does not substantially improve the parameter *error* obtained with 28 times fewer degrees of freedom in the 1-D anisotropic inversion. The model shown in Figure 4.23 is similar to the one obtained by Harris et al. (1990), where ray bending has been taken into account.

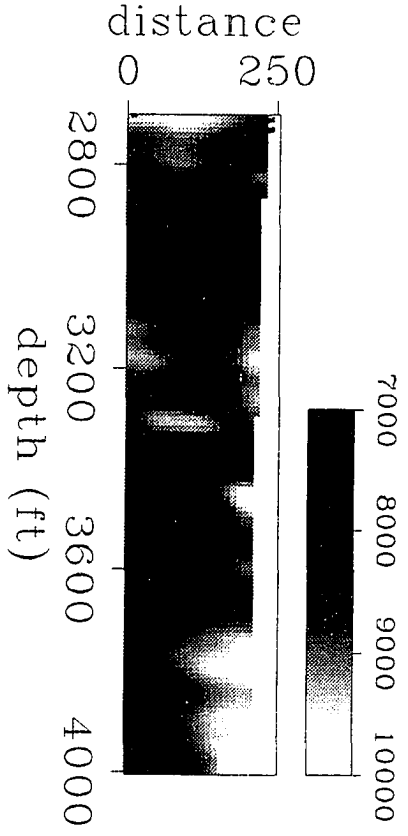

Figure 4.23: 2-D isotropic inversion. The image has been divided into 131 × 26 square cells (10 × 10 ft^2 each).

The result of the 2-D anisotropic inversion is shown in Figure 4.24 (*error* = 0.45 ms). As in the 1-D example, that V_x is remarkably similar to V_{iso}. The main difference between these two images is that in V_x (Figure 4.24) the events tend to be more horizontally smeared than in V_{iso} (Figure 4.23). This result was predicted from the 2-D synthetic

example shown in Figure 4.10.

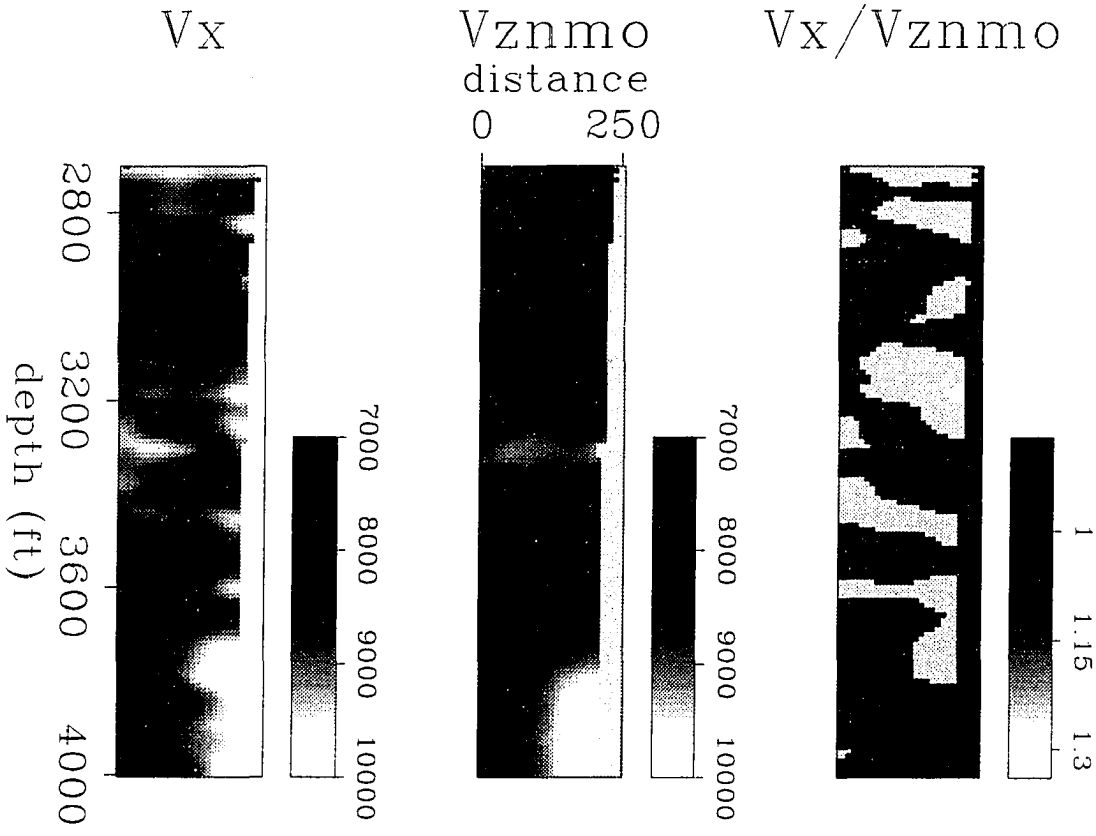

Figure 4.24: 2-D anisotropic inversion. Each image has been divided into 131 × 26 square cells (10×10 ft^2 each). Left: V_x. Center: $V_{z\mathrm{NMO}}$. Right: $V_x/V_{z\mathrm{NMO}}$. The spatial resolution of $V_{z\mathrm{NMO}}$ is poor when compared with the spatial resolution of V_x. The ratio $V_x/V_{z\mathrm{NMO}}$ has been separated into four areas that show percentages of anisotropy: white (ratio $>$ 1.25), light gray ($1.06 <$ ratio ≤ 1.25), dark gray ($0.90 <$ ratio ≤ 1.06), and black (ratio ≤ 0.9). The dark gray areas can be considered isotropic.

Since V_z is not adequately sampled by the recording geometry, the events in the estimated vertical component of the velocity tend to be smeared in the direction of the steepest rays, and the spatial resolution in this component is poor when compared with V_{iso} and V_x. In the 1-D case, this lack of information is compensated for by assuming a layered model, which allows us to do more CG-iterations without having problems with the noise. In two dimensions, however, doing more CG-iterations is not possible and therefore the results obtained can be in a stage where V_x is close to convergency but $V_{z\mathrm{NMO}}$ is far from that point. This difference in the speed to convergency of the different components

of the velocity may introduce artificial anisotropy.

Because V_x and $V_{z\text{NMO}}$ cannot be estimated at the same resolution (at least using only this type of recording geometry), it is not possible to estimate spatial variations in velocity anisotropy (the ratio $V_x/V_{z\text{NMO}}$ for example) at the same resolution of the variations in velocity. Nevertheless, an image that shows variations in velocity anisotropy can be useful if it accounts only for the large-scale variations that are well resolved by the inversion. Such an image is shown in Figure 4.24. This image is divided into four areas: highly anisotropic, moderately anisotropic, isotropic, and anisotropic with $V_{z\text{NMO}} > V_x$. We can see that most of the model is isotropic whereas the anisotropic areas are associated with high-velocity zones, possibly shales.

Figure 4.25 summarizes how the mean absolute value of the residual (*error*) changes for the different parametrizations used. The error decreases roughly 50 percent from the homogeneous to the 1-D inversion and about 60 percent from the homogeneous to the 2-D inversion, which means that when trying to estimate lateral variations in the medium (smallest singular values), a 10 percent reduction in the mismatch is gained with respect to the estimation of vertical variations only (largest singular values). The residual does not reduce substantially when we compare the 1-D anisotropic inversion (letter D in the plot) with the 2-D isotropic (letter E), with 28 more degrees of freedom, which suggests that anisotropy in the data can be reconciled with either isotropic heterogeneity or anisotropic, less heterogeneous media.

4.5.2 Devine test site

BP's Devine test site is located southwest of San Antonio, Texas. A sketch of the geology at this site is shown in Figure 4.26. This test site has been cited in recent publications to illustrate the application of different techniques. For example, Harris (1988) reports cross-well seismic measurements using a cylindrical piezoelectric bender transducer both as a source and as a receiver. Miller and Chapman (1991) and Onishi and Harris (1991) have concentrated on the problem of estimating velocity anisotropy from cross-well data (tomographically and by head-wave analysis, respectively). Lazaratos et al. (1991) present reflection images also from the cross-well data, and Raikes (1991) has studied the propagation of S-waves from a multicomponent VSP survey.

The cross-well data I used were P-waves with frequencies between 200 Hz and 4000 Hz. They were recorded between two cased boreholes (Wilson 2 and Wilson 4) whose

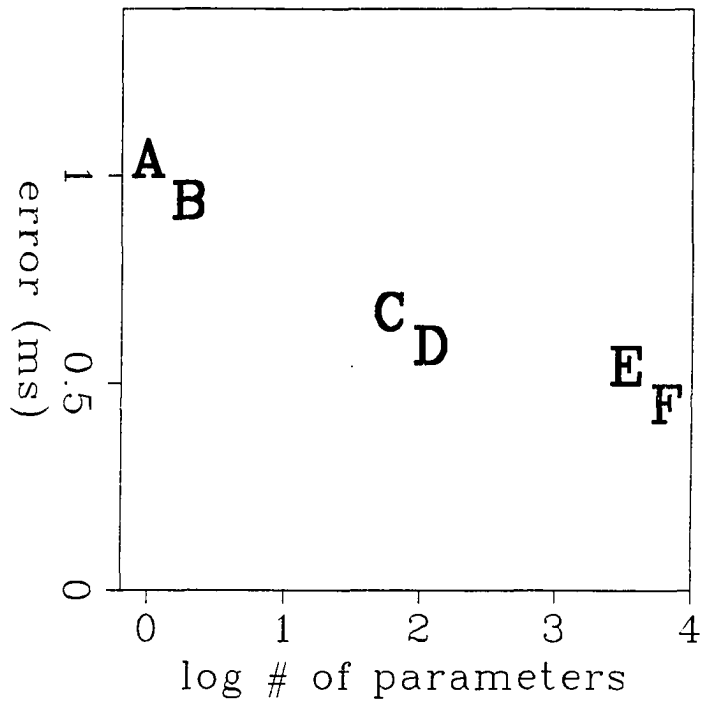

Figure 4.25: Mean absolute residual for the different parametrizations used. (A): Homogeneous isotropic. (B): Homogeneous anisotropic. (C): 1-D isotropic. (D): 1-D anisotropic. (E): 2-D isotropic. (F): 2-D anisotropic.

separation at the surface is 330 feet. Receivers were separated by 10 feet and sources by 20 feet. Figure 4.26 shows the corresponding sonic logs at each well. Although the variations are mainly one dimensional, it is possible to identify small dips ($\approx$ 1 degree) from the sonic logs at the two wells as well as small lateral variations within thin layers (for example, the top of the Del Rio clay).

A total 1660 traveltimes were picked from a small data set of only 26 gathers. Only those traveltimes corresponding to angles of less than 45 degrees between source and receiver were kept for the inversion.

Figure 4.27 shows the positions of sources and receivers for 10 percent of the data set. The ray coverage is quite irregular, with no horizontal rays sampling large portions of the medium. The horizontal velocities estimated in areas not sampled by horizontal rays are the horizontal velocities of the best fitting ellipses.

A 1.5-D elliptically anisotropic model was used to fit the data. The starting model (not shown) consisted of 140 horizontal layers five feet thick. The velocity for all layers

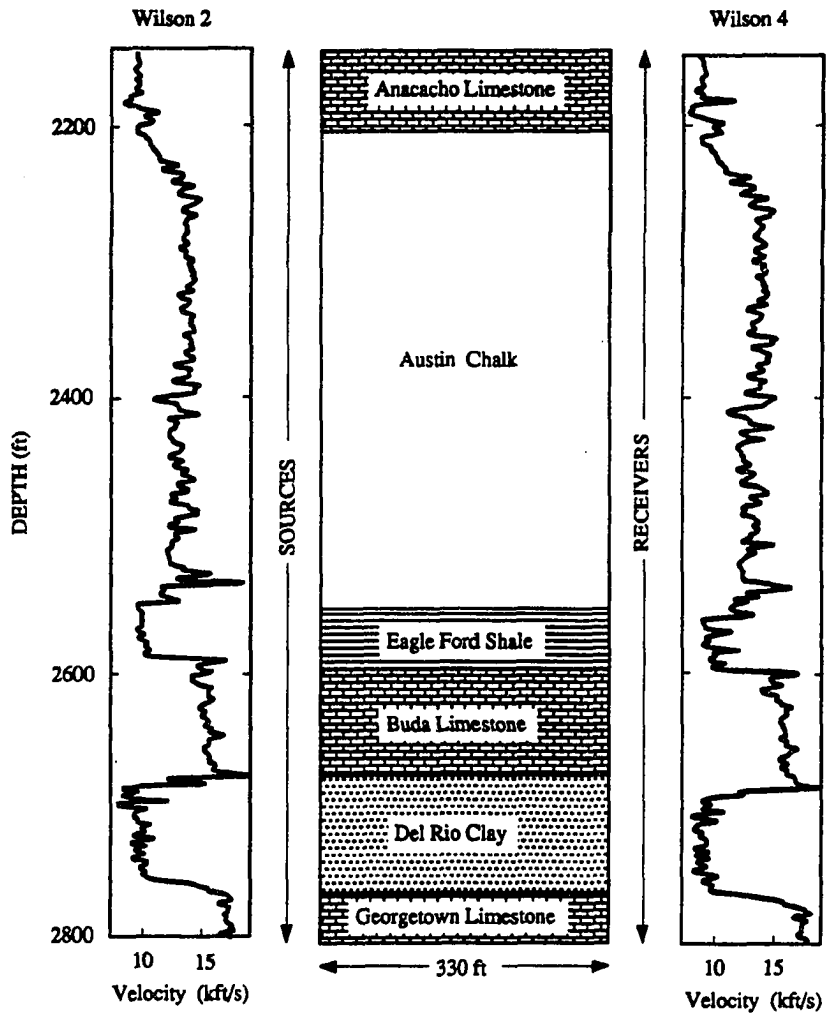

Figure 4.26: Sketch of the geology at the Devine test site with the sonic logs at each well. Although the site is mostly flat layered, small 2-D variations can be seen (modified from Lazaratos et al., 1991).

was 12 000 ft/sec. Layers thinner than one foot were not allowed in the model. The inversion was not constrained to match the vertical velocities or depth of certain layers using information derived from the sonic logs, although the information about dips was already present in the initial model. The dips and the intercepts of the interfaces, as well as the axes of symmetry of the different layers, were allowed to vary during the inversion.

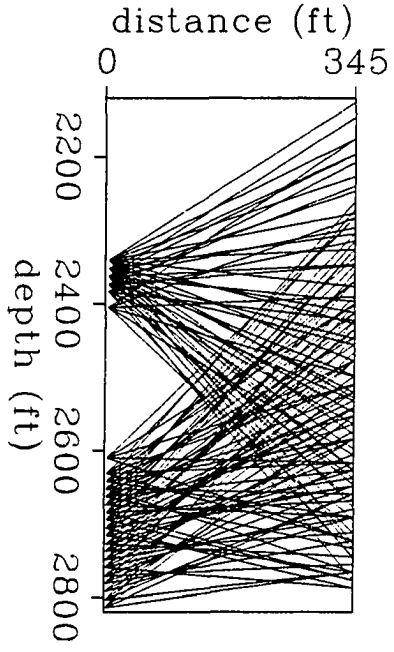

Figure 4.27: Ray coverage for the experiment at the Devine test site for a fraction (10 percent) of the total data set. Notice how irregular the coverage is.

The inversion produced a model with horizontal layers (all dips less than 0.1 degree) and vertical axes of symmetry. Therefore, $V_\perp = V_x$ and $V_\parallel = V_{z\mathrm{NMO}}$. Figure 4.28 shows V_x and $V_{z\mathrm{NMO}}$ as well as the average sonic log (V_z) from the two wells, blocked every seven feet. As expected when the anisotropy is caused by fine layering, $V_x > V_z > V_{z\mathrm{NMO}}$ for almost all depths. We also see that $V_{z\mathrm{NMO}}$ is much closer to the sonic log than V_x. In the shale and clay intervals, V_x is more than 30 percent larger than the log velocity The vertical velocity contrast between limestone and shale is greater than 70 percent. Still, the inversion does a good job in estimating $V_{z\mathrm{NMO}}$, which shows the importance of tracing rays appropriately in anisotropic media when doing the inversion. For this model, the average absolute value of the residuals is 0.2 ms (twice the sampling interval). Twelve

layers were eliminated during the inversion procedure because their thicknesses fell bellow the one foot threshold.

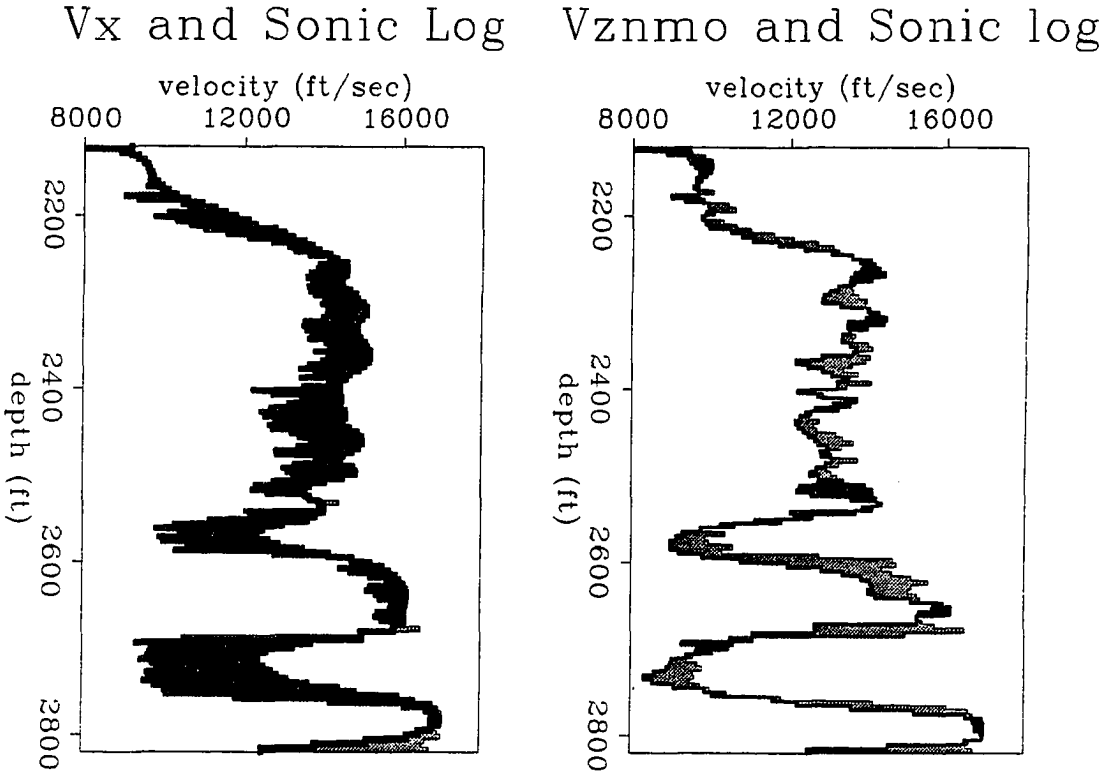

Figure 4.28: 1.5-D inversion at the BP site. An average sonic log (thinner curve) blocked every seven feet is compared with the two estimated velocities. The vertical NMO velocity is closer and better correlated to the log. The amount of anisotropy changes through the model, reaching a peak at the shale and clay intervals. The model is described by 128 layers.

These results agree with those presented by Miller and Chapman (1991) and Onishi and Harris (1991).

Figure 4.28 also shows that the elliptical velocity model explains most of the P-wave anisotropy at this site. The estimated vertical NMO velocity is in general smaller than the log velocity, which is expected if the anisotropy is caused by fine layering. However, the differences between the log velocity and the vertical NMO velocity show that the elliptical model is not fully adequate to describe the possible transverse isotropic nature of this medium. In a few places (the top of the clay, for example) the estimated vertical velocities are larger than the log velocity. This is probably because of lateral variations in the real

medium that are not correctly described by the model of heterogeneities.

Biases in the inversion

The main problem considered in the preceding sections was how the limited view of the measurements affects our ability to estimate velocities in different directions. Unfortunately, many other factors besides limited view produce effects that may depend on direction and influence the anisotropy of the results. Among these factors we have:

1. Picking errors. These errors may systematically increase or decrease the velocities, depending on which part of the first arriving wavelet has been picked. Picking before the correct value speeds velocities up, whereas picking later arrivals slows the velocities down. If the picking errors are constant for different vertical offsets, the velocities that result from the inversion can be anisotropic because the errors have more effect on the smaller traveltimes that usually correspond to rays that travel horizontally. Picking errors may explain why in Figure 4.21 $V_{z\mathrm{NMO}}$ is systematically one or two percent faster than the sonic log.

2. Head waves picked as body waves. Although this bias may be considered a picking error, it primarily affects traveltimes from small vertical offsets (i.e., ray paths close to the horizontal) in low-velocity layers. Traveltimes from head waves picked as body waves affect S_x more than $S_{z\mathrm{NMO}}$ because $S_{z\mathrm{NMO}}$ is less sensitive to rays that travel at small angles. Therefore, when head waves are inverted like body waves, the estimated horizontal velocity may turn out to be faster than the actual one.

3. Well deviation. Often, wells deviate in three dimensions but the results are rarely presented in three dimensions. Instead, the 3-D deviations are usually projected onto a 2-D plane where conventional 2-D algorithms can be applied. If the well deviation is not strong, and if the 3-D variations in the real medium are moderate, the 2-D solution is a good approximation but otherwise it may not be. I didn't consider the well deviation when first testing the algorithm with field data. When comparing the velocities that were estimated without considering well deviation with those estimated by considering it (Figure 4.21), I obtained higher velocities where the wells were actually closer and lower velocities where the wells were actually farther apart. S_x was more sensitive to well deviation than $S_{z\mathrm{NMO}}$.

All these factors, when not considered correctly, may produce artificially anisotropic results, especially when complex models are used to describe both anisotropy and heterogeneity.

4.6 Conclusions

This chapter has presented the basic theory and examples of an algorithm that does anisotropic traveltime tomography. The algorithm generalizes the well-known techniques of tomographic traveltime inversion in isotropic media by using models discretized into a set of homogeneous elliptically anisotropic cells. Each cell is characterized by two slownesses, and the inclination of the axis of symmetry.

Cross-well geometries usually don't adequately sample the vertical component of the medium's velocity. The opposite happens with the horizontal component of the velocity. Therefore, it is easier to estimate V_x than V_z when using cross-well geometries alone.

In one dimension, both components of the slowness can be estimated accurately if the range of ray angles that is wide enough. Otherwise the problem becomes ill-conditioned. In two dimensions, however, the vertical component of the velocity has poor resolution when compared to the horizontal component. Therefore, the spatial resolution in velocity anisotropy is also poor. In general, it is difficult to separate small variations in velocity anisotropy from reconstruction artifacts.

I have found that 1.5-D models, which consist of dipping elliptically anisotropic layers, are a good compromise between the simplicity and restricted applicability of 1-D models and the complexity and generality of full 2-D models. I use 1.5-D models to illustrate the estimation of velocity anisotropy in a medium with strong anisotropy, strong velocity contrasts, and variable inclination of the axis of symmetry.

When the measurements have limited view, and iterative techniques such as conjugate gradients are used to solve the linearized problem, early termination of the iterations may produce artificial anisotropy. This problem is more severe in 2-D than in 1-D estimation of velocity anisotropy.

Since the inclination of the axis of symmetry is also a variable in the inversion procedure, certain types of azimuthally anisotropic media can be approximated, in particular those formed by dipping, transversely isotropic layers.

The estimated elliptical velocities can be transformed into elastic constants that describe a general TI medium, if compressional and shear wave traveltimes are available. The next chapter addresses this topic. If any of the wave types is not available, the partial solutions obtained are still useful since they can be interpreted in terms of medium properties such a lithology or fine layering, as the field data examples in this chapter show.

Chapter 5

Estimation of elastic constants in heterogeneous transversely isotropic media

Chapter 2 introduced the idea of fitting the traveltimes with elliptical velocity functions as a first step in the estimation of the elastic constants of a homogeneous TI medium. The techniques presented in chapters 3 and 4 (anisotropic ray tracing and anisotropic tomography) generalize to heterogeneous media the method of fitting the data with elliptical velocity functions. After fitting the traveltimes, the next step is the mapping from elliptical velocities to elastic constants. In this chapter, I show how all these techniques work together in the estimation of elastic constants in heterogeneous TI media.

5.1 Introduction

As chapter 2 shows, obtaining the elastic constants of a homogeneous TI medium from *P*-, *SV*- and, *SH*-wave traveltimes is a two-step procedure. The first step is to obtain direct and normal moveout (NMO) velocities by separately fitting traveltimes from each wave type with elliptical velocity functions. The second step is to map these elliptical velocities into elastic constants using equations (2.22) or (2.23). In this chapter I show that when the medium is heterogeneous, the elastic constants can be estimated by applying the procedure for homogeneous media many times to a heterogeneous model described as a superposition of homogeneous blocks. These blocks should incorporate our previous

knowledge about the structure. The direct and NMO velocities needed at each block are estimated tomographically, as explained in chapter 4.

I start by explaining how the data aperture should be constrained to use the algorithm and how those constraints affect the estimation of both anisotropy and heterogeneity. Then I show the application of the technique using synthetic *P*- and *SV*-wave traveltimes generated through a heterogeneous TI model. Finally, I present a field data example from a west Texas oil field. This example shows how the estimation of the elastic constants can add useful information when we study the properties of reservoir and nonreservoir rocks.

5.2 Aperture constraints: consequences

The procedure for estimating elastic constants from *P*-, *SV*- and *SH*-wave traveltimes can be summarized as tomographic estimation of elliptical velocities and transformation of the elliptical velocities into elastic constants. These two steps have opposite requirements in terms of data aperture. On the one hand, the mapping from elliptical velocities to elastic constants requires velocities estimated from rays that travel as closely as possible to one axis of symmetry, which is the assumption made in chapter 2 when deriving the equations that relate elliptical velocities and elastic constants. One the other hand, the tomographic estimation of elliptical velocities requires wide ray angles to improve the conditioning of the problem, the accuracy of the NMO velocities, and the spatial resolution of the result. Therefore, the aperture of the traveltimes used for the inversion should satisfy the following two conditions simultaneously: it shouldn't be too large because otherwise the elliptical approximation may not be adequate, and it shouldn't be too small because otherwise the tomographic estimation of elliptical velocities fails, even if the medium is actually isotropic.

Large ray angles are important for the estimation of moderate and large dips in the medium. Since the procedure doesn't allow the use of large ray angles in the inversion of *P*- and *SV*-wave traveltimes, I assume that the dips in the medium are small. If the dips are not small, they can be estimated first from *SH*-wave, wide-aperture traveltimes (that are truly elliptical), and the result can be used to constrain the boundaries in the inversion of *P*- and *SV*-wave data.

The axes of symmetry of the different homogeneous blocks that describe the model

are assumed to be vertical or near vertical.[1] Therefore, when starting the iterations in the anisotropic traveltime tomography by assuming vertical axes of symmetry, the actual inclinations can be found while the estimation of the elliptical velocities remains accurate, regardless of the wave type. If the axes of symmetry are neither vertical nor close to vertical, we need to find their inclination first by fitting *SH*-wave traveltimes with heterogeneous elliptically anisotropic models, as explained in chapter 4. Once the inclination of the axes of symmetry of the different blocks is known, the elliptical group velocities of *P*- and *SV*-waves at each block are estimated using only rays that travel near the axes of symmetry. This process assumes that the axes of symmetry of the different blocks are in the same plane of the survey, as explained also in chapter 4.

In summary, in the absence of *SH*-wave traveltimes, the medium is assumed to be horizontally layered with vertical axes of symmetry. Small departures from this initial assumption can also be estimated. Larger variations from this initial guess require elliptical *SH*-wave traveltimes that allow the use of large data apertures.

When the inclination of the axes of symmetry varies across the medium, the estimated elastic constants are referred to different coordinate frames, one for each different axis of symmetry. For purposes of interpretation, having the elastic constants referred to different frames is not a problem as long as we also use the inclination of the axes of symmetry. However, for further computations (finite difference modeling, for example) it might be necessary to transform the elastic constants to a common frame. This transformation can be done by using Bond's matrices (Auld, 1990).

5.3 Synthetic example

P- and *SV*-wave synthetic traveltimes were generated using the anisotropic ray tracing algorithm described in chapter 3. Figure 5.1 shows the heterogeneous TI model where the rays were traced. This model shows the variation in depth of $V_{ij} = \sqrt{c_{ij}/\rho}$, the elastic constants transformed to velocity assuming unit density. The cross-well geometry used to compute the traveltimes consists of 92 sources and 92 receivers at each well. The distance between wells is 390 feet, and the separations between consecutive sources or receivers is 23 feet.

[1] They can also be horizontal or near horizontal. The algorithm works equally well in either case because the axes of symmetry of the ellipses are not constrained to be either the major or the minor axis, as explained in section 4.3.3, "Which is the axis of symmetry?."

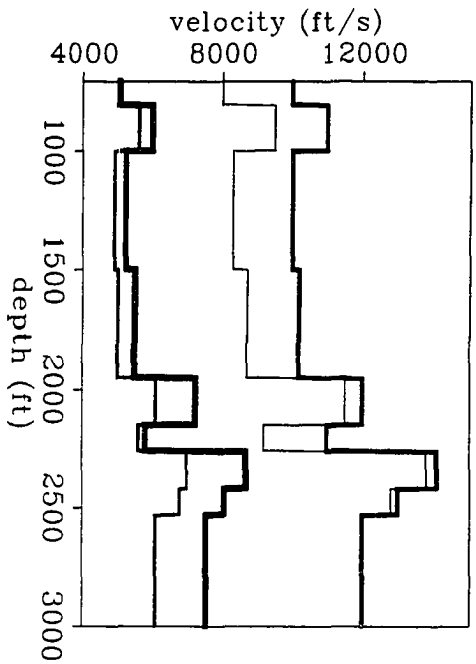

Figure 5.1: Layered TI synthetic model. From left to right the four curves represent the elastic constants in units of velocity V_{44}, V_{13}, V_{33}, and V_{11}, respectively. The density is assumed to be unity.

Since the elastic constants of the medium are known, the corresponding elliptical velocities ($V_{P,x}$, $V_{P,z\text{NMO}}$, $V_{SV,x}$, and $V_{SV,z\text{NMO}}$) can be calculated easily by using the equations derived in chapter 2. Figure 5.2 shows the result. These velocities can be used to check how the algorithm performs in the first step toward the estimation of the elastic constants, that is, the tomographic estimation of the elliptical velocities.

As chapter 2 shows, the paraxial elliptical approximation around the horizontal axis (assuming vertical axis of symmetry) is accurate for angles of less than 30 degrees. For this reason, the inversion only uses rays whose angle measured from the horizontal satisfies this condition. However, no approximation is made in the computation of the synthetic traveltimes through the model of Figure 5.1. The paraxial approximation is made only during the inversion procedure in which the rays are traced in elliptically anisotropic instead of transversely isotropic models.

The fact that the straight line that connects a source-receiver pair forms a small angle with respect to the horizontal doesn't necessarily mean that the angle of the corresponding ray path is also small. The angle of the ray path increases in low-velocity layers and

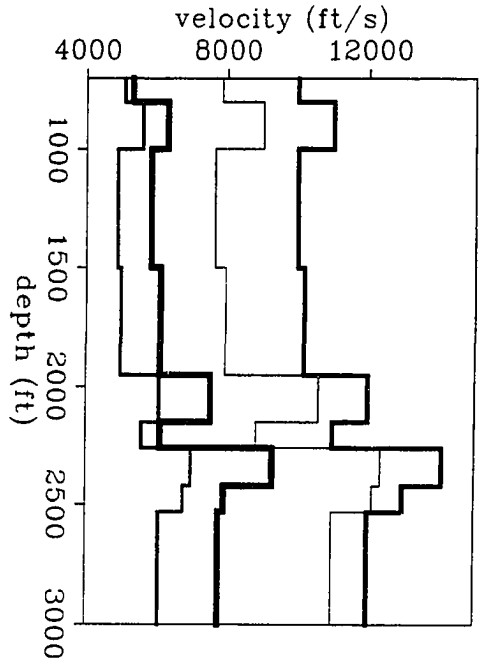

Figure 5.2: Theoretical elliptical velocities around the horizontal axis calculated from the elastic constants shown in Figure 5.1. From left to right the four curves represent $V_{SV,x}$, $V_{SV,z\text{NMO}}$, $V_{P,z\text{NMO}}$, and $V_{P,x}$, respectively.

decreases in high-velocity layers. However, if the velocity contrasts are not too strong, it should be enough to look at the straight line that connects source and receiver to select the rays that satisfy the proper constraints.

Figure 5.3 shows the result of inverting the P-wave traveltimes. This figure also shows the theoretical elliptical velocities calculated from the elastic constants. The estimation of the horizontal P-wave velocity is, as expected, almost perfect, whereas the vertical NMO velocity is slightly overestimated ($\approx 3\%$) in all layers. As Figure 5.4 shows, the estimation of the vertical NMO velocity is more accurate when inverting SV-wave traveltimes than when inverting P-wave traveltimes, which means that, for the range of ray angles used, the elliptical approximation works better for SV-waves than for P-waves. The error in $V_{SV,z\text{NMO}}$ is less than one percent.

The errors in the NMO velocities $V_{P,z\text{NMO}}$ and $V_{SV,z\text{NMO}}$ come from using an elliptical approximation for ray angles that are not sufficiently small. When the model is truly elliptical, the estimation of the NMO velocities is accurate, as I show in chapter 4.

The variation with depth in the theoretical P- and SV-wave elliptical velocities has been estimated accurately. Therefore, by using these two models of elliptical velocities, we can

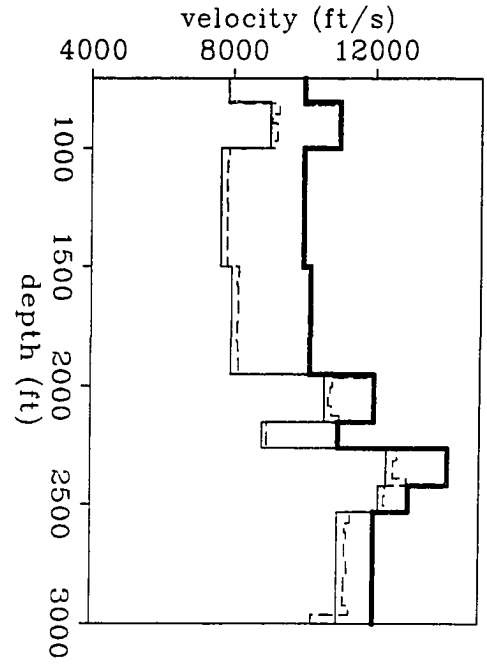

Figure 5.3: *P*-wave elliptical velocities. Dashed lines: result of the inversion of *P*-wave traveltimes with a ray angle of less than 30 degrees. Continuous lines: theoretical values. The curves with lower velocity correspond to $V_{P,z\text{NMO}}$, and the ones with higher velocity correspond to $V_{P,x}$.

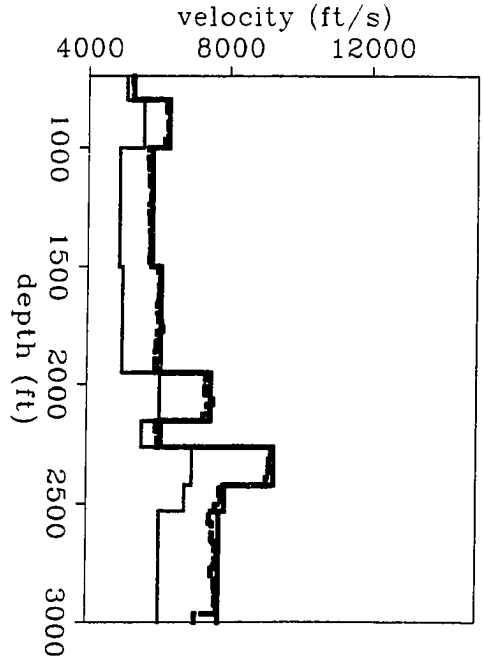

Figure 5.4: *SV*-wave elliptical velocities. Dashed lines: result of the inversion of *SV*-wave traveltimes with a ray angle of less than 30 degrees. Continuous lines: theoretical values. The curves with lower velocity correspond to $V_{SV,x}$, and the ones with higher velocity correspond to $V_{SV,z\text{NMO}}$.

also expect an accurate estimation of the elastic constants, as Figure 5.5 shows.

Since P- and SV-wave traveltimes are inverted separately and the interfaces are not constrained to move consistently with both data sets, the models obtained for P- and SV-wave elliptical velocities may not have all the interfaces at exactly the same depths. As a consequence, artificial thin layers (spikes) may appear when we estimate the elastic constants because there may be slight relative mispositions of the same boundaries in the two models. In Figure 5.5 these spikes are removed by applying a median filter to the elastic constants after the mapping from elliptical velocities. Another way to solve this problem is by describing the interfaces with the same parameters for both P- and SV-wave velocity models and inverting the two sets of traveltimes simultaneously.

Depending on the radiation pattern of the source, traveltimes that correspond to nearly horizontal rays may not always be available for either P- or SV-waves. When this happens, it may be necessary to use ray angles that are far from the horizontal because nothing else is available. Figure 5.6 shows an example where SV-wave elliptical velocities have been estimated by using ray angles between 28 and 36 degrees. The estimated horizontal component of the velocity is as accurate as in Figure 5.4 even though this component is not well sampled by the ray paths used. The error in $V_{SV,z\mathrm{NMO}}$ increases when using larger ray angles. However, as Figure 5.7 indicates, the error in the estimation of the elastic constants is still small because the P-wave elliptical velocities were estimated using small ray angles.

In the field data example that follows, SV-wave traveltimes are not available for small vertical offsets.

5.4 Field data example

Cross-well data were recorded at the McElroy field, a carbonate reservoir of the Permian Basin in west Texas. This field has large oil reserves. It was discovered in 1926 and has been under continuous water-flooding since the early 1960s. McElroy field produces mainly from intertidal and shallow-shelf dolostones and siltstones of the Grayburg formation, which is a stratigraphic/structural trap. Hydraulic fracturing has stimulated reservoir performance. Porosity and permeability data from cores show that the Grayburg formation is very heterogeneous, with significant changes over short distances. The reason for the heterogeneity is that anhydrite and gypsum have plugged the pores (Avasthi et

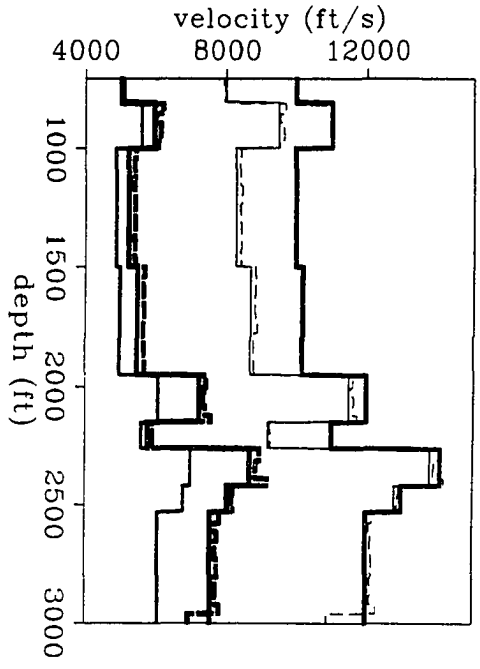

Figure 5.5: Elastic constants that control P- and SV-wave propagation. Dashed lines: estimated. Continuous lines: given. From left to right the four pairs of curves represent V_{44}, V_{13}, V_{33}, and V_{11}, respectively.

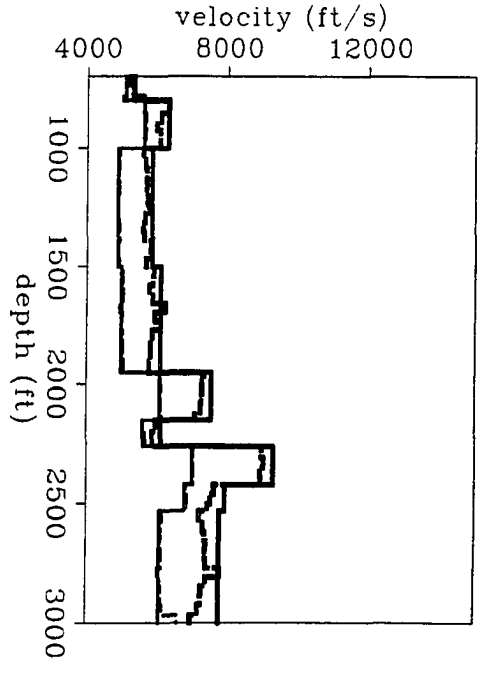

Figure 5.6: SV-wave elliptical velocities. Dashed lines: result of the inversion of SV-wave traveltimes with ray angles between 28 and 36 degrees. Continuous lines: theoretical SV-wave elliptical velocities. The curves with lower velocity correspond to $V_{SV,x}$ and the ones with higher velocity correspond to $V_{SV,z\mathrm{NMO}}$.

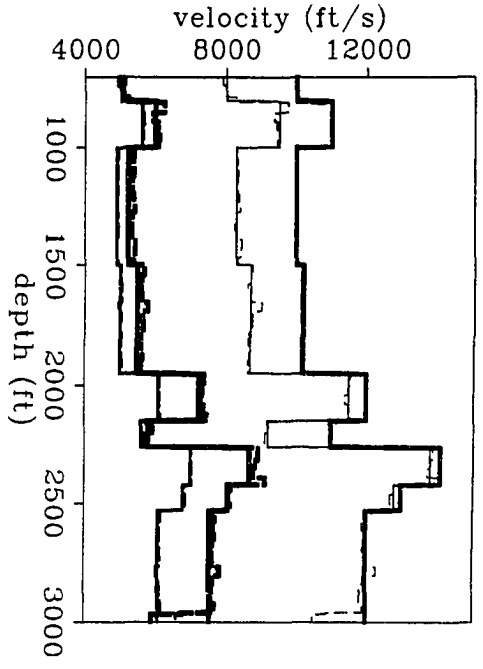

Figure 5.7: Elastic constants that control P- and SV-wave propagation. Dashed lines: elastic constants estimated when the ray angles used in the tomographic inversion of SV-wave traveltimes are between 28 and 36 degrees. The ray angles used to obtain the P-wave elliptical velocities are between 0 and 30 degrees, as in Figure 5.5. Continuous lines: original elastic constants. From left to right the four pairs of curves represent V_{44}, V_{13}, V_{33}, and V_{11}, respectively.

al., 1991). Structurally, the region is flat with mildly increasing dips at the bottom of the surveyed section (Lazaratos et al., 1992). The profile area is part of three 20-acre, five-spot patterns in a CO_2 pilot study.

A cylindrical piezoelectric bender was used as the source, a linear upsweep from 250 to 2000 Hz. Well spacing is 184 feet. The receiver well in the cross-well profiling was an observation well drilled for the CO_2 study, and the receiver system was a nine-level array of hydrophones. The plane of the survey is almost perpendicular to the direction of natural fractures measured in a nearby well (Avasthi et al., 1991). The target of the experiment was a reservoir between 1850 and 1960 feet. Sources and receivers were centered around the reservoir, from 1650 to 2150 feet.[2] The vertical spacing between sources and receivers was 2.5 feet. The survey consists of nearly 36 000 traces (201 sources $\times$ 178 receivers) sampled at 0.2 ms. More details about the data acquisition can be found in Harris et al. (1992).

Figure 5.8 shows a common receiver gather recorded at 1880 feet. Data editing and geometry definition was performed before picking the data. The total number of traveltimes

[2]Reservoir depths are changed for purposes of presentation in this chapter.

picked from the field data was 33 519 and 20 887 for *P*-waves and *S*-waves, respectively. Van Schaack et al. (1992) show that the source can be modeled as a radial horizontal point source, which explains why no shear waves are clearly visible in the data for ray angles less than ≈ 28 degrees with respect to the horizontal, as Figure 5.8 shows.

P-wave energy is converted to shear energy at the source well. If the source well is perfectly cylindrical, and if the downhole source is positioned symmetrically within the source well, the polarization of the converted energy recorded at the receiver well is contained in the plane of the survey. Therefore, it is safe to assume that most of the recorded shear energy in this experiment corresponds to the *SV*-mode.

The *P*-wave traveltimes used for the inversion were from sources and receivers forming angles between 9 and 36 degrees with the horizontal. Even though the corresponding range of ray angles may be slightly different depending on how strong the velocity contrasts are, I still expect most ray angles at all layers to fall within the range of validity of the elliptical approximation. By applying this constraint on the data aperture, the number of *P*-wave traveltimes was reduced to 12 258 from the original 33 519. For similar reasons, the number of *S*-wave traveltimes was reduced to 2922, which corresponds to sources and receivers forming angles between 29 and 35 degrees.

The initial model for the tomographic inversion of *P*-wave traveltimes is homogeneous isotropic. The model is described by 200 horizontal layers of equal thickness (2.5 feet). Figure 5.9 shows the elliptical velocities that result after inverting the data. $V_{P,z\mathrm{NMO}}$ is larger than $V_{P,x}$ in some strata, which indicates that the anisotropy is not caused by fine, horizontal layering, according to the results of section 2.7 "Constraints on elliptical velocities in layered media." The mean absolute value of the residuals [equation (4.12)] for this model is 0.086 ms.

Figure 5.10 shows the elliptical velocities that result from the inversion of shear-wave traveltimes. The initial model in this case was also homogeneous isotropic and described by 200 layers of equal thickness. Seven layers were eliminated during the inversion procedure. $V_{SV,z\mathrm{NMO}}$ is close to $V_{SV,x\mathrm{NMO}}$, which means that, as discussed also in section 2.7, the *P*-wave anisotropy at this site is close to elliptical. As Figures 5.9 and 5.10 show, the shear-wave anisotropy at this site is smaller than the compressional wave anisotropy. The mean absolute value of the residuals computed for the model in Figure 5.10 is 0.240 ms, approximately equal to the sampling interval.

Finally, the elliptical velocities of Figures 5.9 and 5.10 are transformed into elastic

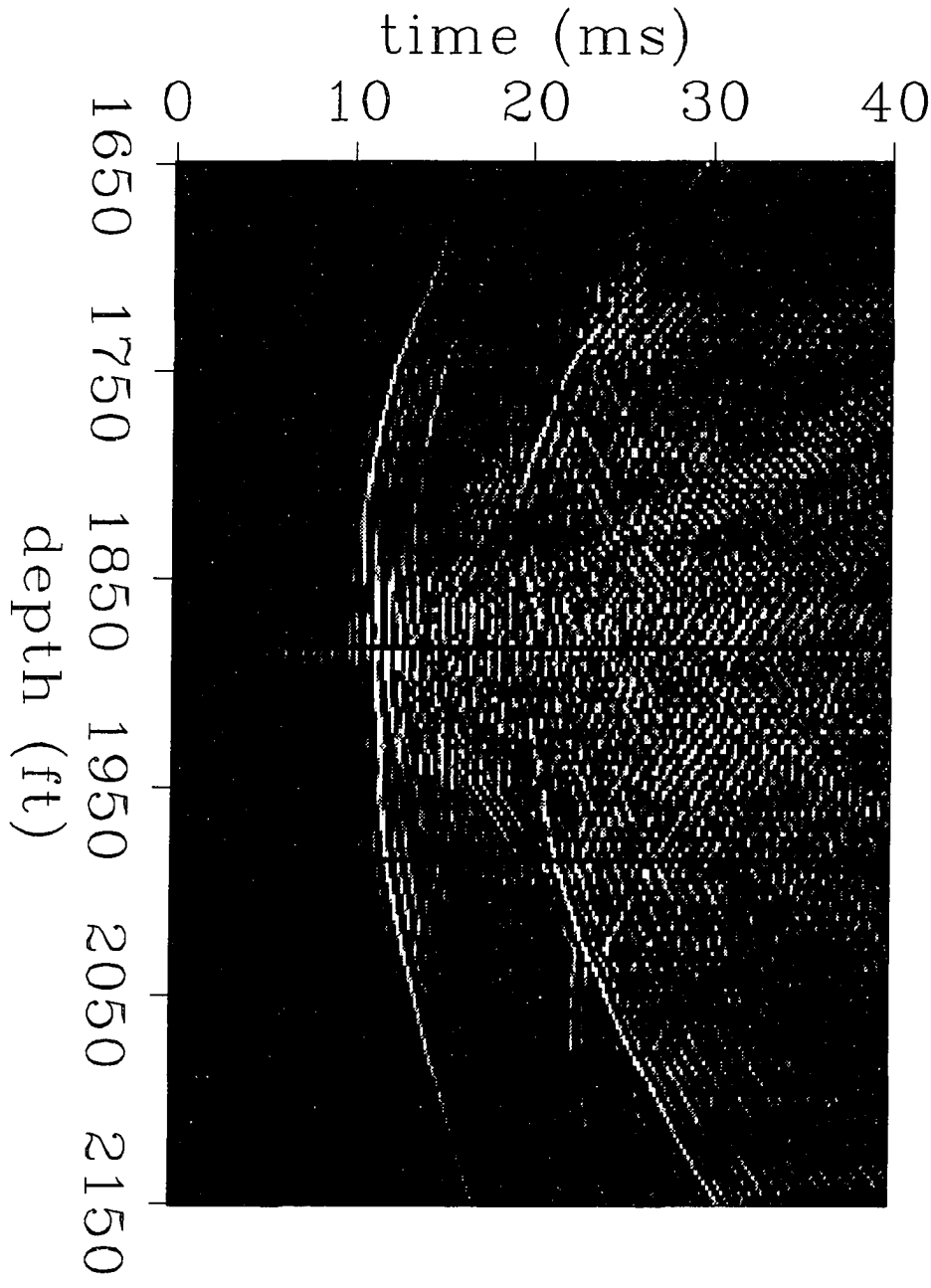

Figure 5.8: Common receiver gather recorded at 1880 feet. The source depth interval is 2.5 feet. The well-to-well separation is 184 feet. First arriving compressional and shear waves are clearly visible at most vertical offsets. Other wave modes are also visible. The target of the experiment was a reservoir between 1850 and 1960 feet.

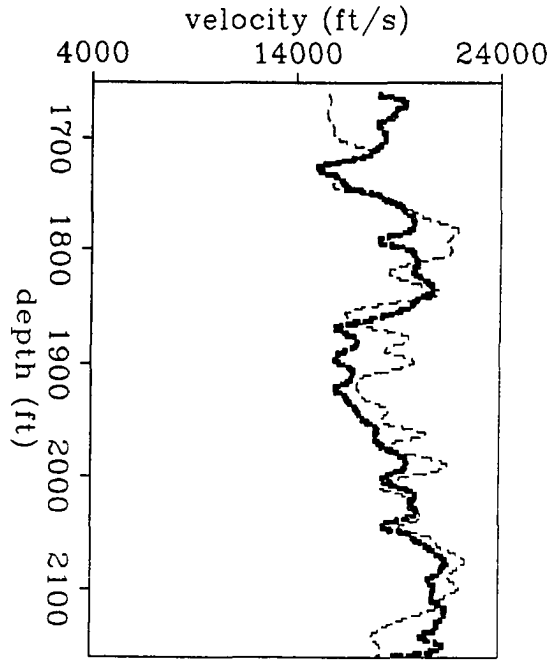

Figure 5.9: *P*-wave elliptical velocities estimated from field data. Thick line: $V_{P,x}$. Thin line: $V_{P,zNMO}$. The model is described by 200 horizontal layers.

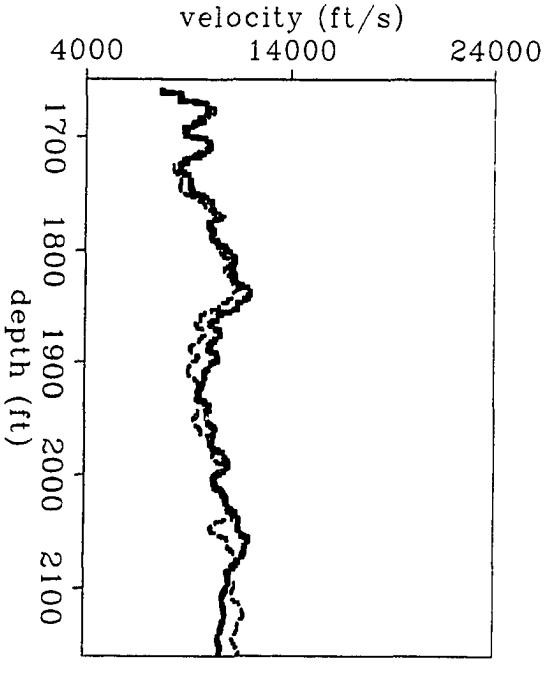

Figure 5.10: *S*-wave elliptical velocities estimated from field data. Thick line: $V_{SV,zNMO}$. Thin line: $V_{SV,x}$. The model is described by 193 horizontal layers.

constants by using equation (2.3) at each depth. Figure 5.11 shows the result of the transformation. V_{11} and V_{33} (horizontal and vertical P-wave velocities, respectively) vary more rapidly than V_{44} (SV-wave velocity). V_{33} is almost the same as $V_{P,z\mathrm{NMO}}$ because the shear wave anisotropy is not significant, as Figure 5.10 shows. The difference $V_{11}-V_{33}$ alternates between zero or negative in the interval between 1700 and 2100 feet. If we assume that the anisotropy is caused by fine layering, such changes in $V_{11}-V_{33}$ can be explained by a sequence of isotropic and anisotropic strata with horizontal axes of symmetry, probably vertically fractured. The reservoir between 1850 and 1960 feet corresponds to one stratum that is probably vertically fractured, which suggests that other intervals where $V_{11} < V_{33}$ may also correspond to vertically-fractured reservoir zones.

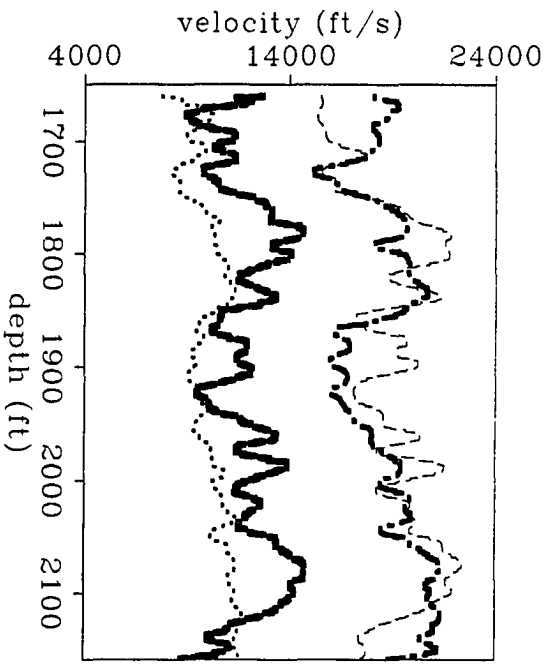

Figure 5.11: Elastic constants at the McElroy site (in units of velocity) estimated from the elliptical velocities of Figures 5.9 and 5.10, assuming a TI medium. Dotted line: V_{44}. Thick-dashed line: V_{13}. Dotted-dashed line: V_{11}. Thin-dashed line: V_{33}.

Figure 5.12 compares the horizontal and vertical velocities estimated from the cross-well measurements with the vertical shear and compressional velocities derived from the sonic log. Comparing shear-wave velocities yields the results expected for a TI medium: the vertical shear velocity from the sonic log is the same as the horizontal shear velocity derived from cross-well measurements. For the compressional velocities, however, the results are not as expected: the sonic log velocity is closer to the horizontal velocity than

to the vertical velocity estimated from cross-well traveltimes.

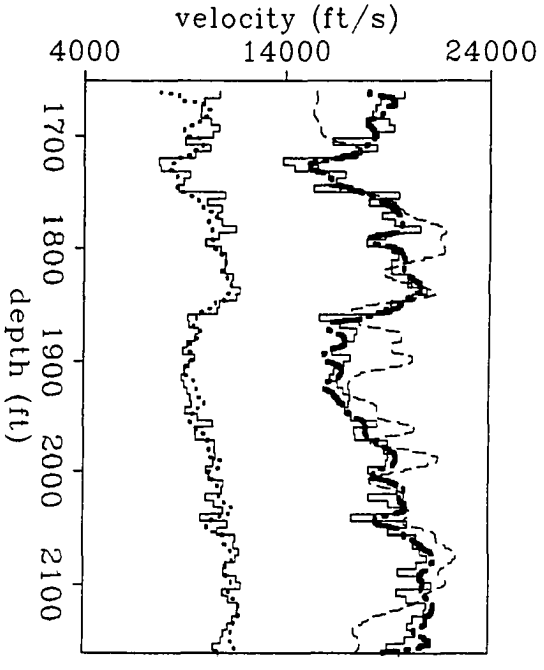

Figure 5.12: Elastic constants (in units of velocity) estimated from cross-well traveltimes compared with sonic logs blocked every six feet. Continuous line at the left: shear sonic velocity. Continuous line at the right: compressional sonic velocity. Dotted line: V_{44}. Dotted-dashed line: V_{11}. Thin-dashed line: V_{33}.

The differences between vertical P-wave sonic velocity and vertical P-wave velocity estimated from cross-well traveltimes can be explained in several ways that are consistent with the idea of vertically fractured strata alternating with isotropic strata. One explanation is that fluids used when drilling can penetrate the reservoir zones causing a decrease in the compressional velocities of waves that travel close to the well without affecting either the velocities of waves that travel far from the well or the shear velocities. Another explanation assumes that the vertical fractures are embedded in a slow, fluid-filled matrix. The fractures are well-separated and filled with fast material (anhydrite), which can effectively increase the vertical velocity of waves that travel vertically in the interwell region without affecting either the velocity of waves that travel horizontally (because the fractures are thin) or the velocity of high-frequency waves that travel around the borehole in the low-velocity matrix. Strong, lateral heterogeneities in the vertical component of the velocity may cause the type of variation observed in the results, because the model doesn't account for them. This possibility, however, is less likely because reflection images of the site show fairly laterally homogeneous layers (Lazaratos et al, 1992).

Having out-of-plane shear arrivals would help to confirm the hypothesis of vertical fractures, by allowing us to look at the shear-wave splitting in the near horizontal direction.

5.5 Conclusions

The procedure used to estimate elastic constants in heterogeneous TI media is a generalization of the technique presented in chapter 2 for estimating elastic constants in homogeneous TI media. For homogeneous media, traveltimes from different wave types are fitted with elliptically anisotropic models. The elliptical velocities that result are then transformed into elastic constants. For heterogeneous media, the elliptical fit is performed by using anisotropic traveltime tomography, and the transformation to elastic constants is performed locally at each point in space.

The examples presented in this chapter show that the procedure is accurate as long as the maximum aperture satisfies the following constraints: it must be not too small because that would impede the estimation of the NMO velocities and not too large because the elliptical approximation might not be adequate.

In this chapter, I tested the algorithm with simple layered models. The estimation of elastic constants in media with more complex heterogeneities may require traveltimes from wider apertures, which could yield in less accurate results. This problem can solved by using traveltimes from all wave types from different recording geometries.

Appendix A

Singular value decomposition for cross-well tomography

Singular value decomposition is performed on the matrices that result in tomographic velocity estimation from cross-well traveltimes in isotropic and anisotropic media. For a simple recording geometry, this appendix shows the singular vectors in both data and model space along with their corresponding singular values.

A.1 Introduction

In ray theoretic traveltime tomography, the solution of a linear system of equations is the heart of the problem. Solving this linear system transforms variations in traveltimes into variations in model parameters. This transformation from data to model depends on the properties of the matrix that describes the linear system, and singular value decomposition (SVD) is the tool for studying such properties.

SVD has been applied in the past to study the structure of the matrices involved in tomographic traveltime inversion problems. White (1989), Bregman et al. (1989), and Pratt and Chapman (1992) among others, present singular values and singular vectors in model space for cross-well geometries. Stork (1992) also shows singular values and the corresponding singular vectors in model space for the problem of reflection tomography. All these studies, however, have not completely reported the results of the SVD because they make no reference to the properties of the singular vectors in data space.

For a small cross-well geometry, in this appendix presents the complete results of the

SVD (singular values and singular vectors in both data and model spaces) of matrices that result from the following four types of parametrization: 1-D isotropic, 2-D isotropic, 1-D anisotropic, and 2-D anisotropic. The anisotropy is assumed to be elliptical. These four models differ as to how they incorporate the prior information that might be available about the medium. My results show that the model that makes more assumptions about the medium (1-D isotropic) is the one that can be estimated better whereas the model that makes fewer assumptions (2-D anisotropic) contains a large null space that may distort the anisotropy as well as the heterogeneities in the solution. Although these results are not surprising, they remind us that when prior information about the medium is available it is important to incorporate it in the parametrization, because otherwise the results may not even contain the expected features or they may be severely distorted, especially when the medium is anisotropic.

The results of the SVD of the previous matrices show how damping the matrix inversion affects the solution when the velocity model is isotropic and anisotropic. As expected, when the model is isotropic, damping the solution results in smoothness in the image. However, when the model is anisotropic, damping not only creates smoother images but also may distort the anisotropy or create artificially anisotropic results.

This appendix is an example of the type of analysis that can be performed for any recording geometry to gain insight into how data and model parameters relate. This insight can help to improve both the data acquisition and the estimation of the parameters.

A.2 The linear system

Regardless of how the model is described, the problem of ray theoretic traveltime tomography always reduces to the solution of a linear system of equations of the form:

$$\underset{\sim}{\mathbf{J}}\, \boldsymbol{m} = \boldsymbol{t}, \tag{A.1}$$

where $\underset{\sim}{\mathbf{J}}$ is a matrix whose elements depend on the ray paths and on how the model is described, $\boldsymbol{m}$ is the vector of model parameters, and $\boldsymbol{t}$ is the vector of measured traveltimes. The vectors $\boldsymbol{m}$ and $\boldsymbol{t}$ may also represent *variations* with respect to a given model and to measured traveltimes, respectively.

The model space represented by $\boldsymbol{m}$ consists of two separate models: one for the heterogeneities and one for the velocities. If the model for velocities is isotropic, the elements

$\boldsymbol{m}$ usually represent the coefficients of the expansion of the slowness model in a basis function that describes the model of the heterogeneities. Moreover, if the basis function is also orthogonal (i.e., its different elements do not overlap), each component of $\boldsymbol{m}$ represents the slowness within one particular region in space. Although other basis functions that don't have the property of orthogonality have been recently proposed (Van Trier, 1988; Harlan, 1989; Michelena and Harris, 1991), those that have such a property are still the most widely used to represent 1-D layered models (large, rectangular cells) and arbitrary 2-D variations (small, square cells). In this appendix, I focus on these two types of basis function to describe the model of heterogeneities. In both cases, the isotropic slowness model can be expressed as

$$S(x,z) = \sum_{j=1}^{N} S_j R_j(x,z), \tag{A.2}$$

where $R_j(x,z)$ is nonzero only at the j^{th} cell, S_j is the slowness within that cell, and N is the total number of cells (either layers or square pixels). The corresponding vector of model parameters is

$$\boldsymbol{m} = (S_1, S_2, ..., S_N)^T. \tag{A.3}$$

When the model for velocities is anisotropic, our choices for defining the global model space $\boldsymbol{m}$ increase substantially because all the models available in the isotropic case for describing the heterogeneities are now combined with all the different models available for describing the anisotropy. The selection of the proper combination velocity-model/heterogeneity-model should be made according to any prior knowledge we might have about the medium. The examples that follow show that introducing prior information in the proper way in each of these two models helps to estimate both of them more accurately but, unfortunately, if one of the models is incorrect or too general, the results obtained with the other model may be also incorrect.

In this appendix, I assume that the anisotropy is elliptical and that the model of heterogeneities is described either by horizontal homogeneous layers or by square pixels. Even though most rocks are not elliptically anisotropic, by using elliptical anisotropy I can show some of the difficulties we may encounter when tomographically estimating variations in velocity with both direction and position. When the anisotropy is elliptical, the representation of the slowness images is a generalization of expression (A.2) as follows:

$$S_x(x,z) = \sum_{j=1}^{N} S_{x_j} R_j(x,z), \tag{A.4a}$$

$$S_z(x,z) \;=\; \sum_{j=1}^{N} S_{z_j} R_j(x,z). \tag{A.4b}$$

The corresponding vector of model parameters is

$$\boldsymbol{m} \;=\; (S_{x_1}, S_{x_2}, ..., S_{x_N}, S_{z_1}, S_{z_2}, ..., S_{z_N})^T, \tag{A.5}$$

where S_{x_j} and S_{z_j} are the horizontal and vertical components of the slowness, respectively.

If the vector $\boldsymbol{m}$ is not transformed into an image(s), it is difficult to understand the relations among its different components. The same applies for the vector $\boldsymbol{t}$ of traveltimes. A simple method of mapping $\boldsymbol{t}$ into an image has been used in recent publications (see, for example, Squires et al., 1992). The mapping consists of plotting each component of $\boldsymbol{t}$ at its corresponding source-receiver location in a 2-D space where the axes are source depth and receiver depth. Traveltimes corresponding to sources and receivers at the same depth map into the diagonal of the image and other traveltimes corresponding to rays that travel at nonzero angle with respect to the horizontal map off the diagonal. This transformation of the vector $\boldsymbol{t}$ into an image and the transformations (A.2) and (A.4) are used extensively in the next sections to visualize the vectors in both data and model space that result from the SVD.

A.3 SVD: a short review

Any MxN-matrix $\underset{\sim}{\mathbf{J}}$ can be decomposed in the following way (Golub and Van Loan, 1989):

$$\underset{\sim}{\mathbf{J}} \;=\; \underset{\sim}{\mathbf{U}}\,\underset{\sim}{\mathbf{L}}\,\underset{\sim}{\mathbf{V}}^T, \tag{A.6}$$

where $\underset{\sim}{\mathbf{U}}$ is an MxM orthogonal matrix of eigenvectors that span the data space, $\underset{\sim}{\mathbf{V}}$ is an NxN orthogonal matrix of eigenvectors that span the model space, and $\underset{\sim}{\mathbf{L}}$ is an MxN diagonal matrix whose elements are the singular values of $\underset{\sim}{\mathbf{J}}$. The columns of $\underset{\sim}{\mathbf{U}}$ ($\mathbf{u}$) are the eigenvectors of $\underset{\sim}{\mathbf{J}}\,\underset{\sim}{\mathbf{J}}^T$, and the columns of $\underset{\sim}{\mathbf{V}}$ ($\mathbf{v}$) are the eigenvectors of $\underset{\sim}{\mathbf{J}}^T\underset{\sim}{\mathbf{J}}$. The decomposition (A.6) is called singular value decomposition.

When a singular value is zero, the corresponding singular vector in data space cannot be mapped into model space or vice versa. Data vectors or model vectors with zero singular value belong to the null space and cannot be resolved. When a singular value is not zero but is small compared with the largest one (i.e, the condition number is large), the contribution of the corresponding eigenvectors to the solution must be eliminated or attenuated, that is regularized, because the matrix inversion may become unstable.

A.4 SVD: application

SVD (Dongarra et al., 1979) was performed on the matrix $\underset{\sim}{\mathbf{J}}$ after describing the model space as described by equations (A.2) and (A.4). In order to represent the results of the SVD, I show the singular values simultaneously with the singular vectors in data and model space, both sets of vectors having been transformed into images as explained in the previous section. This representation of the SVD results follows Pratt and Chapman (1992), with the addition of the singular vectors in data space.

The ray geometry used to compute the SVD for the differents parametrizations is shown in Figure A.1. It is the same as the one used by Pratt and Chapman (1992): five sources and five receivers in separate wells in a constant slowness medium. When the model is isotropic, the matrix $\underset{\sim}{\mathbf{J}}$ depends only on the ray geometry and when the model is anisotropic, $\underset{\sim}{\mathbf{J}}$ depends on both the ray geometry and the slowness model (which is constant in this case) which means that even when the rays are straight the tomographic estimation of velocity anisotropy is in general a nonlinear problem. Ray bending adds another nonlinearity to the problem.

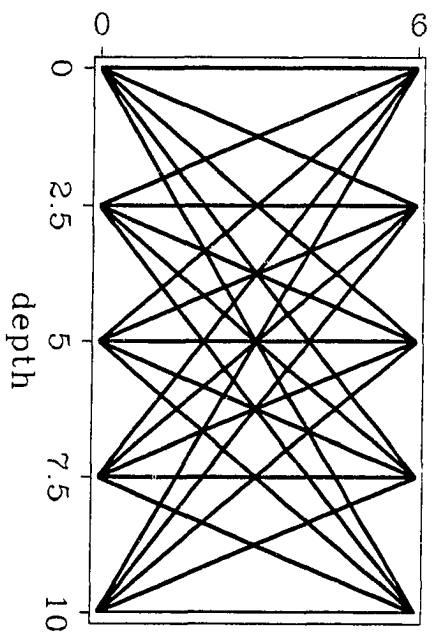

Figure A.1: Recording geometry used to do the SVD for the different parametrizations. The slowness is constant and therefore, the ray paths are always straight.

A.4.1 Isotropic models

Figure A.2 shows the SVD when the model is discretized using six horizontal isotropic layers [equation (A.2)]. The differences among the singular values are small, which means that the problem is well-conditioned. The largest singular values correspond to singular vectors in data and model space (**u** and **v**, respectively) whose components are roughly of the same magnitude. With this parametrization only some "big structures" (averages) in data space can be explained whereas in model space all the parameters can be well resolved. By representing the singular vectors in data space **u** as images, it is possible to identify source-receiver pairs whose traveltimes belong to the null space and therefore cannot be resolved or have no influence in the estimation of the model parameters. For this reason, errors in these particular traveltimes (noise) will also have little or no effect in the solution, which means that this parametrization is not too sensitive to errors in the data.

Allowing lateral variations in the previous parameterization results in a matrix $\underset{\sim}{\mathbf{J}}$ whose SVD is shown in Figure A.3. The largest singular value corresponds roughly to horizontal layers (in model space) and non-horizontal rays (in data space). As the singular values decrease, the eigenvectors in model space tend to contain more horizontal and high-frequency variations and the eigenvectors in data space tend to span near and far vertical offsets (diagonal and non-diagonal structures in the data images). In model space, the smallest singular values correspond to "pure" horizontal variations, which means that the data is not sensitive to this type of variation in the model. In data space, the smallest singular values correspond to rapid changes among nearby traveltimes that have little or no influence on the model. Rapid changes among nearby traveltimes might be produced by noise that, unfortunately, is not necessarily confined to the less influential part of the data. Therefore, in some applications it might be necessary to damp the effect of singular values larger than those contained in the null space in order to attenuate the effect of certain components of the noise.

The results shown in the previous two figures are as expected. In both cases the largest eigenvalues correspond to gross features in both model and data space. When few parameters compared with the number of data points are used (Figure A.2), the data is not well resolved, and when the number of parameters is increased, some components of the model (pure lateral variations, for example) may be difficult or impossible to retrieve from the given data, even if the problem is overdetermined as in Figure A.3.

Even though these results were expected, they have received little attention. The discretization of the model in square pixels assumes that we don't know anything about the spatial variations in the medium, unlike the discretization of the model in layers. Since the discretization of the model in layers is a subset of the discretization of the model in square pixels, we may think that whatever can be estimated by using homogeneous layers can be also estimated by using homogeneous square pixels. What Figures A.2 and A.3 show is that this statement is not necessarily true. The estimation of the parameters depends on how the data and parameters relate to each other. In problems of tomographic estimation of velocities, 2-D inversions are done often in places that are known to be isotropic and horizontally layered in order to account for all possible "unexpected" variations in the medium. The extra degrees of freedom (and the null space) introduced in the inversion have to be penalized appropriately in the objective function, which produces an image with less resolution overall than the one obtained by directly estimating the parameters of a 1-D model. Of course, if well logs are available and the medium is known to be isotropic and horizontally layered, 1-D inversions are not interesting, and the intrinsic advantages of the parametrization (fewer unknowns and better conditioning) are not useful. However, as the next section shows, if the medium is anisotropic and known to be horizontally layered, using a model of heterogeneities that appropriately incorporates such prior information can make the difference between retrieving or not (accurately) variations of velocity as a function of direction.

The large number of data singular vectors **u** contained in the null space in Figure A.2 also suggests that, if the medium is known to be isotropic and horizontally layered, the data acquisition can be optimized in order to increase the number of measurements that influence the solution, which results in a better estimation of the velocities.

A.4.2 Anisotropic models

The SVD for a 1-D anisotropic parametrization [equation (A.4)] is shown in Figure A.4. The upper half of each eigenvector in model space corresponds to $S_x(x,z)$, the lower half to $S_z(x,z)$. As expected, the largest singular values correspond to gross features in both model and data space. In descending order of singular value, the corresponding singular vectors in data space span first $S_x(x,z)$, then $S_z(x,z)$. The least sensitive part of the model (singular values 11 and 12) is spanned by vectors that contain only information about $S_z(x,z)$. In data space, the behavior for the largest singular values is similar to the

isotropic 1-D case.

Figure A.5 shows the SVD when the model is 2-D anisotropic. The result for this parametrization is roughly a combination of the SVD for the 2-D isotropic and the 1-D anisotropic model (Figures A.3 and A.4 respectively); that is, vertical variations in $S_x(x,z)$ correspond to the largest singular values and horizontal and high-frequency variations in $S_z(x,z)$ to the smallest ones. Nearly half the vectors in the null space (Figure A.6) contain information about $S_z(x,z)$ only and the other half contain information about both $S_x(x,z)$ and $S_z(x,z)$. These vectors cannot be estimated from the data.

Figures A.4, A.5, and A.6 show that when we introduce anisotropy in the model, the sensitivity of the data to the vertical component of the slowness is lower than the sensitivity to the horizontal component, which is not a surprise for cross-well geometries that don't adequately sample the vertical direction. This limitation, however, doesn't impede an accurate estimation of variations of velocity anisotropy with position if we use at the same time the proper model to describe the heterogeneities, as shown in Figure A.4, where most singular vectors in model space correspond to large singular values.

When using a model that assumes nothing about the heterogeneities (square pixels), estimating spatial variations in slowness anisotropy may become a very difficult task because we have to deal with the features of the medium about which the data give less information: horizontal and high-frequency variations in the vertical component of the slowness. Even if the inversion can retrieve the singular vectors corresponding to the smallest singular values, the result can still be images with different resolutions for the horizontal and the vertical components of slowness because most vectors in the null space are related to the vertical component (Figure A.6).

For these reasons, performing 2-D inversions in places known to be one dimensional may create serious problems, in particular when the model is anisotropic. From Figure A.4 we see that all variations in $S_x(x,z)$ can be retrieved from the data because the smallest singular values are related to $S_z(x,z)$ only. However, when we allow 2-D variations in the model, several components of $S_x(x,z)$ go to the null space, as Figure A.6 shows. This fact has two implications. First, features that could be easily recovered with one parametrization have become more difficult or impossible to recover with another parametrization that is more general. Second, taking 1-D averages or smoothing across the horizontal direction 2-D images is not necessarily the same as performing true 1-D inversions, because the 2-D images may be less accurate and contain more artifacts than the images obtained using

1-D parametrizations.

When the velocity model is isotropic, a common way to deal with the noise and ill-conditioning when solving the system (A.1) is by damping the least-squares solution or by truncating the SVD. The purpose of these two techniques is to attenuate or eliminate the effect of the smallest singular values of the problem. When the model is isotropic, damping translates into smoothing because what is being attenuated are the high frequency and horizontal variations in the model. However, when the velocity model is anisotropic, damping out the smallest singular values affects not only the smoothness of the model but also its anisotropy (or isotropy) because the effect of the vertical component of the slowness compared with the horizontal has also been reduced. Therefore, common techniques used to regularize the problem in isotropic media may not be adequate in anisotropic media because they may introduce artificial anisotropy.

Besides damped least-squares or SVD truncation, conjugate gradients (CG) is another common way to solve the system (A.1). In practice, if the data energy distribution among the different singular values is even, early CG iterations tend to be more sensitive to the largest singular values, whereas later iterations tend to be affected by both large and small singular values (Stork, 1988). For this reason, stopping the CG iterations after a small number of steps is similar to the effect of damping or of truncating the SVD (Scales and Gersztenkorn, 1988). As a consequence, when the model is anisotropic, early truncation of the CG iterations may also produce artificially anisotropic results because the horizontal component of the slowness converges faster than the vertical, which belongs to the less sensitive part of the model. Figures 4.7 and 4.8 show examples of how the two components of the slowness converge at different speeds. Early truncation of the iterations may be necessary because of noise or ill-conditioning.

The effect of damping can also be seen in data space. On the one hand, when the damping is large, only gross features in data spaced are resolved. On the other hand, when the damping is small or zero, the high-frequency variations in the data that correspond to the smallest singular values can be also resolved. Therefore, depending on the amount of damping (or, equivalently, where the SVD solution is truncated or when the CG iterations are terminated) some portions of the data may be better resolved than others, which has to be taken into account when interpreting traveltime residuals.

A.5 Conclusions

By performing the SVD of the matrices that result from a small scale numerical experiment, I have shown the relations between data and model space for four different parametrizations. The parametrizations vary according to the amount of prior information that they contain about the medium.

All the results have in common that the largest singular values correspond to gross features in both data and model space. The main differences among the results are in the type of feature in data and model space that the small singular values represent, the size of the null space, and the effect of regularization when dealing with such insensitive parts of the data and the model. When the model is 1-D isotropic, the problem is well conditioned and all the parameters can be resolved well but the resolution of the data is poor. For this type of model cross-well traveltime tomography performs the best if the medium is also 1-D isotropic.

I have generalized the 1-D isotropic model in three ways: by allowing the layers to vary lateraly, to be anisotropic, and to be both heterogeneous and anisotropic. The effect of lateral heterogeneities in the data was negligible even when the problem was overdetermined. Lateral heterogeneities also introduced into the model high-frequency variations whose influence in the inversion needs to be attenuated. The effect of anisotropy in one dimension was to introduce structures in the vertical component of the slowness that are not sensitive to the data. Most other vertical variations, however, can still be easily retrieved. The effect of lateral variations and anisotropy in the parametrization was to create a large null space in the model related mostly to horizontal and high-frequency variations in the vertical component of the slowness. This means that when 2-D anisotropic models are used anisotropy and heterogeneity cannot be estimated with the same resolution, no matter how simple the real medium is. Hence the importance of using the appropriate parametrization when information about the medium is available beforehand.

Since the singular value distribution is different for the different parametrizations, the effect of conventional regularization procedures such as damping, SVD truncation, or a simple early termination of CG iterations is also different when each of these parametrizations is used. When the model is isotropic, regularization translates into smoothness in the resolution of both data and model spaces. When the model is anisotropic, diminishing

the effect of the smallest singular values in the solution not only creates smoother images but may also introduce anisotropy where it doesn't actually exist or, more generally, may distort the anisotropy of the medium.

Figure A.2: SVD when the model is 1-D isotropic (six horizontal isotropic layers). **u** represents the singular vectors in data space and **v** represents the singular vectors in model space. The origin of the axes is at the upper left corner of each image. **r** is the receiver axis, **s** is the source axis, **x** is the horizontal distance, and **z** is the depth. The gray scale goes from black (negative) to white (positive).

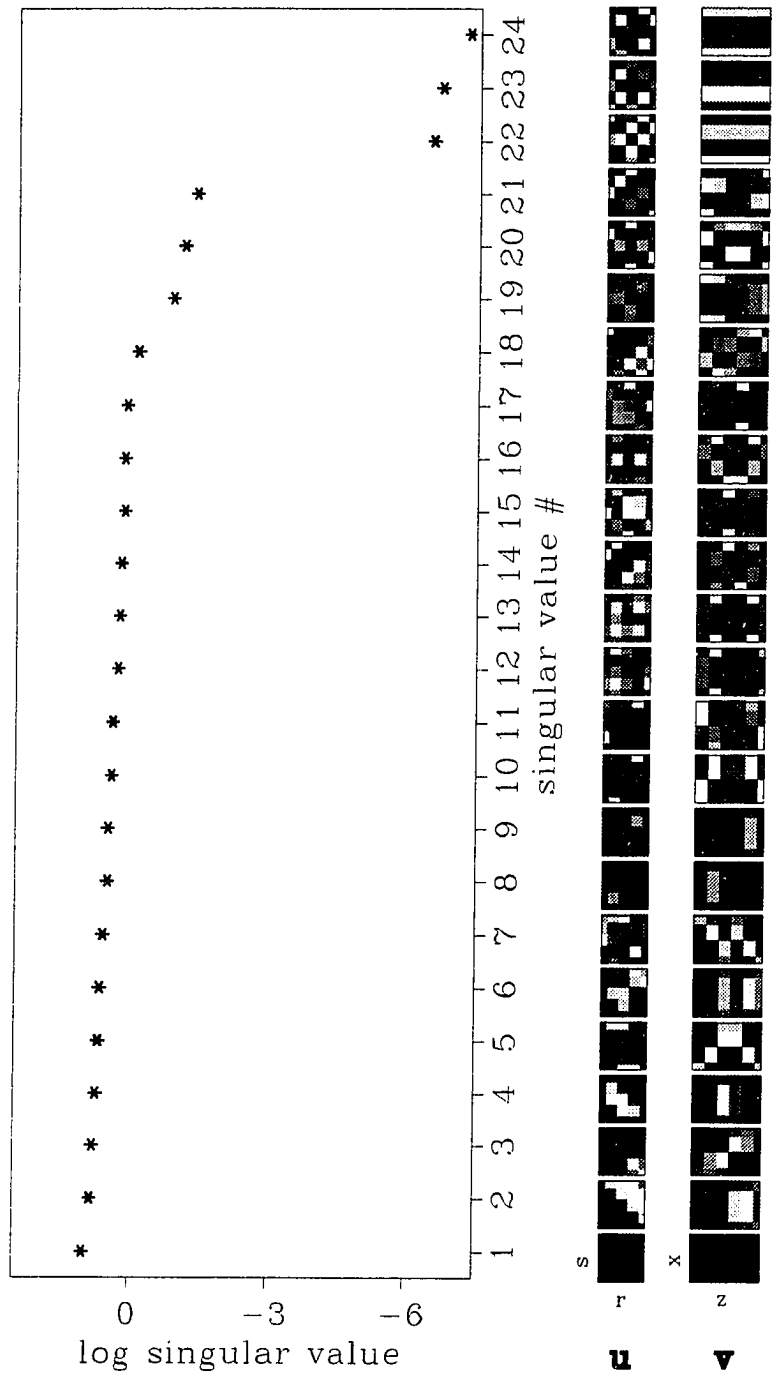

Figure A.3: SVD when the model is 2-D isotropic (6×4 homogeneous isotropic squared regions). The amount of lateral variation in the model space increases as the size of the singular values decreases.

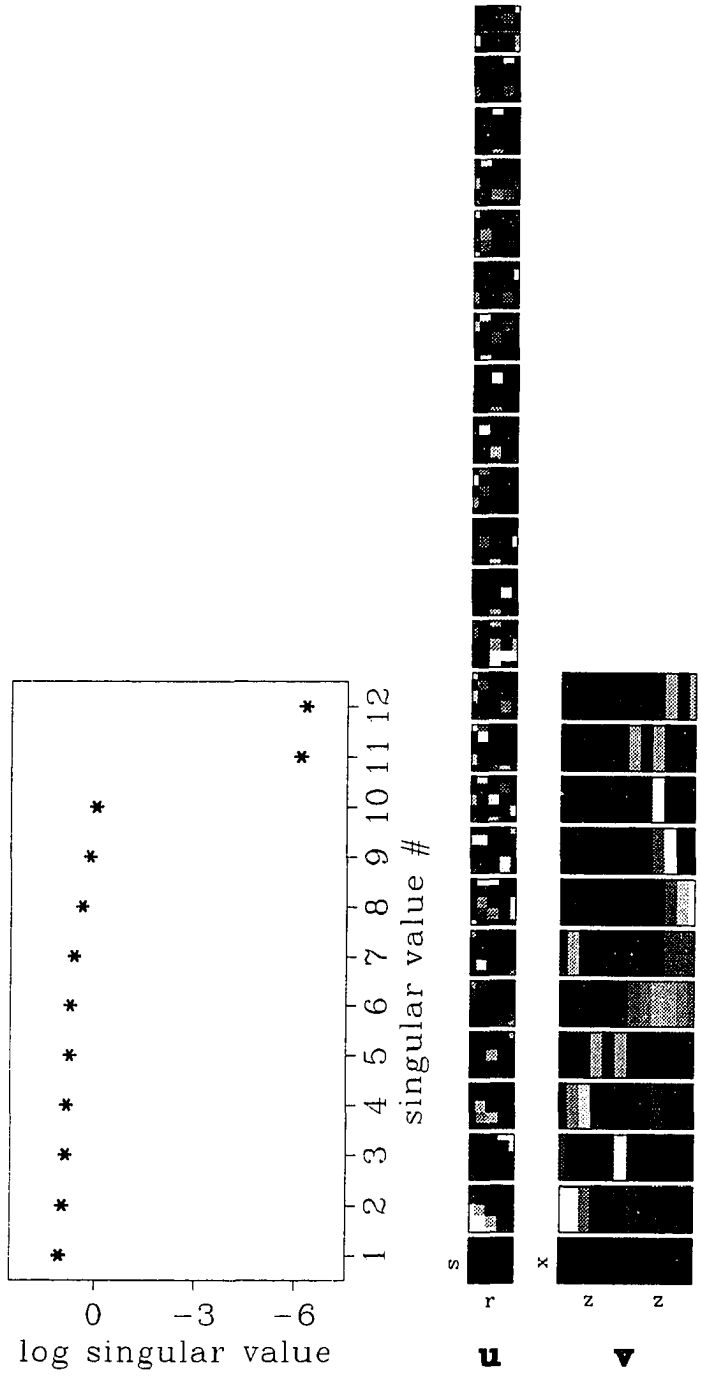

Figure A.4: SVD when the model is 1-D anisotropic (6 × 2 model parameters). The upper half of each image in the model space corresponds to $S_x(x,z)$, and the lower half corresponds to $S_z(x,z)$. The origin in the data space is at the upper left corner of each image.

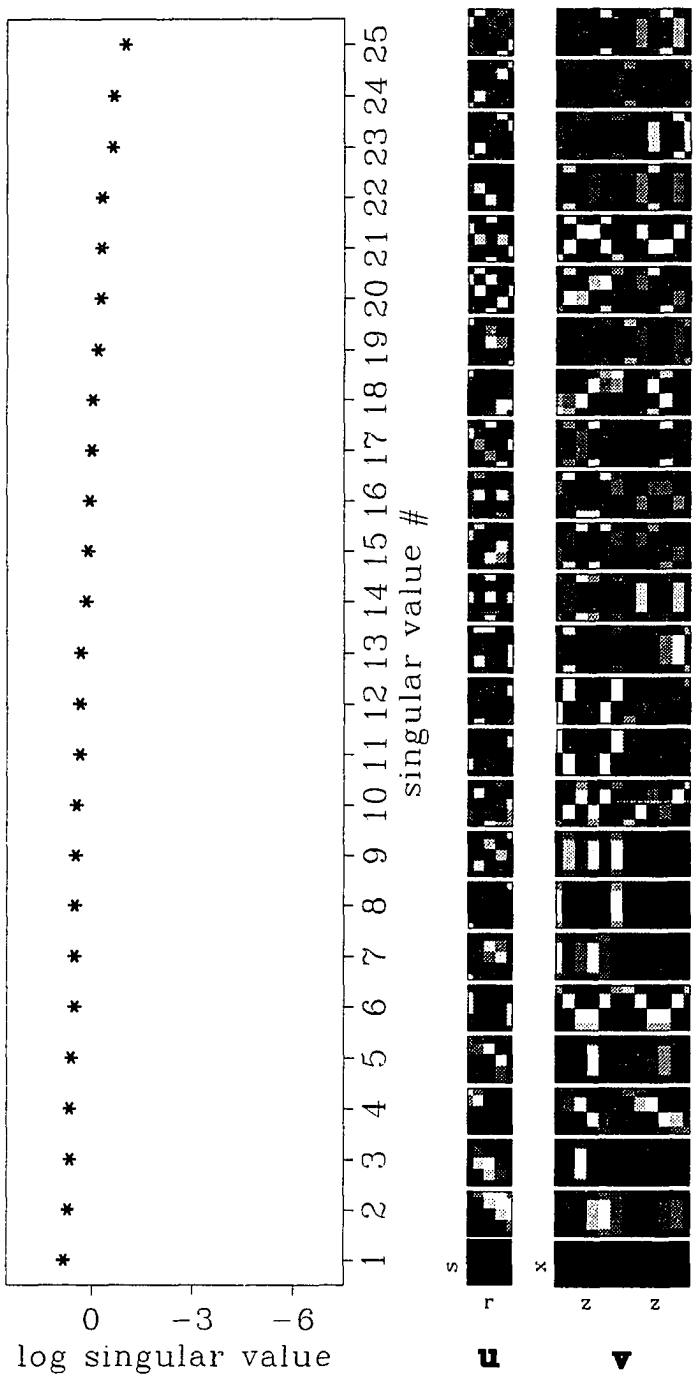

Figure A.5: SVD when the model is 2-D anisotropic. (24 × 2 model parameters).

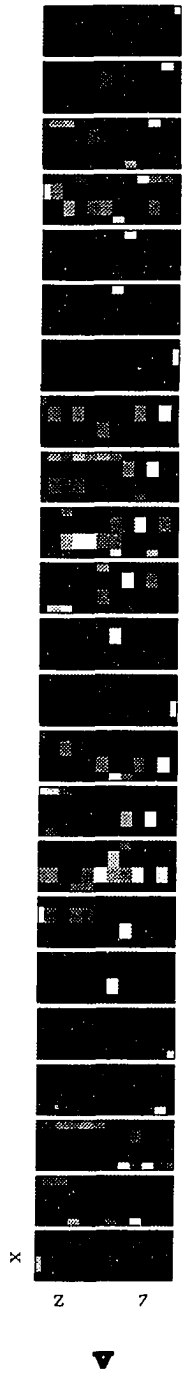

Figure A.6: Vectors that span the null space of the model for the SVD shown in Figure A.5. Most vectors contain information about $S_z(x,z)$ (nonzero components in the lower half of each image), and therefore, $S_z(x,z)$ cannot be estimated at the same resolution of $S_x(x,z)$ from cross-well traveltimes alone.

Appendix B

Coefficients of the equation that relates ray parameter and scattered phase angles

This appendix shows the explicit form of the coefficients a_i in equation (3.8), the fourth order polynomial that relates the angles of the scattered phases and the incident ray parameter. The coefficients are

$$\begin{aligned} a_0 &= c^4p^4 - T_0^2, \\ a_1 &= -2T_0T_1, \\ a_2 &= 2b^2c^2p^4 - 4d^2p^4 - T_1^2 - 2T_2T_0, \\ a_3 &= -2T_2T_1, \\ a_4 &= p^4b^4 - T_2^2, \end{aligned}$$

where

$$\begin{aligned} T_0 &= 2\sin^2(\gamma_2) - p^2(c^2 + 2a^2), \\ T_1 &= 2\sin(2\gamma_2), \\ T_2 &= 2\cos^2(\gamma_2) - p^2(b^2 + 2a^2), \\ a^2 &= c_{44}/\rho, \end{aligned}$$

$$
\begin{aligned}
b^2 &= (c_{11} - c_{44})/\rho, \\
c^2 &= (c_{33} - c_{44})/\rho, \\
d^2 &= [(c_{11} - c_{44})(c_{33} - c_{44}) - (c_{13} + c_{44})^2]/\rho^2.
\end{aligned}
$$

The constants c_{ij} are four of the five elastic constants that describe a homogeneous transversely isotropic medium, γ_2 is the orientation of the axis of symmetry measured from the normal to the interface, p is the ray parameter, and ρ is the density.

Appendix C

Traveltime in homogeneous elliptically anisotropic media with a nonvertical axis of symmetry

The expression for the ray velocity in a medium with elliptical velocity dependency is given by the expression

$$\frac{1}{V^2(\alpha)} = \frac{\cos^2\alpha}{V_{||}^2} + \frac{\sin^2\alpha}{V_{\perp}^2}, \tag{C.1}$$

where α is the ray angle measured from the axis of symmetry (positive counterclockwise), and $V_{||}$ and $V_{\perp}$ are the velocities in the directions parallel and perpendicular to the axis of symmetry (Figure C.1a). When the axis of symmetry is vertical, the angle that measures the direction of propagation of the ray with respect to the vertical is the same as the group velocity angle.

When the axis of symmetry is rotated an angle γ (Figure C.1b), the expression for the ray velocity (for the same ray direction) becomes

$$\frac{1}{V^2(\alpha)} = \frac{\cos^2(\alpha-\gamma)}{V_{||}^2} + \frac{\sin^2(\alpha-\gamma)}{V_{\perp}^2}, \tag{C.2}$$

where $\alpha - \gamma$ is the angle from the axis of symmetry to the ray (the group velocity angle).

If the ray travels a distance d between two points (Figure 4.1),

$$d = \sqrt{\Delta x^2 + \Delta z^2}, \tag{C.3}$$

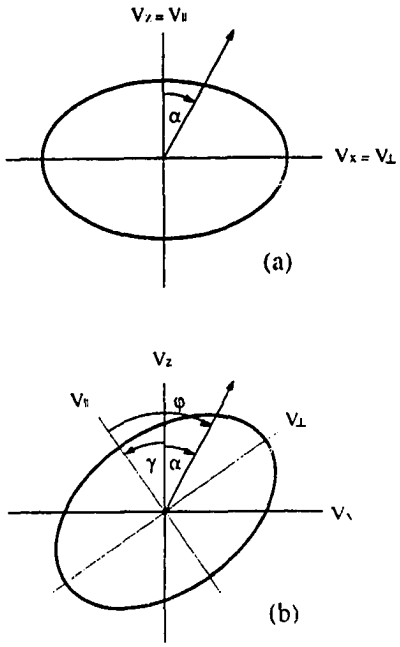

Figure C.1: Ray velocity as a function of direction in an elliptically anisotropic medium: (a) Vertical axis of symmetry (ray angle = group velocity angle). (b) Tilted axis of symmetry (ray angle = α; group velocity angle = ϕ).

the corresponding traveltime t is

$$t^2 = \frac{(d\cos(\alpha-\gamma))^2}{V_{||}^2} + \frac{(d\sin(\alpha-\gamma))^2}{V_{\perp}^2} \qquad (C.4)$$

$$= \frac{(d\cos\alpha\cos\gamma + d\sin\alpha\sin\gamma)^2}{V_{||}^2} + \frac{(d\sin\alpha\cos\gamma - d\cos\alpha\sin\gamma)^2}{V_{\perp}^2}.$$

To further simplify this equation we need to know the values of $d\cos\alpha$ and $d\sin\alpha$. In order to do this, we need to be careful about the sign of α (clockwise or counterclockwise) for the given ray direction. We also need to be careful about the signs of Δx and Δz. It turns out that regardless of how the signs of these quantities are defined (as long as they are consistent) the final expression for t^2 is always, as expected, the same. The result is

$$t^2 = \frac{(-\Delta z\cos\gamma + \Delta x\sin\gamma)^2}{V_{||}^2} + \frac{(\Delta x\cos\gamma + \Delta z\sin\gamma)^2}{V_{\perp}^2}. \qquad (C.5)$$

This is the expression for the traveltime of a ray that travels between two points separated by a distance d in a homogeneous elliptically anisotropic medium with the axis of symmetry forming an angle γ with the vertical. This equation is the heart of the inversion procedure that I propose in chapter 4.

Appendix D

Partial derivatives of the traveltime with respect to the model parameters

In this appendix, I show the expressions for the partial derivatives of the traveltime t_i [equation (4.5)] with respect to the model parameters m_k, where m_k is a component of the vector $\boldsymbol{m}$ as follows:

$$\begin{aligned}\boldsymbol{m} &= (m_1, ..., m_N, m_{N+1}, ..., m_{2N}, m_{2N+1}, ..., m_{3N}, m_{3N+1}, ..., m_{4N}, m_{4N+1}, ..., m_{5N}) \\ &= (S_{\perp_1}, ..., S_{\perp_N}, S_{\parallel_1}, ..., S_{\parallel_N}, \gamma_1, ..., \gamma_N, b_1, ..., b_N, a_1, ..., a_N).\end{aligned}$$

First, the derivatives with respect to the interval parameters $S_{\perp_j}$, $S_{\parallel_j}$, and γ_j $(1 \leq j \leq N)$ are

$$\frac{\partial t_i}{\partial m_k} = \begin{cases} \frac{\Delta X_{ik}^2 S_k}{t_{ik}} & \text{if } 1 \leq k \leq N \\ \frac{\Delta Z_{ik}^2 S_k}{t_{ik}} & \text{if } N+1 \leq k \leq 2N \\ \frac{\Delta X_{i,k} S_k^2 (-\Delta x_{i,k} \sin\gamma_k + \Delta z_{i,k} \cos\gamma_k)}{t_{i,k}} + & \\ \frac{\Delta Z_{i,k} S_{k+N}^2 (\Delta z_{i,k} \sin\gamma_k + \Delta x_{i,k} \cos\gamma_k)}{t_{i,k}} & \text{if } 2N+1 \leq k \leq 3N. \end{cases}$$

Note that, for the interval parameters, the derivatives with respect to the j^{th} variable depend only upon the properties of the j^{th} layer.

The derivatives of the traveltime with respect to the boundary parameters (a_j and b_j)

depend on the properties of the medium above and below that boundary, as follows:

$$\frac{\partial t_i}{\partial m_k} = \begin{cases} \frac{-\sin\gamma_k \Delta X_{i,k} S_k^2 + \cos\gamma_k \Delta Z_{i,k} S_{k+N}^2}{t_{i,k}} + \\ \frac{\sin\gamma_{k-1} \Delta X_{i,k-1} S_{k-1}^2 - \cos\gamma_{k-1} \Delta Z_{i,k-1} S_{k-1+N}^2}{t_{i,k-1}} & \text{if } 3N+2 \le k \le 4N \\ \frac{\partial t_i}{\partial m_{k-N}} x_{i,k} & \text{if } 4N+2 \le k \le 5N. \end{cases}$$

Since the traveltime t_i is not affected by the position of the top boundary, $\frac{\partial t_i}{\partial a_1} = \frac{\partial t_i}{\partial b_1} = 0$.

When a ray travels horizontally, only the first N components of the vector of partial derivatives are nonzero. For the forward modeling this is not problem; it simply means that the horizontal component of the velocity is the only parameter that affects the traveltime of a horizontally traveling ray. Problems arise, however, when we try to invert these traveltimes, because there are infinite combinations of the other parameters (null space) that satisfy the data equally well. This problem casues instability in the inversion procedure. For this reason, the inversion procedure described in chapter 4 does not use rays that travel exactly along the horizontal.

Making the appropriate simplifications in the above equations for the case of isotropic media results in a set of equations similar to the ones obtained by Lee (1990), except for two misprints in Lee's equations.

Bibliography

Aki, K., and Richards, P. G., 1980, Quantitative seismology, volume 1: W. H. Freeman Co.

Arts, R. J., Rasolofosaon, P. N. J., and Zinszner, B. E., 1991, Complete inversion of the anisotropic elastic tensor in rocks: experiment versus theory: 61st Ann. Internat. Mtg., Soc. Expl. Geophys., Expanded Abstracts, 1538–1541.

Auld, B. A., 1990, Acoustic fields and waves in solids, volumes 1 and 2: Robert E. Krieger Publishing Co.

Avasthi, J. M., Nolen-Hoeksema, R. J., and El Rabaa, A. W. M., 1991, In-situ stress evaluation of the McElroy field, west Texas: SPE Formation Eval., September issue, 301–309.

Babuska, V., and Cara, M., 1991, Seismic anisotropy in the earth: Kluwer Academic Publishers.

Backus, G. E., 1962, Long-wave elastic anisotropy produced by horizontal layering: J. Geophys. Res., **67**, 4427–4440.

Banik, N. C., 1984, Velocity anisotropy of shales and depth estimation in the North Sea basin: Geophysics, **49**, 1411–1419.

Berryman, J. G., 1979, Long wave elastic anisotropy in transversely isotropic media: Geophysics, **44**, 896–917.

Bregman, N. D., Bailey, R. C., and Chapman, C. H., 1989, Ghosts in tomography: the effects of poor angular coverage in 2-D seismic traveltime inversion: Can. J. Expl. Geophys., **25**, 7–27.

Byun, B. S., 1982, Seismic parameters for media with elliptical velocity dependencies: Geophysics, **47**, 1621–1626.

———, 1984, Seismic parameters for transversely isotropic media: Geophysics, **49**, 1908–1626.

Byun, B. S., and Corrigan, D., 1990, Seismic traveltime inversion for transverse isotropy: Geophysics, **55**, 192–200.

Carrion, P., Costa J., Ferrer Pinheiro, J. E., and Michael Schoenberg, 1992, Cross-borehole tomography in anisotropic media: Geophysics, **57**, 1194–1198.

Červený, V., 1972, Seismic rays and ray intensities in inhomogeneous anisotropic media: Geophys. J. R. Astr. Soc., **29**, 1–13.

Chapman, C. H., and Pratt, R. G., 1992, Traveltime tomography in anisotropic media–I. Theory: Geophys. J. Intl., **109**, 1–19.

Crampin, S., Chesnokov, E. M., and Hipkin, R. A., 1984, Seismic anisotropy–the state of the art: Geophys. J. R. Astr. Soc, **76**, 1–16.

Dellinger, J., 1989, Anisotropic traveltime inversion with error bars: theory: Stanford Expl. Proj. SEP-**60**, 253–260.

———, 1991, Anisotropic seismic wave propagation: Ph.D thesis, Stanford University.

Dellinger, J., and Muir, F., 1991, The double elliptic approximation in the group and phase domains: Stanford Expl. Proj. SEP–**70**, 361–366.

Dellinger, J., Muir, F., and Karrenbach, M., 1993, Anelliptic approximations for TI media: J. Seismic Expl., **2**, 23–40.

Dines, K. A., and Lytle, R. J., 1979, Computerized geophysical tomography: Proc. Inst. Electr. Electron. Eng., **67**, 1065–1073.

Dongarra, J. J., Bunch, J. R., Moler, C. B., and Stewart, G. W., 1979, Linpack: Users' Guide: Soc. Ind. Appl. Math., Chapter 11.

Gajewski, D., and Pšenčík, I., 1990, Vertical seismic profile synthetics by dynamic ray tracing in laterally varying layered anisotropic structures: J. Geophys. Res., **95**, 11 301–11 315.

Gill, P. H., Murray, W., and Wright, M. H., 1981, Practical Optimization: Academic Press.

Golub, G. H., and Van Loan, C. F., 1989, Matrix Computations. Johns Hopkins Univ. Press.

Hake, H., Helbig, K., and Mesdag, C. S., 1984, Three-terms Taylor series for $t^2 - x^2$ curves for P- and S-waves over layered transversely isotropic ground: Geophys. Prosp., **32**, 828–850.

Hanyga, A., 1982, Dynamic ray tracing in an anisotropic medium: Tectonophysics, **90**, 243–251.

Harlan, W. S., 1989, Tomographic estimation of seismic velocities from reflected raypaths: 59th Ann. Internat. Mtg., Soc. Expl. Geophys., Expanded Abstracts, 922–924.

Harris, J. M., 1988, Cross-well seismic measurements in sedimentary rocks: 58th Ann. Internat. Mtg., Soc. Expl. Geophys., Expanded Abstracts, 147–150.

Harris, J. M., Nolen-Hoeksema, R., Rector J. W., Van Schaack, M., and Lazaratos, S. K., 1992, High resolution cross-well imaging of a west Texas carbonate reservoir: Part 1. Data acquisition and project overview: 62nd Ann. Internat. Mtg., Soc. Expl. Geophys., Expanded Abstracts, 35–39.

Harris, J. M., Tan, H., Lines, L., Pearson, C., Treitel. S., Mavko, G., Moos, D., and Nolen-Hoeksema, R., 1990, Cross-well tomographic imaging of geological structures in Gulf Coast sediments: 60th Ann. Internat. Mtg., Soc. Expl. Geophys., Expanded Abstracts, 37–40.

Helbig, K., 1979, Discussion on "The reflection, refraction and diffraction of waves in media with elliptical velocity dependence" by F. K. Levin: Geophysics, **44**, 987–990.

Jech, J., and Pšenčík, I., 1989, First-order perturbation method for anisotropic media: Geophys. J. Internat., **99**, 369–376.

Karrenbach, M., 1992, "Plug and Play" wave equation modules: Stanford Expl. Proj. SEP–**75**, 273–287.

Lazaratos, S. K., Rector, J. W., Harris, J. M., and Van Schaack, M., 1991, High resolution imaging with cross-well reflection data: 61st Ann. Internat. Mtg., Soc. Expl. Geophys., Expanded Abstracts, 107–110.

Lazaratos, S. K., Harris, J. M., Rector, J. W., and Van Schaack, M., 1992, High resolution cross-well imaging of a west Texas carbonate reservoir: Part 4. Reflection imaging: 62nd Ann. Internat. Mtg., Soc. Expl. Geophys., Expanded Abstracts, 49–53.

Lee, M. W., 1990, Traveltime inversion using transmitted waves of offset vertical seismic profiling data: Geophysics, **55**, 1089–1097.

Levin, F. K., 1978, The reflection, refraction, and diffraction of waves in media with elliptical velocity dependence: Geophysics, **43**, 528–537.

———, 1979, Seismic velocities in transverse isotropic media: Geophysics, **44**, 25–36.

———, 1980, Seismic velocities in transverse isotropic media, II: Geophysics, **45**, 3–17.

Lines, L., 1992, Poor's man anisotropic traveltime tomography: 62nd Ann. Internat. Mtg., Soc. Expl. Geophys., Expanded Abstracts, 83–86.

McCann, C., Assefa, S., Sothcott, J., McCann, D. M., and Jackson, P. D., 1989, In-situ borehole measurements of compressional and shear wave attenuation in Oxford clay: Sci. Drilling, **1**, 11–20.

McMechan, G. A., 1983, Seismic tomography in boreholes: Geophys. J. Roy. Astr. Soc., **74**, 601–612.

Michelena, R. J., and Harris, J. M., 1991, Tomographic traveltime inversion using natural pixels: Geophysics, **56**, 635–644.

Miller, D. E., and Chapman, C. H., 1991, Incontrovertible evidence of anisotropy in cross-well data: 61st Ann. Internat. Mtg., Soc. Expl. Geophys., Expanded Abstracts, 825–828.

Muir, F., 1990a, A modified anisotropic system: Stanford Expl. Proj. SEP–**67**, 41–42.

———, 1990b, Various equations for TI media: Stanford Expl. Proj. SEP–**70**, 367–372.

Nolet, G., 1985, Solving or resolving inadequate and noisy tomographic systems: J. Comp. Phys., **61**, 463–482.

———, 1987, Seismic wave propagation and seismic tomography, *in* Nolet, G., Ed., Seismic tomography: D. Reidel Publ. Co., 1–23.

Onishi, M., and Harris, J. M., 1991, Anisotropy from head waves in cross-well data: 61st Ann. Internat. Mtg., Soc. Expl. Geophys., Expanded Abstracts, 115–118.

Pratt, R. G., Chapman, C. H., 1992, Traveltime tomography in anisotropic media–II. Application: Geophys. J. Intl., **109**, 20–37.

Qin, F., Luo, Y., and Cai, W., 1992, Traveltime inversion for anisotropic seismic data: 62nd Ann. Internat. Mtg., Soc. Expl. Geophys., Expanded Abstracts, 762–765.

Raikes, S., 1991, Shear-wave characterization of the BP Devine test site, Texas: 61st Ann. Internat. Mtg., Soc. Expl. Geophys., Expanded Abstracts, 65–68.

Saito, H., 1991, Anisotropic traveltime tomography at the Buckhorn test facility in Illinois: 62nd Ann. Internat. Mtg., Soc. Expl. Geophys., Expanded Abstracts, 123–126.

Scales, J. A., and Gersztenkorn, A., 1988, Robust methods in inverse theory: Inverse Problems, **4**, 1071–1091.

Schoenberg, M., and Muir, F., 1989, A calculus for finely layered anisotropic media: Geophysics, **54**, 581–589.

Sena, A., 1991, Seismic traveltime equations for azimuthally anisotropic and isotropic media: estimation of interval elastic properties: Geophysics, **56**, 2090–2101.

Squires, L. J., Blakeslee, S. N., and Stoffa, P. L., 1992, The effects of statics on tomographic velocity reconstructions: Geophysics, **57**, 353–362.

Stewart, R. R., 1988, An algebraic reconstruction technique for weakly anisotropic velocity: Geophysics, **53**, 1613–1615.

Stork, C., 1988, Comparison of Richardson's iteration with Chebyshev acceleration factors to conjugate gradient iteration, Stanford Expl. Proj. SEP–**57**, 479–503.

———, 1992, Singular value decomposition of the velocity-reflector depth tradeoff, Part 2: High-resolution analysis of a generic model: Geophysics, **57**, 933–943.

Thomsen, L., 1986, Weak elastic anisotropy: Geophysics, **51**, 1954–1966.

Van der Sluis, A., and Van der Vorst, H. A., 1987, Numerical solution of large, sparse linear algebraic systems arising from tomography problems, *in* Nolet, G., Ed., Seismic Tomography: D. Reidel Publ. Co., 49–84.

Van Schaack, M., Harris, J. M., Rector, J. W., and Lazaratos, S. K., 1992, High resolution cross-well imaging of a west Texas carbonate reservoir: Part 2. Wavefield analysis and tomography: 62nd Ann. Internat. Mtg., Soc. Expl. Geophys., Expanded Abstracts, 40–44.

Van Trier, J., 1988, Migration velocity analysis using geological constraints: 58th Ann. Internat. Mtg., Soc. Expl. Geophys., Expanded Abstracts, 897–900.

Vernik, L., and Nur, A., 1992, Ultrasonic velocity and anisotropy of hydrocarbon source rocks: Geophysics, **57**, 727–735.

White, D. J., 1989, Two-dimensional seismic refraction tomography: Geophys. J., **97**, 223–245.

White, J. E., Martineau-Nicoletis, L., and Monash, C., 1983, Measured anisotropy in Pierre shale: Geophys. Prosp., **31**, 707-725.

Williamson, P. R., Sams, M. S., and Worthington, M. H., 1993, Crosshole imaging in anisotropic media: The Leading Edge, **12**, 19–23.

Winterstein, D. F., 1986, Anisotropy effects in *P*-wave and *SH*-wave stacking velocities contain information on lithology: Geophysics, **51**, 661–672.

Winterstein, D. F., and Paulsson, B. N., 1990, Velocity anisotropy in shale determined from crosshole seismic and vertical seismic profile data: Geophysics, **55**, 470–479.